QUANTITATIVE PHASE IMAGING: INSTRUMENTATION, VALIDATION, AND ANNULAR ILLUMINATION

A Thesis
Presented to
The Academic Faculty

By

Pranav Prasad Kulkarni

In Partial Fulfillment
of the Requirements for the Degree
Master of Science in Electrical and Computer Engineering

Georgia Institute of Technology

December 2021

QUANTITATIVE PHASE IMAGING: INSTRUMENTATION, VALIDATION, AND ANNULAR ILLUMINATION

Thesis committee:

Dr. Thomas K. Gaylord, Advisor
School of Electrical and Computer Engineering
Georgia Institute of Technology

Dr. Wenshan Cai
School of Electrical and Computer Engineering
Georgia Institute of Technology

Dr. Stephen E Ralph
School of Electrical and Computer Engineering
Georgia Institute of Technology

Dr. Yijun Bao
Department of Biomedical Engineering
Duke University

Dr. Sorin Tibuleac
ADVA Optical Networking

Date approved: November 23, 2021

ACKNOWLEDGMENTS

I would like to thank my thesis advisor, Dr. Thomas K. Gaylord, for being a constant source of inspiration, support, and guidance throughout my time at Georgia Tech. He is an exemplary advisor, mentor, teacher, and friend. His academic excellence, optimism, humility, and kindness inspire me to be a better researcher and a better person. I am grateful for the opportunity to work with him and am fortunate to have him as a mentor and a friend.

I am also grateful to the other members of my committee, Dr. Stephen Ralph, Dr. Wenshan Cai, Dr. Sorin Tibuleac, and Dr. Yijun Bao, for their valuable insight and feedback on this work. Their questions, suggestions, and feedback are of great help, and I am honored to have them on my thesis committee.

I owe special thanks to Dr. Yijun Bao for his generous help in overcoming the difficulties in completing this work. He always made himself available to answer my questions and provided me with his valuable suggestions. I would also like to thank my previous and current fellow students at the Optics Laboratory, Ji Ye Chun, Shengtao Yu, Gabriel Krivian, William Schaffer, George Hopkins, and Lukas Yoder, for helping me with experiments and projects.

This work would not have been possible without the support of my loving friends, Jagriti Sahoo, Anubhav Sachan, Dhrumil Shah, and Roshan Shetty. I am grateful to them for supporting me through all the ups and downs in my life at Georgia Tech, and I consider myself truly blessed to have them as my friends.

I thank my parents, Prasad and Prdanya Kulkarni, for having an unwavering faith in me and for giving me an opportunity to realize my dreams. I am grateful beyond words for their hard work and sacrifices over the years so that I and my sister could get the best of everything. I thank my sister, Vaishnavi, for being a constant source of happiness in my life, and my grandmother, Vijaya, for her care and affection. I am grateful to my family for their constant love and support throughout my life.

TABLE OF CONTENTS

LIST OF TABLES

LIST OF FIGURES

LIST OF ABBREVIATIONS

CGH Computer Generated Hologram

CTF Contrast Transfer Function

DHM Digital Holographic Microscopy

DIC Differential Interference Contrast

DPC Differential Phase Contrast

EBL Electron Beam Lithography

EPS Effective Pixel Size

ETL Electrically Tunable Lens

EUV Extreme Ultraviolet

FBG Fiber Bragg Grating(s)

FIR Finite Impulse Response

HMC Hoffman Modulation Contrast

HPM Hilbert Phase Microscopy

ITIA Interferometry with Triple Imaging Area

IWFR Iterative Wave Function Reconstruction

LPFG Long-Period Fiber Grating(s)

LS-MFPI-PC Least Squares MFPI-PC

MFPI Multifilter Phase Imaging

MFPI-C Multifilter Phase Imaging with Coherent Light

MFPI-PC Multifilter Phase Imaging with Partially Coherent Light

ML Machine Learning

NA Numerical Aperture

OAH Off-Axis Holography

OAI Off-Axis Interferometry

ODT Optical Diffraction Tomography

OFC Optical Fiber Characterization

OFS Optimal Frequency Selection

OPL Optical Path Length

OTF Optical Transfer Function

PCM Phase Contrast Microscopy

PCTF Phase Contrast Transfer Function

PM Ptychographic Microscopy

POS Piezoelectric Objective Scanner

POTF Phase Optical Transfer Function

POTFR Phase Optical Transfer Function Recovery

PR Phase Retrieval

PSH Phase Shifting Holography

PSI Phase Shifting Interferometry

PTF Phase Transfer Function

PZT Piezoelectric Transducer

QPI Quantitative Phase Imaging

QWLSI Quadriwave Lateral Shearing Interferometry

RBC Red Blood Cells

RI Refractive Index

SGDF Savitzky-Golay Differentiation Filters

SLIM Spatial Light Interference Microscopy

SLM Spatial Light Modulators

SNR Signal-to-Noise Ratio

TDPM Tomographic Deconvolution Phase Microscopy

TIE Transport of Intensity Equation

WD-PCTF Weakly-Defocused Phase Contrast Transfer Function

WLS Weighted Least Squares

WLS-MFPI-PC Weighted Least Squares MFPI-PC

WOTF Weak Object Transfer Function

LIST OF SYMBOLS

F_{Disk} 2D FFT of disk illumination phase image ($\mathrm{rad} \cdot \mu\mathrm{m}^2$)

F_{Annular} 2D FFT of annular illumination phase image ($\mathrm{rad} \cdot \mu\mathrm{m}^2$)

F_{ideal} 2D FFT of ideal image ($\mathrm{rad} \cdot \mu\mathrm{m}^2$)

$\tilde{I}$ 3D Image intensity spectrum ($\mu\mathrm{m}$)

$T_{\mathrm{P}}^{(3)}(\boldsymbol{\rho}, \eta)$ 3D phase optical transfer function (dimensionless)

$T_{\mathrm{A}}^{(3)}(\boldsymbol{\rho}, \eta)$ 3D absorption optical transfer function (dimensionless)

$\tilde{T}_{\mathrm{P}}^{(3)}(\boldsymbol{\rho}; \eta, \rho_{\mathrm{si}}, \rho_{\mathrm{s}})$ 3D phase optical transfer function for annular source normalized by background intensity ($\mu\mathrm{m}^2$)

$\tilde{T}_{\mathrm{P}}^{(3)}(\boldsymbol{\rho}; \eta, 0, \rho_{\mathrm{s}})$ 3D phase optical transfer function for disk source normalized by background intensity ($\mu\mathrm{m}^2$)

B Background intensity ($\mu\mathrm{m}^{-2}$)

ρ_{p} Boundary of nonzero pupil function ($\mu\mathrm{m}^{-1}$)

$a_i^{(k)}$ Coefficient of the (2*k*-1)th order of SGDF (dimensionless)

S Coherence parameter (dimensionless)

$(.)^*$ Complex conjugate

$\tilde{\phi}(\boldsymbol{\rho})_{\mathrm{composite}}$ Composite phase after combining all SGDF orders (rad.)

ξ Cut-off ratio (dimensionless)

ρ_c Cut-off spatial frequency ($\mu\mathrm{m}^{-1}$)

Δz Defocus distance ($\mu\mathrm{m}$)

$\boldsymbol{\delta}(.)$ Delta function

δ_{Disk} Deviation of 2D FFT of disk case from ideal FFT ($\mathrm{rad} \cdot \mu\mathrm{m}^2$)

$\delta_{\mathrm{Annular}}$ Deviation of 2D FFT of annular case from ideal FFT ($\mathrm{rad} \cdot \mu\mathrm{m}^2$)

Δx EPS of the camera for a given objective lens ($\mu\mathrm{m}$)

ω Free parameter used in the MATLAB program (dimensionless)

h Height of the ridges (bars) on the phase masks.

NA_{ci} Inner numerical aperture of condenser lens (dimensionless)

ρ_{si} Inner boundary of nonzero source function ($\mu\mathrm{m}^{-1}$)

$\boldsymbol{I}(\boldsymbol{r}, z)$ Intensity at plane z ($\mu\mathrm{m}^{-2}$)

∇^2 Laplacian operator

$\boldsymbol{r}$ Lateral 2D spatial coordinate ($\mu\mathrm{m}$)

$\boldsymbol{\rho}$ Lateral 2D spatial frequency ($\mu\mathrm{m}^{-1}$)

$\nabla_{x,y}$ Lateral gradient operator

$\frac{\partial \boldsymbol{I}(\boldsymbol{r},z)}{\partial z}$ Longitudinal intensity derivative ($\mu\mathrm{m}^{-3}$)

$\frac{\partial \boldsymbol{I}(\boldsymbol{r},0)}{\partial z}$ Longitudinal intensity derivative at focal plane ($\mu\mathrm{m}^{-3}$)

z Longitudinal spatial coordinate ($\mu\mathrm{m}$)

η Longitudinal spatial frequency ($\mu\mathrm{m}^{-1}$)

M_{obj} Magnification of the objective lens (dimensionless)

ρ Magnitude of 2D lateral spatial frequency $\boldsymbol{\rho}$ ($\mu\mathrm{m}^{-1}$)

$\bar{\lambda}$ Mean wavelength of quasi-monochromatic source ($\mu\mathrm{m}$)

$\Delta\delta$ Normalized difference of deviation between disk and annular cases (dimensionless)

$f_{x,(K,n)}$ Number of lines per millimeter (spatial frequency) for Group *K* element *n* in USAF resolution test chart (lines/mm)

NA_{o} Numerical aperture of objective lens (dimensionless)

$\tilde{\phi}(\boldsymbol{\rho})$ Object phase spectrum ($\mu\mathrm{m}^2$)

NA_{c} Outer numerical aperture of condenser lens(dimensionless)

ρ_s Outer boundary of nonzero source function ($\mu\mathrm{m}^{-1}$)

$T_{\mathrm{P}}^{(2)}(\boldsymbol{\rho})$ Phase contrast transfer function ($\mu\mathrm{m}^{-3}$)

$T_{\mathrm{P_{TIE}}}^{(2)}(\boldsymbol{\rho})$ Phase contrast transfer function in TIE approximation ($\mu\mathrm{m}^{-3}$)

$\tilde{\phi}(\boldsymbol{\rho})_n$ Phase estimated using *n*th order of SGDF (rad.)

$T_{\mathrm{P},k}{}^{(2)}(\rho))$ Phase contrast transfer function of (2*k*-1)th order of SGDF ($\mu\mathrm{m}^{-3}$)

$\phi(\boldsymbol{r})$ Phase of the object (rad.)

$\tilde{p}(\boldsymbol{\rho})$ Pupil function (dimensionless)

α Regularization parameter (unit depends on application)

R_{Disk} Resolution for disk case ($\mu\mathrm{m}$)

R_{Annular} Resolution for annular case ($\mu\mathrm{m}$)

n_{oil} RI of the index matching oil (dimensionless)

n_1 RI of air (dimensionless)

n_2 RI of silica substrate (dimensionless)

Z Scanning range of the POS (μm)

$\tilde{S}(\boldsymbol{\rho})$ Source function (dimensionless)

$\tilde{A}(\boldsymbol{\rho}, \eta)$ Spatial spectrum of object absorption (μm^2)

N Total number of intensity patterns (dimensionless)

$H_{\mathrm{SG}}(e^{j2\pi\eta})$ Transfer function of SGDF (μm^{-1})

$H_{\mathrm{SG,k}}(e^{j2\pi\eta})$ Transfer function of (2*k*-1)th order of SGDF (μm^{-1})

λ Wavelength (μm)

$T^{(2)}_{\mathrm{PW}}(\boldsymbol{\rho})$ Weakly-defocus phase contrast transfer function (μm^{-3})

$T^{(2)}_{\mathrm{PW}}(\boldsymbol{\rho}; \rho_{\mathrm{si}}, \rho_{\mathrm{s}})$ Weakly-defocused phase contrast transfer function for annular source (μm^{-3})

$T^{(2)}_{\mathrm{PW}}(\boldsymbol{\rho}; 0, \rho_{\mathrm{s}})$ Weakly-defocused phase contrast transfer function for disk source (μm^{-3})

$H^{(k)}(\rho)$ Weighting filter of the phase from (2*k*-1)th order of SGDF (dimensionless)

$H^{(k)}_{\mathrm{LS}}(\rho)$ Weighting filter of the phase from (2*k*-1)th order of SGDF in LS-MFPI-PC (dimensionless)

$H^{(k)}_{\mathrm{WLS}}(\rho)$ Weighting filter of the phase from (2*k*-1)th order of SGDF in WLS-MFPI-PC (dimensionless)

SUMMARY

The imaging of transparent objects like biological cells and optical fibers is difficult using conventional optical microscopy. Quantitative Phase Imaging (QPI) provides a label-free, quantitative, and reliable way of imaging transparent objects. Conventionally, disk illumination has been widely used as a standard illumination type in microscopy. However, annular illumination provides a way to enhance contrast and improve resolution. In this work, the phase recovery performance of the two illumination types was compared using 2D QPI experiments performed on a standard-type phase test chart using weighted-least squares multifilter phase imaging with partially coherent light (WLS-MFPI-PC). A state-of-the-art QPI system with 2D QPI and 3D QPI capabilities was developed for performing the experiments and is described in detail. The reconstructed phase images were compared to an ideal image using spatial frequency response. Furthermore, the comparison results were found to match the theoretical predictions from MFPI-PC showing the significant advantage of annular illumination in higher spatial frequencies. Thus, the model used to describe the optics of QPI for the two illumination types was validated. A summary of the paraxial, non-paraxial, and WLS-MFPI-PC theories is also provided for the readers.

CHAPTER 1
INTRODUCTION

This chapter provides an overview of the background, motivation and impact of research in Quantitative Phase Imaging (QPI). The background covers conventional qualitative imaging methods and their limitations. In the motivation and impact section, the necessity for QPI is established and is discussed in the context of its application in various fields. The literature review provides a detailed overview of various QPI techniques and their applications. Furthermore, a literature review of annular illumination research is also discussed. Following the background, motivation, and impact, the techniques developed by Optics Laboratory at Georgia Tech are discussed and the research objectives for this thesis are defined. Finally, an overview of the organization of the thesis is provided at the end of this chapter.

1.1 Background

The field of optical imaging has seen tremendous development since the invention of the first microscope at the time of Robert Hooke's *Micrographia*. Now, it is possible to view the farthest of objects in space, the smallest of bacteria in soil, and as will be described further, even objects that are transparent. All of this has become possible due to development of powerful telescopes and microscopes, and more importantly, because of insightful techniques used to overcome various technological challenges.

"Contrast" in optical microscopy, can be categorized as either exogenous (extrinsic) or endogenous (intrinsic). Exogenous contrast is achieved by techniques like fluorescence microscopy [1] that makes use of exogenous contrast agents or "labelling markers" like specific fluorescent molecules to highlight the internal structure of biological samples [2–5]. This method has led to many advancements in biological studies, and is highly effective in

providing high contrast images of biological samples. In fact, fluorescence microscopy has also been used to attain "super-resolution" by circumventing the limitation of the diffraction limit [6–8]. Even though this technique has been widely used and has improved over time, the use of external fluorescent agents renders the biological samples prone to phototoxicity and photobleaching, depending on the type of agent used and its compatibility with the sample [9, 10]. This makes it unusable on samples that are incompatible with fluorescent markers and does not allow for its use in continuous imaging of cells over long periods of time, which is an important part of observing various cellular processes. There have been efforts to reduce the effects of phototoxicity on cells by improving illumination techniques, reducing the exposure time, developing better imaging techniques etc. [11]

On the other hand, endogenous contrast arises from the internal structure of cells and other objects being imaged. If the object being imaged has a good endogenous contrast, then no external agents are needed and it can be imaged in its natural state. However, biological cells and optical fibers are transparent phase objects and hence, do not absorb or scatter enough light to produce good contrast under usual illumination conditions. It is difficult to obtain good images of cells by measuring the intensity variation of light. Nevertheless, good contrast can be achieved by using the phase variation of the light illuminating the cells and the fibers. This has been done with methods like Phase Contrast Microscopy (PCM), Differential Interference Contrast (DIC), Hoffman Modulation Contrast (HMC), dark field microscopy, polarized light microscopy, etc. In PCM, an annular phase plate is used to amplify the phase difference between the background light and the light through the sample to produce high contrast [12, 13] whereas in DIC, the linearly polarized light is split into two orthogonally polarized beams using a Wollaston or a Nomarski prism, passed through the sample, and finally recombined by passing through an analyzer to obtain a phase interference image of the sample [14–16]. Figure 1.1 shows the images of biological samples obtained through the various techniques mentioned above and shows an image of cells in bright-field illumination obtained by staining the sample to enhance the contrast.

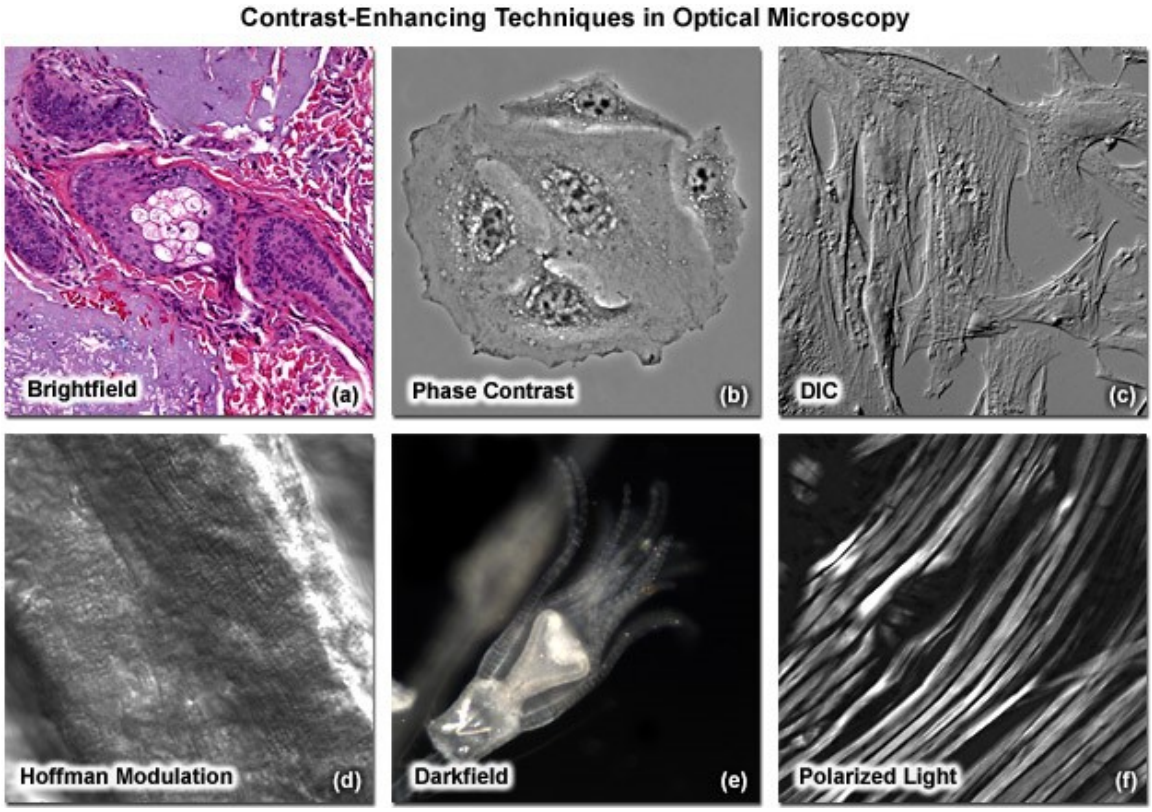

Figure 1.1: (a) Human basal cell carcinoma with hematoxylin-eosin stain to enhance contrast in bright-field illumination; (b) living HeLa cells imaged using PCM; (c) Indian Muntjac cells in aqueous medium imaged using DIC; (d) Mouse heart muscle bathed in aqueous saline solution imaged using HMC; (e) Obelia Hydroid specimen imaged using dark-field illumination; (f) Rabbit skeletal muscles clearly visible in polarized light microscopy due to birefringence. (images from [17])

Although the above-mentioned methods do not need any external "labelling markers" and can be used for continuous imaging for prolonged time periods, they only provide a "qualitative" image that cannot be used to quantify any physical properties of the sample. This is because the intensity measured at the image plane has a nonlinear relationship with the phase of the light and hence it cannot be used to obtain quantitative information about the phase of the light transmitted through the sample. This drawback, along with advancements in holography and computing, has led to a growth of QPI techniques that have the advantage of being "label-free" or non-invasive and have the ability to provide quantitative data about the phase, that can be further used to obtain morphological details of the sample. In recent years, QPI techniques have been developed to resolve the phase information in

2D objects as well as 3D objects, hence providing a detailed map of the internal structure of the sample being imaged. QPI combines the areas of optics, imaging theory, and computational methods to provide an accurate description of the refractive index variation or morphological structure of the sample.

1.2 Motivation and Impact

QPI has been applied in a variety of biological studies. Many of the achievements are listed in [18]. As described there, one of the major areas of study is the measurement of the dry mass and dry mass density of the cells [19–22]. This is important because it is used to measure cell growth, follow cell cycles, measure the effects of drugs, as well as measure cell metabolism. QPI has been used in the analysis of blood coagulation processes by observing an aggregation structure of Red Blood Cells (RBC) with Digital Holographic Microscopy (DHM) [23] and for measurement of fluctuations in the structure of cell membrane of RBCs for different storage periods [23]. In the case of RBCs, it is possible to determine the haemoglobin count in the cells using the measurement of it's refractive index [24].

Furthermore, using QPI, it is possible to detect certain types of cancers and tumors as the cancerous growth can be detected via monitoring the changes in the Refractive Index (RI) of the cells [25, 26]. Similarly, QPI has been used to identify and classify leukemia cells with the help of Machine Learning (ML) algorithms that can "discern healthy cells from lymphoblasts and classify stages of B cell acute lymphoblastic leukemia," by determining the morphological information like dry mass and volume of healthy cells and comparing those to that of cancerous cells [27]. QPI is also useful in enhanced assesment of optomechanical properties of cancer cells [28]. Furthermore, similar studies have been performed for early detection of esophageal cancer [29], breast cancer [30, 31], drug resistance in cases of endometrial cancer [32], and other cancer studies [33–35]. The ability of QPI to provide information about details like dry mass, intracellular mass transport [36],

cell volume [37], etc. is useful in the study of various diseases like sickle-cell disease [38], malaria [39], diabetes [40], etc. It is also useful in demonstrating that cell nuclei have a lower refractive index and mass density than the cytoplasm of the cell [41].

Beyond the field of clinical diagnostics and biological studies, QPI is also applicable to semiconductor research as it allows visualization of defects and features that are difficult to capture in conventional intensity variation measurements. It has been used for imaging particles embedded in three-dimensional microscopic structures [42], for determining the number of layers in and imaging of 2D materials [43], for silicon wafer defect inspection in manufacturing applications [44, 45], and for the imaging of nanoscale electrostatic and magnetic fields in nanostructured materials [46]. QPI has also been applied to in X-ray radiology, adaptive optics, and manufacturing using electron microscopy.

An important area of application of QPI is Optical Fiber Characterization (OFC). The world is witnessing a rapid development in fiber-based technologies and optical fiber communication. As these developments take place, it is necessary to understand the fundamental mechanisms that enable their operation. Earlier, such mechanisms were understood based on the measurement of transmission properties and characteristics. However, it does not provide an insight into the fundamental processes underlying the operation and it renders the understanding of such processes as mere assumptions albeit with empirical observations. As described in the introduction of Micah Jenkin's thesis [47], identification of the mechanisms producing RI modulation in Long-Period Fiber Grating(s) (LPFG) is an example of the limitations of conventional measurement approaches. These mechanisms have been previously explained by residual stress modification, changes of frozen-in viscoelasticity, dopant diffusion, structural deformation, etc. As these mechanisms lead to changes in RI, QPI can be used to measure these changes and enable a direct determination of the role of such mechanisms in the operation of various fiber-based devices. The QPI techniques developed by Jenkins [47–50] are able to produce high quality phase images of the cross section of various types of optical fibers, as well as high contrast phase im-

ages of cells [49, 50], as shown in Fig. 1.2. One of the 3D QPI techniques developed at Optics Laboratory at Georgia Tech, called Tomographic Deconvolution Phase Microscopy (TDPM) has also been used to obtain images of cross-sectional refractive index variations in Fiber Bragg Grating(s) (FBG), which had not been previously observed [51].

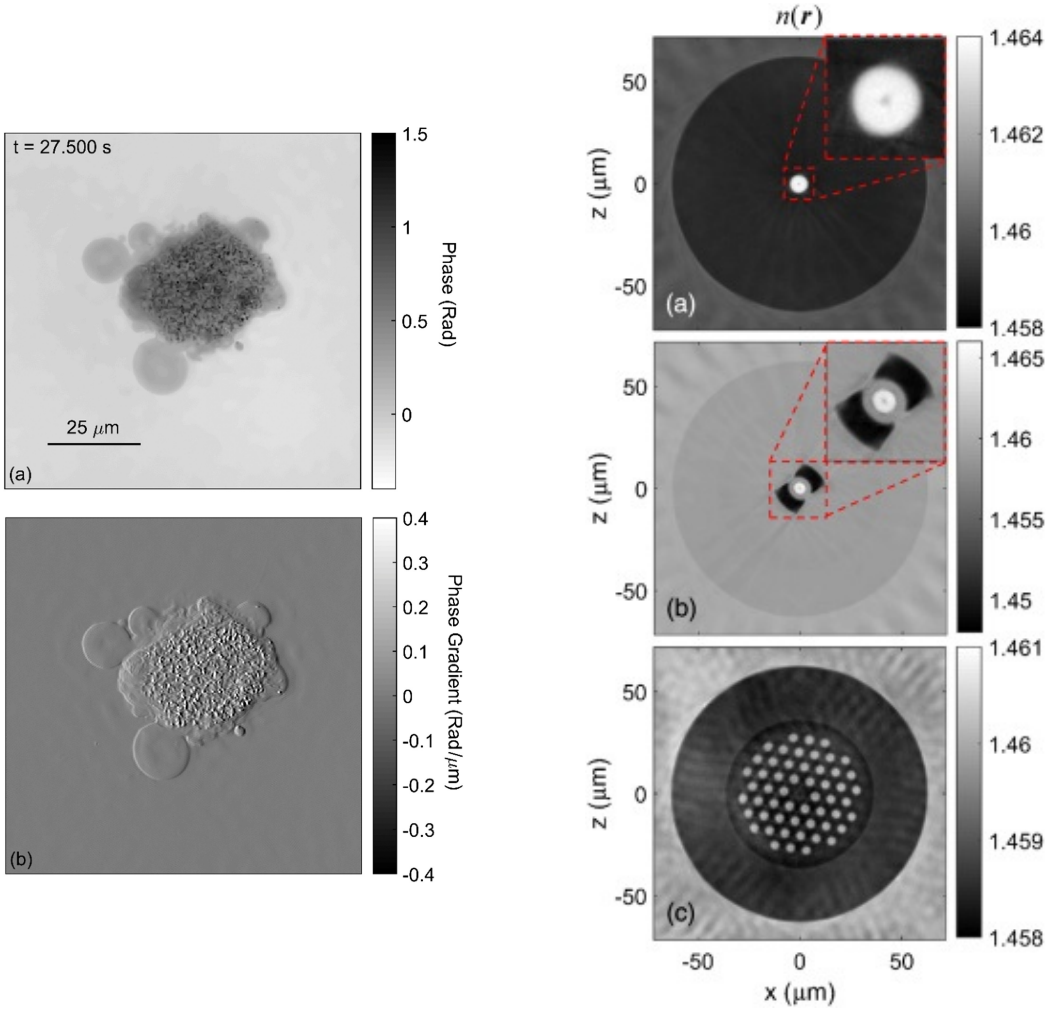

Figure 1.2: Left: Snapshot of live bovine mesenchymal stem cell cluster via (a) QPI and (b) simulated DIC (image extracted from [49]). Right: 2D tomograms obtained on (a) single-mode, (b) polarization-maintaining, and (c) photonic crystal fiber (image from [50]).

In addition, several companies have developed commercial QPI techniques and technologies for both 2D and 3D imaging. Examples of such companies include Phi Optics Inc. (2D imaging) [52] and Tomocube Inc. (3D imaging) [53]. Phi Optics Inc. was founded in 2009 and according to their website, they "combine the performance of traditional modal-

itites of a light microscope (eg. fluorescence, DIC, phase contrast) with real-time 3D topography capabilities of QPI. This combination offers a significant advantage for applications that require low-cost, fast, and accurate imaging of nanostructures" [52]. Whereas, Tomocube Inc. was founded in 2016 and has developed Optical Diffraction Tomography (ODT) technology that produces 3D refractive index maps of weakly absorbing phase samples. According to Tomocube Inc's website, "ODT is the technology that makes a 3D image (tomogram) with the RI and the 3-dimensional location which can be obtained by calculating phase shift in hologram taken around the specimen 360°."[53] There are other companies such as Lyncee tec [54], Nanolive [55], Phase Holographic Imaging [56], and Ovizio Imaging Systems [57] that use a variety of techniques to perform QPI and obtain phase images.

Considering all the above applications and advancements, it is evident that QPI is a rapidly developing area of research with a strong impact on a variety of fields. The research being undertaken and the number of papers being published in this area also suggests that it has the potential for many more applications in future. As new techniques of QPI are developed, the ability to extract important information about the objects being imaged is also improving with time. Research is needed to understand the limitations of existing QPI methods and to overcome those limitations by introducing new techniques or by improving the existing techniques.

The Optics Laboratory at Georgia Tech has developed several QPI techniques with the capability to produce high quality phase images of both 2D and 3D objects. These techniques, when published, were experimentally verified on objects like microlens arrays and visible transmission gratings. However, there was no standard test object for phase measurements. Therefore, it was necessary to validate the performance of these methods experimentally by using a standard test object like a phase mask with its phase and spatial variations known with high accuracy. Such an object can be used for comparing the performance of multiple methods and illumination types. Such an experimental validation of QPI

methods using calibrated phase objects and comparison of disk and annular illumination is the motivation behind the research described in this thesis.

In the following section, an overview of existing QPI methods is provided with a comparison of their advantages and limitations. A review of existing instrumentation for QPI is also provided.

1.3 Literature Review

1.3.1 2D QPI Techniques

2D QPI methods image the optical path length of a phase object by integrating the phase along the optical axis. There are a variety of QPI methods in the literature [58]. The methods can be broadly classified into three catagories [59]: interference-based, scanning-based, and defocus-based. As the name suggests, interference-based methods use interference between two light waves to produce an interferogram at the image plane. Whereas, scanning-based and defocus-based methods use phase retrieval algorithms for reconstructing the final phase image.

The most popular form of QPI is interference-based QPI. These methods are also called holographic methods as they create a hologram in the image plane. They can be further classified into two categories: Phase Shifting Interferometry (PSI) or Phase Shifting Holography (PSH) [60, 61], and Off-Axis Interferometry (OAI) or Off-Axis Holography (OAH) [62–64]. In PSI, a coherent beam is split into two beams using a beam splitter and then are recombined collinearly at the image plane. The two arms are called the sample and reference arms. The former passes through the phase sample, while the latter undergoes a known phase shift. The two arms interfere and produce an interferogram at the image plane. For quantitative phase recovery, four such interferograms are recorded for different phase shifts of the reference arm. Generally, the phase is modulated in 4 equal increments around the unit circle (0, $\pi/2$, π, $3\pi/2$) and the corresponding interferograms are recorded. Phase is then recovered using appropriate trigonometric relationships. The reference arm

undergoes a temporal phase change that can be achieved, for example, by a liquid crystal phase modulator [65], a piezoelectric transducer [61], or an acousto-optic modulator [66]. The spatial resolution obtained in PSI depends on the inherent spatial resolution in the imaging optics of the arms, which can be diffraction-limited. Furthermore, the phase recovery is based on simple relationships, and is one of the advantages of this method. The main limitations of this method arise from the fact that four interferograms are required to reconstruct one phase image. This results in a slow image acquisition speed. In addition, the use of monochromatic coherent light can lead to phase and speckle noise, which deteriorates the image quality. In Fig. 1.3, a block diagram representation of PSI is illustrated.

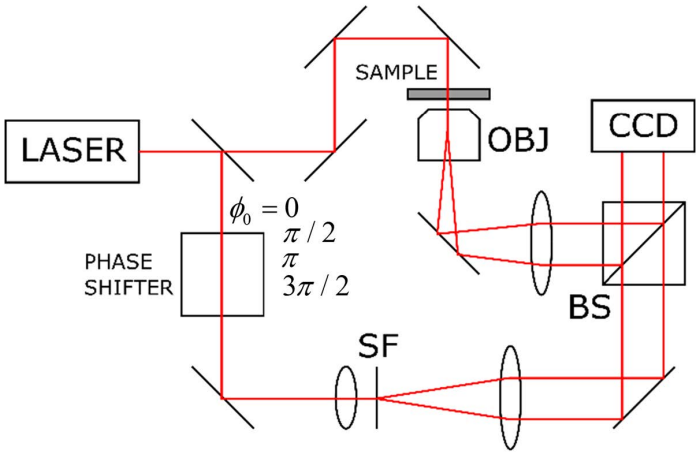

Figure 1.3: Block diagram of PSI using a Mach-Zehnder configuration showing sample arm, reference arm, and known phase increments in reference arm. OBJ = Object, BS = Beam Splitter, SF = Spatial Filter and CCD = Charged-Coupled Device camera. (image from [47])

OAI has a similar configuration as PSI, with the incident beam split into reference and sample arms, and light in the arms recombining at the image plane to produce interferograms. However, the phase modulation in the reference arm is spatial, unlike PSI, which has temporal modulation. This is achieved by having the reference arm at a known off-axis angle. The periodicity of the resulting interferograms depends on this off-axis angle. Figure 1.4 shows a block diagram representation of OAI with the reference arm directed at a known off-axis angle.

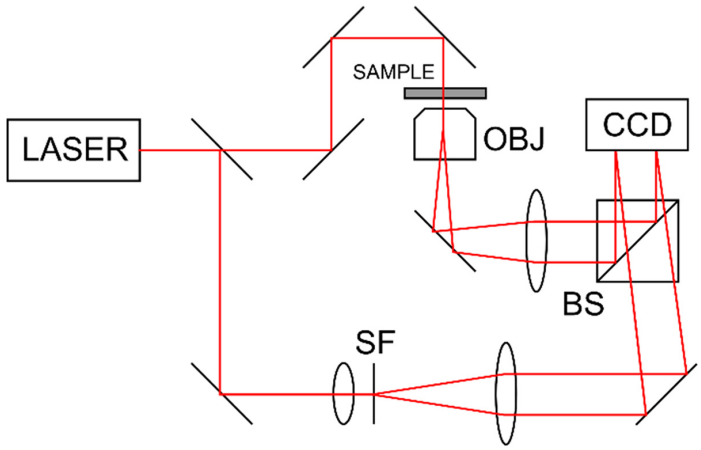

Figure 1.4: Block diagram of OAI based on Mach-Zehnder configuration with sample and reference arms. (image extracted from [47])

The major advantage of this method is that only one interferogram is required to reconstruct the phase image, unlike PSI which requires four interferograms. This results in a faster imaging process and the speed is only limited by the camera read-out speed, which also increases the temporal resolution. The phase is recovered by numerical Fresnel propagation or Fourier domain demodulation. The spatial resolution of OAI is limited by the off-axis angle as opposed to imaging optics in PSI.

There are variants of these two methods that have the same configuration but differ in methodology. Hilbert Phase Microscopy (HPM) [67] uses same configuration as OAI but uses the Hilbert transform for phase recovery. Similarly, Optical Quadrature Microscopy (OQM) uses same configuration as PSI but instead of obtaining four interferograms consecutively, the images are taken simultaneously by using different polarization states. This makes it comparable to OAI in terms of speed [68, 69]. A method called Interferometry with Triple Imaging Area (ITIA) was also introduced in [70]. ITIA uses the principles of OAI but multiplexes three OAI interferograms onto a single camera sensor. This overcomes the limitations of the field of view in OAI where a single image is unable to capture the entire area of interest of the sample. This may be of particular use in case of dynamically changing samples.

The methods mentioned in previous sections, such as PCM and DIC have also been modified into quantitative methods by incorporating the techniques of PSI and OAI. Spatial Light Interference Microscopy (SLIM) [65] is an example of a quantitative version of PCM, while Arnison *et al.* [71] from 2004 describe QPI using DIC. Another interferometric technique is described by Brandi and Wessel [72]. It uses a common-path second harmonic dispersion interferometry combined with polarization dependent phase detection. A technique called Quadriwave Lateral Shearing Interferometry (QWLSI) is also a quantitative version of DIC that uses a modified Hartmann mask instead of a Nomarski prism. It is compatible with white light illumination and uses a single interferogram for obtaining the phase image [73]. The company "Phasics" has developed wavefront sensors that rely on QWLSI to perform QPI. [74].

Since interference-based QPI uses interferograms, phase unwrapping algorithms are required for accurate phase recovery. This makes them computationally expensive. However, recent developments have led to better algorithms for phase unwrapping. Moreover, these methods usually exhibit the problems of phase and speckle noise due to the use of coherent monochromatic light. In recent years, common-path geometries have been adopted to minimize these effects.

Scanning-based and defocus-based methods do not require interferograms for phase recovery, and are also called Phase Retrieval (PR) methods. PR methods are useful because they only require intensity patterns for extracting the phase information of the object. Gerchberg-Saxton algorithm is one of the popular ways of obtaining phase information from the intensity patterns [75]. An example of scanning-based QPI method is Ptychography. It utilizes a beam of light incident on the sample which is moved with respect to the sample such that it scans the sample to create a sequential array of overlapping illuminated areas. The phase of the sample is recovered using a phase retrieval algorithm [76]. This method is label-free, quantitative, non-invasive, and capable of providing enhanced resolution. Ptychographic Microscopy (PM) is a ptychographic technique that uses an angularly

varying beam for illuminating the sample from multiple angles to record the image data. In this technique, an LED array sequentially illuminates the sample in different angles. There is no physical movement of the sample or the system, and the technique is capable of providing a resolution better than the limit set by the objective lens [77]. Ptychographic techniques can provide high resolution and wide field of view, but are slow due to the multiple steps involved in data acquisition and processing.

Defocus-based QPI methods are of special importance in this thesis. These methods require intensity patterns corresponding to the focal plane as well as in the planes above and below the focal plane (defocused intensity patterns) which are recombined in the Fourier domain to reconstruct a phase image of the sample. The common aspect of many defocus-based QPI methods is the use of iterative algorithms to obtain a converging solution to the phase problem. In Iterative Wave Function Reconstruction (IWFR), the phase solution is iteratively identified by comparing the measured defocus intensities with the defocus intensities from the calculated phase. These iterative methods preserve the spatial resolution of the imaging optics and do not suffer from phase and speckle noise as in the case of methods like OAI and PSI. However, these methods are computationally expensive due to the iterative algorithms and are not usable for real-time imaging.

Apart from iterative algorithm-based methods, another way to obtain phase information from intensity patterns is to linearize the relationship between the object phase and defocus intensities, thus simplifying the computational process. If the object is weakly absorbing, the Transport of Intensity Equation (TIE) is used to relate the derivative of intensity along the optical axis, to the phase function of the object [78]. Defocused intensity patterns are used to determine the derivative of intensity using finite difference methods. The TIE has a simple expression in the Fourier domain and the phase can be easily recovered using deconvolution. If the object has a slowly varying phase and weak absorption, then the Weak Object Transfer Function (WOTF) method [58] is useful. It is a non-iterative method and is based on principles of partially coherent illumination. It provides the phase information

by direct inversion of the phase optical transfer function using a Laplacian operator and hence does not require iterative algorithms. This makes it usable for live cell imaging. This method is also called the Contrast Transfer Function (CTF) method in X-ray imaging [79]. The TIE and CTF methods have also been combined to have the advantages of both methods [80]. These methods are non-invasive, speckle-free and computationally efficient. However, they can exhibit a noise problem depending on the defocus distance used.

The Optics Laboratory at Georgia Tech has developed two defocus-based 2D QPI methods namely Multifilter Phase Imaging with Partially Coherent Light (MFPI-PC) [48] and Phase Optical Transfer Function Recovery (POTFR) [49]. MFPI-PC has been extended to the non-paraxial case [81] and to the annular illumination case [82]. A special algorithm called Weighted Least Squares (WLS) was developed to optimize the results for the annular illumination case. MFPI-PC and its annular illumination case will be discussed in detail in Chpt. 2.

1.3.2 QPI Instrumentation

The implementation of various methods discussed in the previous subsection requires the development of compatible systems that can perform the necessary steps to obtain the desired end results. The purpose of developing a good system is to enable ubiquitous use of the particular method with high efficiency and cost-effectiveness. With time, new solutions to the limitations of existing systems are developed that take the research a step further. For example, to use PCM, one needs to use a phase contrast condenser with annular illumination and corresponding phase contrast objectives with compatible annular rings to enhance the contrast of the sample. Similarly, DIC requires the use of Wollaston or Nomarski prisms together with a polarizer and an analyzer, as a part of the microscope system, to correctly obtain a DIC image.

QPI methods also require the development of imaging systems that enable the light to interact with the sample in desired ways to obtain a phase image according to specific

methods. Various approaches are used to achieve the desired interaction. Systems may use an electrically tunable lens, an LED array, pupil modulation, a quatrefoil lens, spatial light modulation, Piezoelectric Transducer (PZT), or other approaches to overcome the limitations of conventional QPI systems, or to introduce new ways of implementing a particular QPI method depending on the application. For example, Fig. 1.3 shows PSI based on a Mach-Zehnder configuration where the phase can be modulated using a liquid crystal phase modulator, while Fig. 1.5 shows PSI based on a Michelson interferometer configuration wherein the phase modulation in the reference arm is achieved by moving the mirror using a PZT.

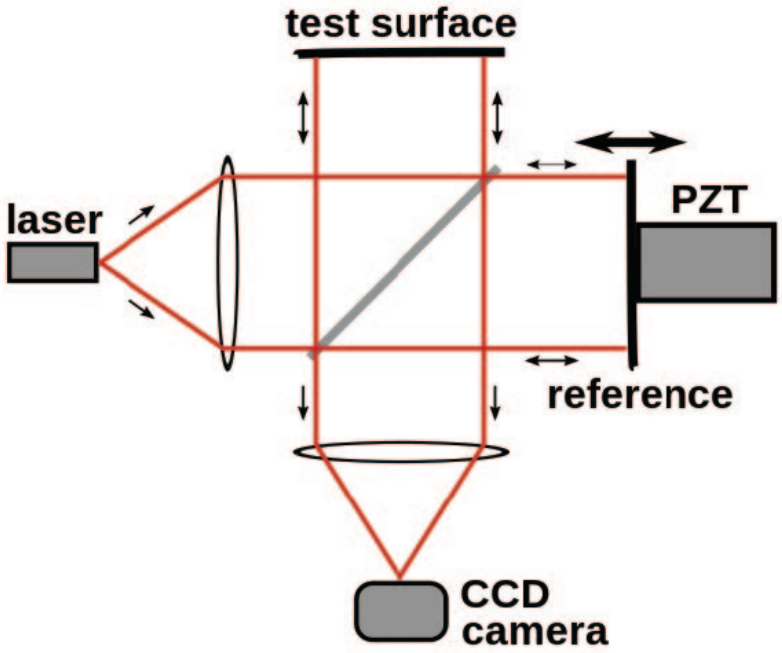

Figure 1.5: Block diagram of PSI based on a Michelson interferometer configuration. PZT = Piezoelectric Transducer

An Electrically Tunable Lens (ETL) is a type of lens that can undergo a change in shape depending on the amount of current passed to it. It has numerous applications in microscopy and imaging as it allows changing of focal length without making any changes to the physical configuration. Consequently, it has been used in QPI systems frequently. In conventional DHM, which follows the principles of OAI, a microscope objective is used

in the object arm that introduces phase distortion. Furthermore, using different microscope objectives results in the introduction of different phase distortions that can deteriorate the accuracy of the method. These distortions can be corrected by using appropriate numerical methods in post-processing, or by making changes to the physical configuration. By making the same distortions in the reference arm, the effect of those distortions can be compensated and no extensive correction is required in processing. One approach to match the distortions in the reference and object arms is to use ETL for matching the wavefronts of reference wave and the wavefront from different microscope objectives, by varying the current to the ETL. This does not require making any complex changes in the configuration and does not require use of any computationally expensive numerical methods for correcting the distortions. As a result, it allows for the use of the method in real-time imaging of biological cells. [83].

Another application of ETL is seen in the paper by Rodrigo and Alieva [84] for a faster response as compared to the liquid crystal spatial light modulators. The system implements a non-interferometric QPI technique to obtain the phase information of the sample in real-time. The emphasis of the system is on the use of quasi-monochromatic partially coherent illumination because of its advantages in circumventing the problem of speckle noise and parasitic reflections in the optical system. The described QPI system uses an LED as a partially coherent light source, microscope objective lens, tube lens, relay lens, ETL, and a high speed CMOS camera for recording the images. Another paper by Rodrigo, Soto, and Alieva [85] descibes a QPI system that obtains bright-field intensity images to obtain a 3D refractive index distribution of living cells. The images are axially scanned using a high-speed ETL in front of a CMOS camera. The system is capable of performing real-time 3D imaging of live cells and can produce a video of the changes observed in the cells over a period of time. This is done by configuring the ETL for continuous scanning in the direction of the optical axis in both up and down directions and having the CMOS camera record the images continuously over a period of time. Other ETL-based QPI systems in-

clude a self-interference digital holographic microscopy system with laser-based illumination, Michelson interferometer configuration, and the ability to reduce coherence-induced disturbances [86], a phase shifting DHM system with an ETL as a reliable phase-shifter device [87], and a TIE-based QPI technique with an ETL for through-focal scanning of the sample at 15 frames per second, allowing for dynamic cell imaging without the need for phase unwrapping algorithms [88]. With time, many such systems are being developed to perform high-speed QPI.

Use of LED array as an illumination source has also seen applications in QPI. A paper on 3D Differential Phase Contrast (DPC) microscopy by Chen *et al.* [89] uses a programmable LED array as a source of partially coherent illumination for capturing through-focal images with four different illumination patterns. The phase information is recovered using a 3D DPC model. Another paper by two of the authors from the above paper, Tian and Waller [90] published in the previous year derive the 2D WOTF for the method and experimentally validate the method using an LED array microscope to achieve QPI in real-time. Another paper by Lee *et al.* [91] uses a programmable three-color LED array as an illumination source. The emphasis of the system is in obtaining bright-field, dark-field and DPC images simultaneously using images in different color channels. The square LED array is programmed such that it has a circle at the center with half of it as red light and the other half as blue light. The part of the array outside the circle is programmed to be a green light. A color camera is used to capture a single shot image, and then the image is decomposed into three color-channel images. Image from the red channel combined with blue channel gives an image with full circle illumination and corresponds to a bright-field image. Whereas, the green channel image results from an oblique illumination from angles greater than the NA of the objective. As a result, it produces a dark-field image. DPC image is obtained by taking the ratio of difference in intensities in red channel and blue channel, to the summation of intensities in the two channels. The method described in the paper is termed as color-coded LED microscopy. LED array was also used in the FPM system

described in [77] to sequentially illuminate the sample from multiple angles and ultimately enhance the performance of the system beyond the limit set by its optical components.

Other approaches like the use of Spatial Light Modulators (SLM) are also used in various imaging systems. A tomographic phase microscopy system is described in [92] that uses limited angle of projections. This system uses a Mach-Zehnder configuration based DHM technique. The main use of SLM in this system is to have a "vibration-free, diffraction-based beam deflection" which is used for acquiring holograms by illuminating the samples from different angles. Another system described in [93] uses SLM and digital image processing to recover phase information of the sample. The SLM produces a set of defocused images at the CCD plane which are further processed numerically. The system contains no moving elements. A novel TIE-based QPI system described in [94] circumvents the requirement of defocus-based scanning by using Computer Generated Hologram (CGH) to record defocused intensity patterns of the sample. The CGH is displayed on an SLM which provides various focal lengths and orientations to allow the camera to record multiple defocused intensity patterns. Further, the higher order approximation is used with TIE to reconstruct the phase images. Another novel system uses a quatrefoil lens for a "partitioned detection aperture", instead of an SLM approach, to perform high resolution 3D phase imaging of various samples, as described in [95] and [96].

PZT based scanning has been used in many QPI systems. A paper by Mehta and Srivastava [97] as well as another paper by Iwai *et al.* [98] describe the use of PZT for moving the reference mirror in a Michelson interferometer-based PSH system. However, the two systems are independent and differ in details of their operation. Similarly, [99] uses PZT in a Mach-Zehnder based system employing phase shifting interferometry. As described previously, defocus-based QPI techniques require only defocused intensity patterns as input without the need for any interferograms or extensive phase unwrapping algorithms. To this end, PZT serves as a valuable device in moving either the camera or the objective through various defocus planes. The Optics Laboratory at Georgia Tech has developed a QPI sys-

tem comprising of a microscope, a camera, a PZT device, and rotation stages controlled by a motion controller, integrated and operated via a LabVIEW interface. The system is capable of performing QPI measurements on 2D as well as 3D objects. Chpt. 3 contains a detailed discussion of the system and its operation.

1.3.3 Annular Illumination

Annular illumination has been of interest to the scientific community since the early investigations of the effects of annular apertures by Airy [100]. Since then, this illumination has been successfully applied to numerous microscopy and imaging techniques. Illuminating two equal pinholes in this manner has shown the additional light blocked by the condenser leads to increased resolution [101]. Then, Noda [102] calculated the 3D phase transfer function of a microscope system with an annular pupil in the source function and used computer reconstruction to generate phase images showing fine details in cultured tobacco cells. A resolution of 90nm was attained with a lab microscope by replacing the standard bright-field condenser with a cardioid annular condenser [103]. Sheppard [104] found that the use of annular illumination provided a linear response over a wider range of phase gradients with a better resolution and improved low-frequency response. Annular illumination is fundamental in enhancing the contrast of fine features in phase contrast microscopy (PCM) as developed by Zernike [12, 13]. Another method by Hisaka [105] used annular illumination in phase contrast scanning optical microscopy with separate amplitude and phase imaging. In confocal microscopy, use of annular illumination improved the image quality [106, 107], produced narrower point spread functions and improved resolution [108, 109]. Annular illumination has also been applied to numerous other fields: third harmonic generation (THG) microscopy [110], focal modulation microscopy (FMM) [111], dark-field Brillouin microscopy [112], localized surface plasmon microscopy [113, 114], multiphoton microscopy [115, 116], stimulated emission depletion microscopy [117], and fluorescence microscopy [118, 119]. In 2018, Ma *et al.* [120] developed spatially incoher-

ent annular illumination microscopy (SAIM) that uses annular LED array for illumination. It is a direct imaging method and the annular illumination design provides better optical sectioning and lateral resolution compared to Koehler illumination. This method has also been used for label-free 3D imaging of weakly absorbing samples [121].

In addition to the various microscopy techniques, annular illumination has been applied to 2D and 3D QPI. In 2D QPI, TIE is one of the frequently used approaches due to its simple requirements and deterministic nature. Partial coherence with conventional circular aperture leads to lowered phase contrast and strong low frequency artifacts in TIE imaging. Zuo *et al.* [122] resolved this problem by using annular illumination which resulted in in improved resolution. In their paper, annular illumination was used to optimize the weak-object transfer function (WOTF) to obtain an improved response over both low and high spatial frequencies, and to resolve the noise-resolution trade-off in TIE imaging. Huang *et al.* [123] proposed a phase retrieval method using annular and annular sector pupils whereas Li *et al.* [124] identified that a thin annulus with an NA matching that of the objective is the optimal illumination pattern for TIE-based QPI. An annular LED array was also used in the system to implement DHM and TIE in rapid succession [125]. Other applications of annular illumination in 2D QPI include quantitative DPC [126, 127], color-multiplexed DPC [128, 129], FPM [130–134], and single-shot wavelength selective QPM [135]. Li *et al.* [136] also used annular illumination through a programmable LED array for phase imaging with better noise performance and higher resolution. The use of annular illumination and the development of WLS-MFPI-PC method by Bao in [82] was useful in this research, and is described in Chpt. 2. In 3D QPI, tomography is a frequently used approach to obtain information of the sample from multiple angles. Li *et al.* [137, 138] improved the intensity diffraction tomography (IDT) technique by incorporating annular illumination using a programmable LED array for reconstructing 3D refractive index distributions. A novel tomographic technique utilized two disk illumination apertures and one annular aperture to combine multi-frequency components for improved resolution and

Signal-to-Noise Ratio (SNR) [139]. An optimization analysis for use of partially coherent illumination with ODT by Li *et al.* [140] compared the performance for multiple illumination patterns. The LED array sequentially illuminated the sample from multiple angles and allowed collection of data without moving the sample or the system. Li *et al.* [141] also developed a computational technique for annular QPI and RI tomography. Huang [142] calculated the 3D phase optical transfer function for multiple illumination types including the annular type, which provided a basis for optimizing QPI in various applications.

Apart from the various microscopy and QPI techniques, annular illumination has also been used to advantage in photolithography systems and has led to improvement in resolution, depth of focus, and contrast [143–145]. More recently annular illumination has been applied to the latest Extreme Ultraviolet (EUV) technology to obtain half-pitch resolutions of 8nm [146]. The field of ophthalmoscopy has also benefitted from the use of annular illumination with its application in scanning laser ophthalmoscopy [147], adaptive optics scanning ophthalmoscopy [148], and the development of devices like digital micromirror based ophthalmoscope [149]. Beyond these domains, annular illumination has also been applied to scanning electron microscopy [150], silicon wafer inspection techniques [151], X-ray imaging [152], imaging of bones and tissues [153, 154], and optical micromachining [155].

The present work is a detailed quantitative comparison of disk and annular illumination as a function of the resulting phase image spatial frequency response. This work is based on resolution measurements made with a standard-type phase test chart rather than based on specific objects such as beads, optical fibers, lenslet arrays, phantoms, biological cells, etc. Further these experimental measurements are then correlated with annular illumination phase imaging theoretical predictions. In the following section, the objectives of this research are delineated and an overview of the various sections of the thesis is provided.

1.4 Research Objectives and Thesis Overview

The goal of this thesis is two-fold. The primary objective is to compare the performance of disk and annular illumination using QPI methods developed at the optics laboratory and validate the theoretical predictions stating potential advantages of using annular illumination. The 2D QPI method used in this thesis is Weighted Least Squares Multifilter Phase Imaging with Partially Coherent Light (WLS-MFPI-PC) [82] under non-paraxial regime [81, 156], and with disk and annular illumination [82]. This technique is defocus-based and uses multiple defocused intensity patterns as input data. Furthermore, the method is deterministic, and hence does not require any iterative algorithms for phase recovery. Chapter 2 describes the theory of the WLS-MFPI-PC method used in this research with a summary of the developments leading upto the WLS-MFPI-PC method and all the relevant equations. Chapter 4 discusses the experimental results and the analysis of the phase images using spatial frequency response. The performance of the disk and annular illumination types as a function of spatial frequency is analyzed and compared to the theoretical model from [82].

The second goal of this research is to develop a state-of-the-art microscope system for performing experiments in 2D QPI as well as 3D QPI, along with the capability to be used for conventional PCM and DIC microscopy. This system comprises of a microscope system, a camera, a piezoelectric transducer connected to the microscope objective, a motion controller and two rotation stages with servo-motors to rotate the sample. This system is capable of collecting the required defocused intensity patterns over a wide range of angles, for use as input data to the 2D QPI and 3D QPI methods developed at the Optics Laboratory at Georgia Tech. Chapter 3 describes the development of this new QPI system. The results discussed in Chpt. 4 are based on the experiments performed using the system described in Chpt. 3.

Lastly, based on the work described in this thesis, a summary of the research work is

provided and avenues for future developments are identified. Chapter 5 provides concluding remarks for the work and discusses the future work that can be undertaken to make further developments in the field of QPI and make it a commercially viable method for industrial applications.

CHAPTER 2

PRINCIPLES OF QPI

The Optics Laboratory at Georgia Tech has developed two 2D QPI techniques namely Multifilter Phase Imaging with Partially Coherent Light (MFPI-PC), and Phase Optical Transfer Function Recovery (POTFR). In this chapter, the principles of MFPI-PC for paraxial case as developed by Micah Jenkins [47, 48], and the extension of the method to nonparaxial regime and annular illumination case, as developed by Yijun Bao [59, 81, 82, 156] are discussed. The WLS-MFPI-PC method was used to reconstruct phase images for disk and annular cases for this research.

2.1 Paraxial MFPI-PC

Propagation based phase retrieval methods are advantageous over methods like OAI and PSI, as the only required input is in the form of defocused intensity patterns and there is no need for phase unwrapping (Chpt. 1). Some methods use iterative algorithms for recovering the phase information of the light transmitted through the sample. However, deterministic phase retrieval using Transport of Intensity Equation (TIE) provides another way of retrieving the phase information, without the need for an iterative algorithm.

The TIE is derived from the paraxial scalar wave equation [78] and relates the derivative of intensity along the optical axis with the phase of the light. It is shown below:

$$\frac{\partial \boldsymbol{I}(\mathbf{r}, z)}{\partial z} = -\left(\frac{\lambda}{2\pi}\right) \nabla_{x,y} \cdot [\boldsymbol{I}(\boldsymbol{r}, z) \nabla_{x,y} \phi(\boldsymbol{r}, z)] \tag{2.1}$$

where λ is wavelength, ϕ is the unknown phase, I is intensity, and $\boldsymbol{r}$ is the position vector given by $\boldsymbol{r} = x\hat{x} + y\hat{y}$. The quantity $\nabla_{x,y}$ is the gradient operator in the lateral dimensions (x, y). As described in [157], if the RHS is expanded further, one term is

$\nabla I(\boldsymbol{r}, z)\nabla\phi(\boldsymbol{r}, z)$ which is dependent on the slope of the local wavefront, while the other term is $I(\boldsymbol{r}, z)\nabla^2\phi(\boldsymbol{r}, z)$ which is dependent on the curvature of the local wavefront. Therefore, this equation can be physically interpreted as a relationship between the intensity and the slope and curvature of the local wavefront, as the wave propagates in the axial direction.

The main quantity of interest is the unknown phase ϕ which contains the phase information of the light transmitted through the object (phase function of the object). To obtain ϕ from inversion of TIE, it is necessary to have knowledge of the axial derivative of intensity. Conventionally, this term $\frac{\partial I}{\partial z}$ is calculated using the intensity difference between two defocus planes (one above and one below the focal plane) and using the finite difference formula as given below [158, 159]:

$$\frac{\partial \boldsymbol{I}(\boldsymbol{r}, 0)}{\partial z} \approx \frac{I(\boldsymbol{r}, \Delta z) - I(\boldsymbol{r}, -\Delta z)}{2\Delta z} \tag{2.2}$$

The accuracy of the approximation depends on the defocus distance Δz. The smaller the defocus distance, the better is the accuracy of Eq. (2.2). However, as described in [158], unlike the ideal case, the defocus distance cannot be too small due to the presence of noise effects and nonlinearity errors. Hence, there is a trade-off between the noise performance and resolution of the image depending on the defocus distance. To overcome this problem, methods like *higher order finite difference* [159, 160] or *noise-reduction finite difference* [159, 161] could be used, with advantages and disadvantages of their own.

In 2013, Zuo *et al.* [159] proved that all these finite difference methods can be expressed as special cases of one method based on a digital signal processing approach, wherein the axial derivative of intensity is estimated by convolution with Savitzky-Golay Differentiation Filters (SGDF). The general expression for the various finite difference methods and the unified SGDF method is given by: [48, 157]

$$\frac{\partial \boldsymbol{I}(\boldsymbol{r}, 0)}{\partial z} = \sum_{j=-n}^{n} \frac{a_j \boldsymbol{I}(\boldsymbol{r}, j\Delta z)}{\Delta z} \tag{2.3}$$

where LHS is the intensity derivative at the focal plane, Δz is the defocus distance, j is the image number and n is the half-data length corresponding to $2n + 1$ total number of images. The main difference between the methods lies in the coefficient a_j [159]. The expressions for a_j are different for different finite difference methods but can be arrived at, by convolution with SGDF with coefficients $h_{\mathrm{SG}}(j) = (a_j/\Delta z)$. This $h_{\mathrm{SG}}(j)$ can be calculated using equations (10), (11), and (12) from [159].

The SGDF approach is, as described in [159], "an equivalent convolution solution for differentiation of data by least-squares polynomial fitting." Furthermore, SGDF is a type-III Finite Impulse Response (FIR) filter with anti-symmetric coefficients and central coefficient always zero. The SGDFs for all odd orders are same as the next highest even order, so only odd orders are used in the phase retrieval process. The phase estimated using TIE inversion can be expressed as a low-pass filtered version of the actual phase, as shown in Eq. 25) of [159]. Analysis of the nature of the inherent low-pass-filtered aspect of SGDFs reveals that as the order of the SGDFs is increased, the effect of low pass filter is reduced, which results in better recovery of wider range of spatial frequencies. However, higher orders also suffer from poor noise effects. As a result, it can be said that lower orders of SGDF are better at resolving lower spatial frequency components with better noise performance, but they cannot recover higher spatial frequencies due to their limited response. This means that no single order of SGDF can recover the full range of spatial frequencies reliably.

This presents a conundrum which can be resolved using Optimal Frequency Selection (OFS) method [159]. OFS method effectively selects the best performance range of spatial frequencies for each order of SGDF and uses that SGDF order to recover only the selected range of spatial frequencies. This is done in [159] by using a 0.3dB cutoff for amplitude in the pass band for each order of SGDF. This cutoff gives the higher limit of the frequency that can be "reliably retrieved" for the given order of SGDF. Furthermore, the lowest order of SGDF satisfying the amplitude requirements is selected for recovering the selected range

of spatial frequencies, as it provides better noise performance. So, the OFS method works by first estimating the axial intensity derivatives by convolution with multiple orders of SGDF, then inverting TIE to obtain phase distribution for all the orders of SGDF, and then using a complementary filter bank in the spatial frequency domain to select particular ranges of frequencies for each SGDF order [157].

The last step of this method comes after the phase information from various SGDF orders is recovered and particular spatial frequency filters are applied. Generally, a low-pass filter is applied on the lowest SGDF order and a high-pass filter is applied on the highest SGDF order. Spatial frequency band-pass filters are applied on all the orders in between, and the filters have a different pass-band for different SGDF orders depending on the range of spatial frequencies selected for the particular SGDF order. In the last step, the phase information from all the orders is combined into a composite phase image.

Since methods like the one described above use multiple spatial frequency filters in the post-processing for producing a composite phase image, these methods are termed as "Multifilter Phase Imaging (MFPI)" methods by Jenkins [48]. Similarly, the relationship between estimated phase and the actual phase of the light through the object (such as Eq. (25) from [159]) is termed as "Phase Transfer Function (PTF)". Since the method described in [159] assumes coherent illumination, the method is termed as "Multifilter Phase Imaging with Coherent Light (MFPI-C)." Jenkins in his paper [48] provides a valuable extension to MFPI-C by extending the method to partially-coherent regime and calculating the corresponding PTFs. This new method, as described in detail in [48] is termed as "Multifilter Phase Imaging with Partially Coherent Light (MFPI-PC)," and uses Streibl's three-dimensional Optical Transfer Function (OTF) theory [162] for calculating the partially coherent PTFs.

The requirement of a coherent illumination limits the use of MFPI-C method, as most of the standard microscope systems do not have that capability. Therefore, extending the MFPI-C method to partially coherent illumination not only broadens the scope of the the-

ory, but also makes it possible to perform QPI on standard microscope systems. It is a step in the direction of making QPI more accessible and economical, while having the ability to perform QPI without making extensive changes to the standard microscope systems. A mercury arc lamp together with an interference filter acts as a good source of partially coherent illumination. Koehler illumination is used for uniform illumination of the sample, which also controls the partial spatial coherence of the illumination. The partial coherence arises from the extended nature of the illumination. If the source is a "point source," the amplitudes of the waves add up coherently in the image plane. However, due to the extended nature of the source, each point source in the lamp illuminates the sample with plane waves that travel different path lengths. As a result, at the image plane, the intensities of the plane waves are incoherently added, which defines the Phase Optical Transfer Function (POTF) of the system.

In [48, 162], the 3D spectrum of image intensity is given as follows:

$$\tilde{I} = B\boldsymbol{\delta}(\boldsymbol{\rho},\eta) + \tilde{\phi}(\boldsymbol{\rho},\eta)T_{\mathrm{P}}^{(3)}(\boldsymbol{\rho},\eta) + \tilde{A}(\boldsymbol{\rho},\eta)T_{\mathrm{A}}^{(3)}(\boldsymbol{\rho},\eta) \tag{2.4}$$

where B is the background intensity, $T_{\mathrm{P}}^{(3)}(\boldsymbol{\rho},\eta)$ is the 3D Phase Optical Transfer Function (POTF) and $T_{\mathrm{A}}^{(3)}(\boldsymbol{\rho},\eta)$ is the 3D Amplitude Optical Transfer Function (AOTF). The quantity $\boldsymbol{\rho}$ is the lateral spatial frequency given by $\boldsymbol{\rho} = \rho_x\hat{\rho_x} + \rho_y\hat{\rho_y}$ while η is the longitudinal spatial frequency coordinate. Furthermore, AOTF is an even function with $T_{\mathrm{A}}^{(3)}(\boldsymbol{\rho},\eta) = T_{\mathrm{A}}^{(3)}(\boldsymbol{\rho},-\eta)$ while POTF is an odd function with $T_{\mathrm{P}}^{(3)}(\boldsymbol{\rho},\eta) = -T_{\mathrm{P}}^{(3)}(\boldsymbol{\rho},-\eta)$. Since SGDF is odd-symmetric, convolution of intensity spectrum with SGDF results in decoupling of phase and amplitude information. The shapes of AOTF and POTF are dependent on the coherence parameter (S) given by the ratio of condenser numerical aperture to that of the objective numerical aperture, as given below [48]:

$$S = NA_{\mathrm{c}}/NA_{\mathrm{o}} \tag{2.5}$$

Like MFPI-C, MFPI-PC also estimates the axial derivative of intensity by convolution with SGDF, given by Eq. (2.3). Jenkins calculated the lateral Fourier Spectrum of this intensity derivative by multiplying the POTF with SGDF frequency response given by $H_{\mathrm{SG}}(e^{j2\pi\eta})$ and integrating it along the axial frequency co-ordinate as given by equations (5a) and (5b) from [48], which are repeated below for the reader:

$$\frac{\mathrm{d}I(\boldsymbol{\rho})}{\mathrm{d}z} = \tilde{\phi}(\boldsymbol{\rho}) T_{\mathrm{P}}^{(2)}(\boldsymbol{\rho}) \tag{2.6}$$

$$T_{\mathrm{P}}^{(2)}(\boldsymbol{\rho}) = \frac{4\pi}{\lambda} \int H_{\mathrm{SG}}(e^{j2\pi n}) T_{\mathrm{P}}^{(3)}(\boldsymbol{\rho}, \eta) \mathrm{d}\eta \tag{2.7}$$

Here $\tilde{\phi}$ is the 2D object phase spectrum and $j = \sqrt{-1}$. The term $T_{\mathrm{P}}^{(3)}(\boldsymbol{\rho}, \eta)$ is the 3D POTF and can be calculated using Eq. (27) from [162] and is repeated below:

$$T_{\mathrm{P}}^{(3)}(\boldsymbol{\rho}, \eta) = \frac{i\lambda}{4\pi} \int \tilde{p}(\boldsymbol{\rho'} + \boldsymbol{\rho}/2)[\tilde{S}(\boldsymbol{\rho'} + \boldsymbol{\rho}/2) - \tilde{S}(\boldsymbol{\rho'} - \boldsymbol{\rho}/2)]\tilde{p}^*(\boldsymbol{\rho'} - \boldsymbol{\rho}/2)\boldsymbol{\delta}(\eta + \lambda\boldsymbol{\rho} \cdot \boldsymbol{\rho'})\mathrm{d}^2\boldsymbol{\rho'} \tag{2.8}$$

where $\tilde{S}(\boldsymbol{\rho})$ is the source function and the $\tilde{p}(\boldsymbol{\rho})$ is the pupil function. The quantities $\boldsymbol{\rho}$ and η are the lateral and longitudinal frequencies.

The Eq. (2.7) is termed as the Phase Contrast Transfer Function (PCTF) for finite amount of defocus. Similarly, the PCTF for weakly defocused case (WD-PCTF) is given in [48] as follows:

$$T_{\mathrm{PW}}^{(2)}(\boldsymbol{\rho}) = \frac{4\pi}{\lambda} \int j2\pi\eta T_{\mathrm{P}}^{(3)}(\boldsymbol{\rho}, \eta) \mathrm{d}\eta \tag{2.9}$$

The TIE for a pure phase object can be given by assuming no variation in intensity. As a result, when the RHS of Eq. (2.1) is expanded, the $\nabla I(\boldsymbol{r}, z)\nabla\phi(\boldsymbol{r}, z)$ term becomes zero

and only $I(\boldsymbol{r}, z)\nabla^2\phi(\boldsymbol{r}, z)$ term remains as shown below:

$$\frac{\partial \boldsymbol{I}(\boldsymbol{r}, z)}{\partial z} = -\left(\frac{\lambda}{2\pi}\right) I(\boldsymbol{r}, z)\nabla^2\phi(\boldsymbol{r}, z) \tag{2.10}$$

Taking Fourier Transform of this equation leads to the equation given below, which is also the Eq. 7(a) in [48]:

$$\frac{\mathrm{d}\tilde{I}(\boldsymbol{\rho})}{\mathrm{d}z} = \tilde{\phi}(\boldsymbol{\rho})2\pi\bar{\lambda}B\rho^2 \tag{2.11}$$

The above equation provides the PCTF for pure phase object, obtained from TIE, which is also the Eq. (7b) in [48]:

$$T^{(2)}_{\mathrm{P_{TIE}}}(\boldsymbol{\rho}) = 2\pi\bar{\lambda}B\rho^2 \tag{2.12}$$

Here, $\bar{\lambda}$ is the mean wavelength of the quasi-monochromatic source, and $\rho = |\boldsymbol{\rho}|$.

The ratio of the PCTF obtained from the estimated intensity derivative to the PCTF obtained from TIE, gives the partially coherent PTFs, as described by Eq. (9) in [48] and repeated below:

$$\mathrm{PTF}(\boldsymbol{\rho}) = T^{(2)}_{\mathrm{P}}(\boldsymbol{\rho})/T^{(2)}_{\mathrm{P_{TIE}}}(\boldsymbol{\rho}) \tag{2.13}$$

In MFPI-PC, TIE inversion is used to obtain the phase information, and the spatial frequency cutoffs for spatial filters in the post processing are given by a comparison of $T^{(2)}_P$ with $T^{(2)}_{\mathrm{P_W}}$. This comparison gives the cutoff ratio $\xi = T^{(2)}_{\mathrm{P}}(\boldsymbol{\rho_c})/T^{(2)}_{\mathrm{P_W}}(\boldsymbol{\rho_c})$, as given in Eq. (8) of [48]. In MFPI-PC method, the composite PTF given by Eq. (2.13) approaches the ratio ξ. This cutoff ratio provides the cutoff frequencies $\boldsymbol{\rho_c}$ that are used for designing the spatial filters to be used with various SGDF orders, so that the best performance of all the SGDF orders can be used to create a composite phase image. This works in the same way as the 0.3dB cutoff in the MFPI-C method. In [48], the threshold for this ratio is chosen to

be 0.99, below which the frequency is not recovered with the given SGDF order. Finally, the phase information calculated from all the orders of the SGDF, after application of the spatial filters, is combined together in the spatial frequency domain to give the composite phase as shown below (for $2n-1$ orders of SGDF):

$$\tilde{\phi}(\boldsymbol{\rho})_{\text{composite}} = \tilde{\phi}(\boldsymbol{\rho})_1 + \tilde{\phi}(\boldsymbol{\rho})_2 + \tilde{\phi}(\boldsymbol{\rho})_3 ... + \tilde{\phi}(\boldsymbol{\rho})_{(2n-1)} \tag{2.14}$$

Figure 2.1 shows the block diagram representation of the MFPI-C and MFPI-PC methods as developed by Zuo [159] and Jenkins [48]. The PTFs obtained for partially coherent illumination are different, and are used for implementing the spatial frequency filters after the TIE inversion step.

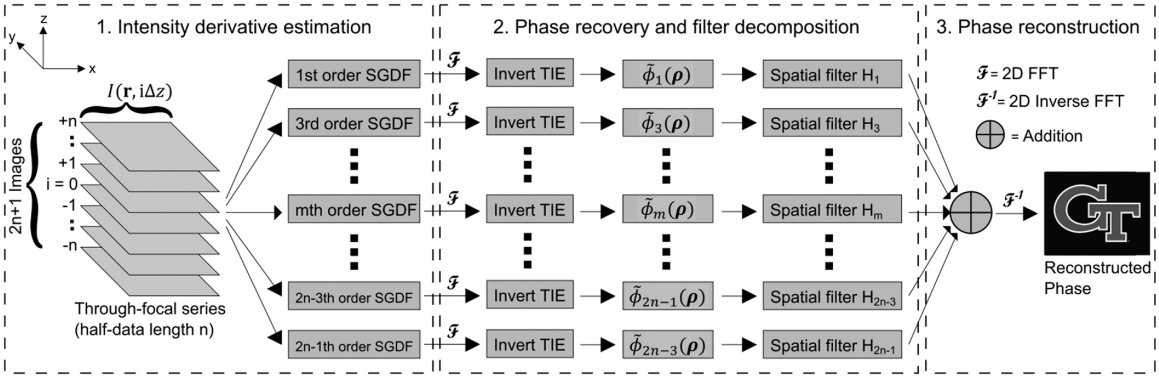

Figure 2.1: Block Diagram of MFPI-C and MFPI-PC methods. The MFPI-PC method developed by Jenkins [48] uses 3D OTF theory and TIE to obtain partially coherent PTFs for phase recovery. (image from [48])

Since, Streibl's 3D OTF theory assumes paraxial case, the POTF, $T_{\text{P}}^{(3)}(\boldsymbol{\rho}, \eta)$, is also based on paraxial approximation. Since MFPI-PC uses $T_{\text{P}}^{(3)}(\boldsymbol{\rho}, \eta)$ in evaluation of $T_{\text{P}}^{(2)}(\boldsymbol{\rho})$ and $T_{\text{P}_{\text{TIE}}}^{(2)}(\boldsymbol{\rho})$, which are then used in calculating the partially coherent PTFs as shown in Eq. (2.12), the MFPI-PC method inherits the paraxial approximation, and can be used reliably only for paraxial case.

2.2 Nonparaxial MFPI-PC

Considering the limitations of paraxial approximation in solving the problems in most of the imaging systems and scenarios, especially in systems with high Numerical Aperture (NA), it is imperative to extend the approach of MFPI-PC to nonparaxial case. This was done by Yijun Bao in [81, 156]. Modifying just the PTFs or PCTFs does not suffice as the paraxial approximation goes back to Streibl's 3D OTF formalism [162].

To extend the MFPI-PC method to nonparaxial case, Yijun Bao re-calculated the 3D POTF, without the paraxial approximations [81, 82]. Streibl in [162] invokes the paraxial approximation for expanding the square roots using Taylor series in Eq. (19) of [162]. Without the approximation, the general nonparaxial 3D POTF is given by Eq. (1) in [81]. Furthermore, Bao also provided an obliquity factor (OF) correction to the Green's function solution that forms the basis of Streibl's 3D OTF theory. This correction is needed to fully incorporate the nonparaxial condition. Details of this obliquity factor are provided in the Appendix A of [81]. After the OF modification to the generalized nonparaxial 3D POTF, it is given by Eq. (4) in [81], as repeated below:

$$\begin{aligned} T_{\mathrm{P}}^{(3)}(\boldsymbol{\rho},\eta) = \frac{i\lambda}{4\pi}\int \tilde{p}(\boldsymbol{\rho'}+\boldsymbol{\rho}/2)\tilde{p}^{*}(\boldsymbol{\rho'}-\boldsymbol{\rho}/2)\times \\ [\tilde{S}(\boldsymbol{\rho}+\boldsymbol{\rho}/2)-\tilde{S}(\boldsymbol{\rho}-\boldsymbol{\rho}/2)] \\ \times\,\delta(\eta+\sqrt{\lambda^{-2}-(\boldsymbol{\rho'}-\boldsymbol{\rho}/2)^{2}}-\sqrt{\lambda^{-2}-(\boldsymbol{\rho'}+\boldsymbol{\rho}/2)^{2}})\mathrm{d}^{2}\boldsymbol{\rho'} \end{aligned} \tag{2.15}$$

where $\tilde{S}(\boldsymbol{\rho})$ is the source function and $\tilde{p}(\boldsymbol{\rho})$ is the pupil function. nonparaxial MFPI-PC method uses Weakly-Defocused Phase Contrast Transfer Function (WD-PCTF) inversion instead of the TIE inversion for obtaining the phase information. The PCTF for finite defocus ($T_{\mathrm{P}}^{(2)}$) and the WD-PCTF ($T_{\mathrm{P_W}}^{(2)}$) can be found for the nonparaxial case by using Eq. (2.14) with Eq. (2.7) and Eq. (2.9) respectively. These substitutions provide the PTF, which is used as a cutoff ratio $\xi = T_{\mathrm{P}}^{(2)}(\boldsymbol{\rho})/T_{\mathrm{P_W}}^{(2)}(\boldsymbol{\rho})$ for the spatial frequency filters. Further

calculations of the composite phase from PTFs, using OFS method and the combination of phase information in the spatial frequency domain is same as in the paraxial MFPI-PC case, except the spatial filters are implemented based on the cutoff frequencies calculated for nonparaxial case.

Figure 2.2 shows the block-diagram representation of the nonparaxial MFPI-PC, as described in [81, 156]. The phase recovery from TIE inversion is replaced by inversion of WD-PCTF given by $T^{(2)}_{\mathrm{PW}}$ which can be calculated from Eq. (2.9) and Eq. (2.15). This change incorporates the nonparaxial effect and broadens the scope of the paraxial MFPI-PC method.

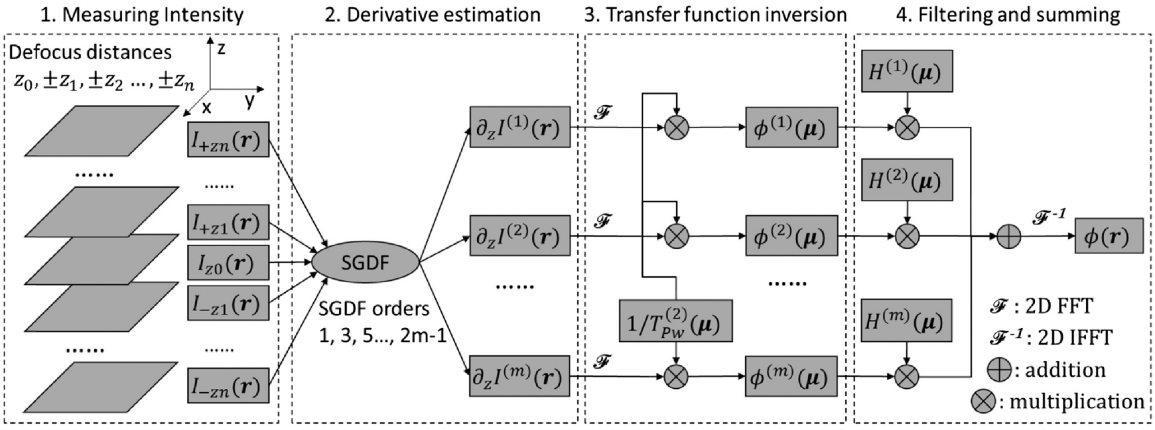

Figure 2.2: Block diagram representation of the nonparaxial MFPI-PC method, based on the generalized nonparaxial 3D POTF, as obtained by Bao in [81] The TIE inversion is replaced by WD-PCTF inversion. (image from [81])

All the methods described above use a disk illumination assumption for the source function $\tilde{S}(\boldsymbol{\rho})$. However, in recent years, annular illumination has been used in multiple imaging techniques and have been found to be advantageous in improving resolution, improving phase contrast, and obtaining better phase images [122, 136]. Consequently, it was imperative that the MFPI-PC method be extended to annular illumination. Bao *et al.* in [82] extended the MFPI-PC method to use of annular illumination, and further improved the method by developing a "Weighted-Least-Squares (WLS)" algorithm in order to provide proper weight to the various SGDF orders.

2.3 WLS-MFPI-PC with Annular Illumination

In the MFPI-PC methods described previously, the source was assumed to be a disk illumination source with the source function $\tilde{S}(\boldsymbol{\rho})$ given by Eq. (6) in [81]:

$$\tilde{S}(\boldsymbol{\rho}) = \begin{cases} 1, & |\boldsymbol{\rho}| \leq \rho_{\mathrm{s}} \\ 0, & |\boldsymbol{\rho}| > \rho_{\mathrm{s}} \end{cases} \tag{2.16}$$

where $\rho_s = NA_{\mathrm{c}}/\lambda$ and NA_{c} is the numerical aperture of the condenser. However, for the annular illumination case, the source function can be given by Eq. (4) in [82]:

$$\tilde{S}(\boldsymbol{\rho}) = \begin{cases} 0, & |\boldsymbol{\rho}| < \rho_{\mathrm{si}} \\ 1, & \rho_{\mathrm{si}} \leq |\boldsymbol{\rho}| \leq \rho_{\mathrm{s}} \\ 0, & |\boldsymbol{\rho}| > \rho_{\mathrm{s}} \end{cases} \tag{2.17}$$

where $\rho_{\mathrm{s}} = NA_{\mathrm{c}}/\lambda$ and $\rho_{\mathrm{si}} = NA_{\mathrm{ci}}/\lambda$ where NA_{c} and NA_{ci} are numerical apertures corresponding to the outer and inner radii of the annular source respectively. Figure 2.3 shows the schematic representation of the annular source.

In both disk and annular illumination cases, the objectives used are of the same kind with circular apertures, and hence the pupil function remains the same, as given by Eq. (5) in [81]:

$$\tilde{p}(\boldsymbol{\rho}) = \begin{cases} 1, & |\boldsymbol{\rho}| \leq \rho_{\mathrm{p}} \\ 0, & |\boldsymbol{\rho}| > \rho_{\mathrm{p}} \end{cases} \tag{2.18}$$

where $\rho_{\mathrm{p}} = NA_{\mathrm{o}}/\lambda$ and NA_{o} is the numerical aperture of the objective.

These functions are useful in calculating the 3D POTF corresponding to the nonparaxial case, as given by Eq. (2.15). The Eq. (2.15) is valid for disk illumination as well as annular illumination, and the generalized 3D POTF for the annular case can be expressed as a

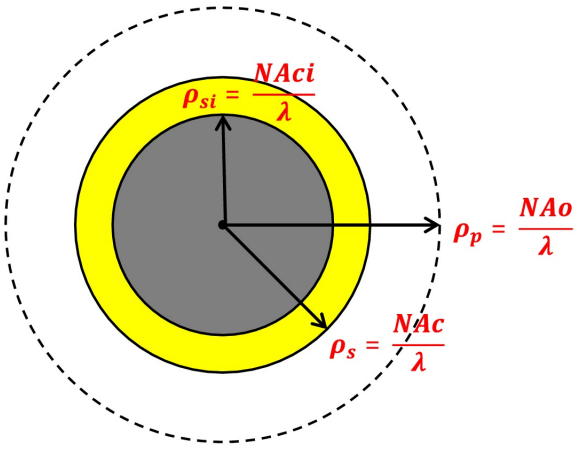

Figure 2.3: Schematic representation of the annular illumination source in the spatial frequency domain. NA_{c} and NA_{ci} are the numerical apertures of the outer and inner radii of the annulus, while the NAo corresponds to numerical aperture of the objective. (Image from [82])

difference of the two POTFs of disk illumination sources corresponding to inner and outer radii of the annulus. It is given in terms of $T_{\mathrm{P}}^{(3)}(\boldsymbol{\rho}, \eta)$ by Eq. (5) in [82]:

$$T_{\mathrm{P}}^{(3)}(\boldsymbol{\rho}, \eta; \rho_{\mathrm{si}}, \rho_{\mathrm{s}}) = T_{\mathrm{P}}^{(3)}(\boldsymbol{\rho}, \eta; 0, \rho_{\mathrm{s}}) - T_{\mathrm{P}}^{(3)}(\boldsymbol{\rho}, \eta; 0, \rho_{\mathrm{si}}) \tag{2.19}$$

The normalized 3D POTF for annular source is expressed as a weighted difference of the normalized 3D POTFs of the disk sources, as described by Eq. (10) in [82]:

$$\tilde{T}_{\mathrm{P}}^{(3)}(\boldsymbol{\rho}; \eta, \rho_{\mathrm{si}}, \rho_{\mathrm{s}}) = \frac{\rho_{\mathrm{s}}^2 \cdot \tilde{T}_{\mathrm{P}}^{(3)}(\boldsymbol{\rho}, \eta; 0, \rho_{\mathrm{s}}) - \rho_{\mathrm{si}}^2 \cdot \tilde{T}_{\mathrm{P}}^{(3)}(\boldsymbol{\rho}, \eta; 0, \rho_{\mathrm{si}})}{\rho_{\mathrm{s}}^2 - \rho_{\mathrm{si}}^2} \tag{2.20}$$

where:

$$\tilde{T}_{\mathrm{P}}^{(3)}(\boldsymbol{\rho}; \eta, \rho_{\mathrm{si}}, \rho_{s}) = \frac{T_{P}^{(3)}(\boldsymbol{\rho}; \eta, \rho_{\mathrm{si}}, \rho_{s})}{B} \tag{2.21}$$

and

$$B = \pi(\rho_{\mathrm{s}}^2 - \rho_{\mathrm{si}}^2) \tag{2.22}$$

Equation (2.21) and Eq. (2.22) are the equations (8) and (9) in [82], and together with Eq. (2.20) and Eq. (2.15), the generalized nonparaxial 3D POTF for annular illumination can be calculated.

Similarly, Bao in [82] also calculates the WD-PCTF for annular case by a weighted difference of WD-PCTFs of disk illumination sources corresponding to the outer and inner radii of the annulus, as given by Eq. (11) in that paper, and repeated here:

$$T^{(2)}_{\mathrm{P_W}}(\boldsymbol{\rho};\rho_{\mathrm{si}},\rho_{\mathrm{s}}) = \frac{\rho_{\mathrm{s}}^2 \cdot T^{(2)}_{\mathrm{P_W}}(\boldsymbol{\rho};0,\rho_s) - \rho_{\mathrm{si}}^2 \cdot T^{(2)}_{\mathrm{P_W}}(\boldsymbol{\rho};0,\rho_{\mathrm{si}})}{\rho_{\mathrm{s}}^2 - \rho_{\mathrm{si}}^2} \tag{2.23}$$

With this set of expressions (Eq. (2.17) to Eq. (2.23)), the nonparaxial MFPI-PC can be implemented for the annular case, similar to the process shown in Fig. 2.2. However, Bao makes further improvement to the MFPI-PC method by arguing that for annular illumination case, in the transfer function inversion step of the procedure from Fig. 2.2, using the individual PCTFs ($T^{(2)}_{\mathrm{P},k}(\rho)$) corresponding to each order of SGDF is better than using the same WD-PCTF ($T^{(2)}_{\mathrm{P_W}}(\rho)$) over all orders of SGDF. This is because in disk illumination, the PCTFs are all positive and the higher order PCTF is always greater than the lower order PCTFs, whereas, in annular case, the PCTFs can also be negative and hence a lower order PCTF may have a higher absolute value than the WD-PCTF or the PCTF of higher order. This is especially true for some mid-range frequencies where WD-PCTFs and higher order PCTFs have small absolute values, and inverting over them can cause noise magnification. This is clearly observed in Fig.5 of [82] and it validates the argument to use the individual PCTFs of each SGDF order directly for transfer function inversion, instead of a common WD-PCTF for all SGDF orders.

The PCTF for (2*k*-1)th order of SGDF is given by $T^{(2)}_{\mathrm{P},k}(\rho)$ and can be calculated using Eq. (2.7) where the $H_{\mathrm{SG}}(e^{j2\pi\eta})$ term corresponds to $H_{\mathrm{SG},k}(e^{j2\pi\eta})$ and represents the frequency response of the (2*k*-1)th order of SGDF.

The phase information recovered from each order of SGDF is then combined together using least squares filtering, as now there is no need for any cutoff frequencies for selecting specific frequency range for each order of SGDF, calculated using the PTFs. Instead, phase from each SGDF order is weighted according to the square of the modulus of the PCTFs corresponding to that SGDF order. This is described in [82] as Least Squares MFPI-PC

(LS-MFPI-PC) and is represented by Eq. (15) and (16) in [82], as repeated below:

$$\phi(\boldsymbol{\rho}) = \sum_k H^{(k)}(\rho)\phi^{(k)}(\boldsymbol{\rho}) \tag{2.24}$$

where $H^{(k)}(\rho)$ is the weighting filter. For LS-MFPI-PC, the weighting filter is given by Eq. (16) in [82]:

$$H^{(k)}_{\mathrm{LS}}(\rho) = \frac{|T^{(2)}_{\mathrm{P},k}(\rho)|^2}{\sum_k |T^{(2)}_{\mathrm{P},k}(\rho)|^2 + \alpha} \tag{2.25}$$

where α is a regularization parameter from Wiener filtering, used to avoid division with a very small denominator.

Bao made further modification to the LS-MFPI-PC by incorporating the fact that a lower order SGDF has a better noise performance than a higher order SGDF. This fact is used by giving a higher weight to lower order SGDFs and a smaller weight to higher SGDF orders. This is done by modifying the weighting filter by $1/\sum_i |a^{(k)}_i|^2$ where $a^{(k)}_i$ is the impulse response of (2*k*-1)th order of SGDF. The new weighting filter with this modification is given by Eq. 17) in [82]:

$$H^{(k)}_{\mathrm{WLS}}(\rho) = \frac{|T^{(2)}_{\mathrm{P},k}(\rho)|^2 / \sum_i |a^{(k)}_i|^2}{\sum_k [|T_{\mathrm{P},k}{}^{(2)}(\rho)|^2 / \sum_i |a^{(k)}_i|^2] + \alpha} \tag{2.26}$$

This method is called the Weighted Least Squares MFPI-PC (WLS-MFPI-PC) [82].

Figure 2.4 shows the phase imaging process for LS-MFPI-PC and WLS-MFPI-PC. The WD-PCTF from Fig. 2.2 is replaced with individual PCTFs for every order of SGDF. The filter $H^{(k)}(\rho)$ in the last step is given by $H^{(k)}_{\mathrm{LS}}(\rho)$ for LS-MFPI-PC and $H^{(k)}_{\mathrm{WLS}}(\rho)$ for WLS-MFPI-PC, and is the distinguishing factor between the two methods.

The methods discussed in this chapter i.e. paraxial MFPI-PC, nonparaxial MFPI-PC, and WLS-MFPI-PC with annular illumination have been used in this research to reconstruct phase images of custom-fabricated phase masks in order to validate the phase recovery performance of these methods experimentally. The known phase and spatial variation of

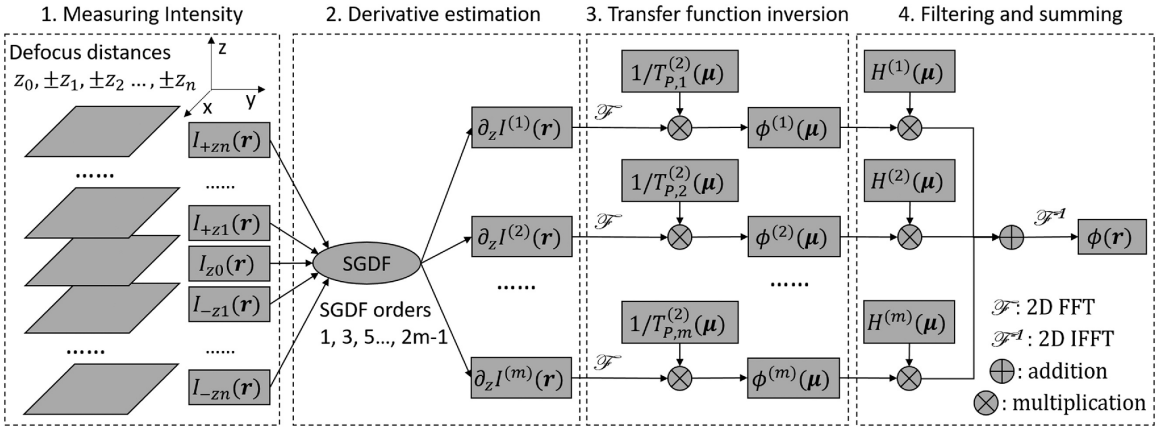

Figure 2.4: Flowchart of LS-MFPI-PC and WLS-MFPI-PC. The transfer function inversion is done using PCTFs for each SGDF order. The filter $H^{(k)}(\rho)$ can be given by $H^{(k)}_{\mathrm{LS}}(\rho)$ or $H^{(k)}_{\mathrm{WLS}}(\rho)$. (image from [82])

the phase masks allow for comparison of the known values with the values measured using the above-mentioned methods.

CHAPTER 3
DEVELOPMENT OF QPI INSTRUMENTATION

Defocus-based QPI methods require defocused intensity patterns as inputs to reconstruct a phase image of an object. A defocus-based QPI system should be designed to collect multiple defocused intensity patterns of the object repeatably and reliably. Such a system was developed at the Optics Laboratory and successfully used in various experiments [28, 48, 81, 82, 156]. However, the system was outdated and suffered from several limitations. The present chapter provides a detailed explanation of the working of the previous QPI system, its limitations, and the development of a new and improved QPI system with the latest hardware and software.

3.1 Previous QPI system

The previous QPI system at the Optics Laboratory was first assembled by Micah Jenkins [47] and later modified by Yijun Bao [59]. As described in Chpt. 2, the 2D QPI techniques developed at the Optics Laboratory are defocus-based and use partially coherent illumination. As a result, these QPI methods can be easily implemented on a standard microscope system without extensive modifications. The previous QPI system consists of an Olympus BX60 microscope, Physike Instrumente PI 721.SL2 piezoelectric objective scanner and E-709 Digital Pizeo controller, QImaging Retiga 1300R camera, Newport ESP300 Motion controller, Newport ESP100 motion controller, and Newport SR50PP motorized rotation stages. Figure 3.1 shows a schematic diagram of the previous QPI system and highlights its different components. Typical objects imaged using the system include optical fibers and biological cells.

Defocused intensity patterns can be collected either by keeping the microscope objective stationary and moving the sample out of focus, or by keeping the sample stationary

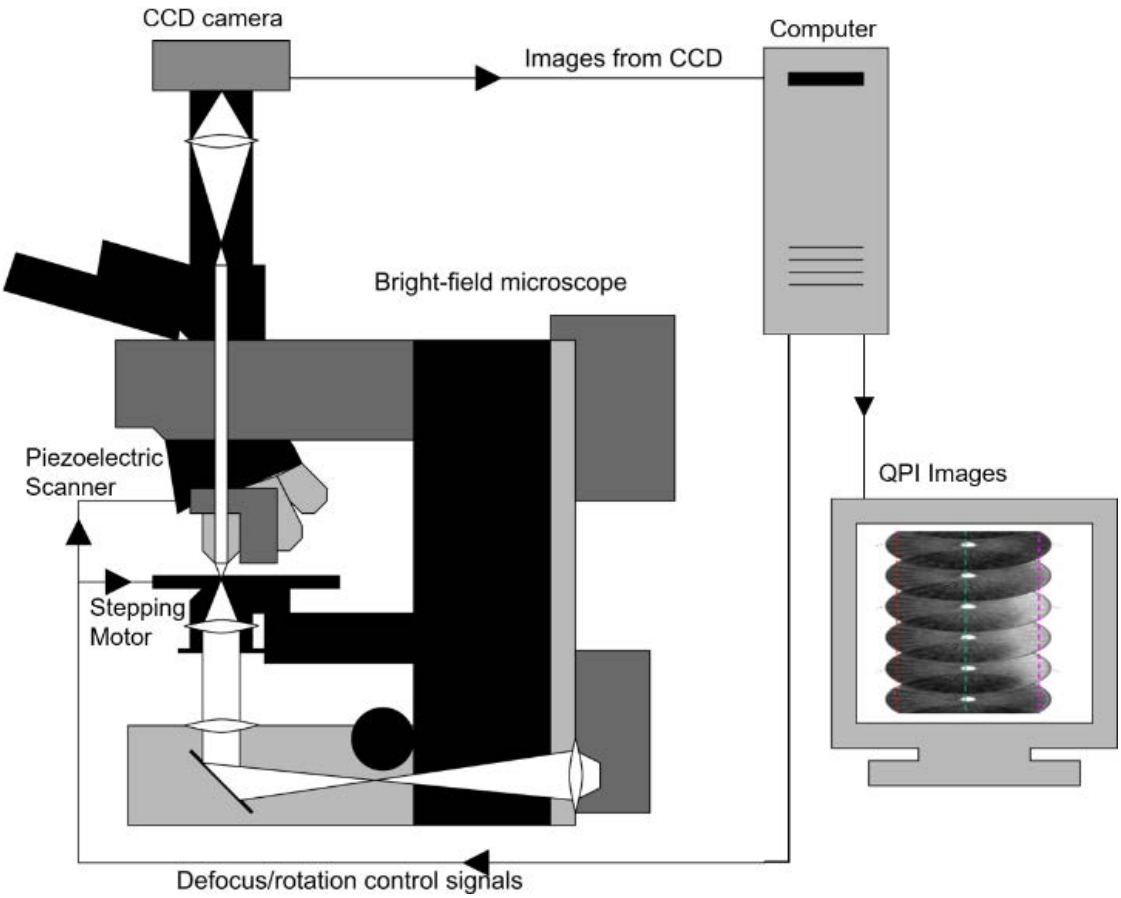

Figure 3.1: Schematic diagram of the previous QPI system in the Optics Laboratory (from [59])

and moving the microscope objective along the optical (vertical, z) axis of the microscope. Initially, in the previous QPI system, the defocused intensity patterns were collected by moving the sample (microscope stage) out of focus. This was done by rotating the microscope focus knobs using stepper motors. Stepper motors were used to have precise control over the motion of focus knobs and ensure the movement of the sample in desired steps. However, it was soon realized that this method did not provide sufficient precision in the motion of the objective and was prone to backlash error.

In order to overcome the limitations associated with moving the microscope stage precisely, and to minimize the complexity of the system, the system was modified to move the microscope objective utilizing a Piezoelectric Objective Scanner (POS). The system used the Physike Instrumente P-721.SL2 objective scanner. The microscope objective was

attached to the POS, which was controlled using the Physike Instrumente PI E-709 digital piezo controller. The scanner had a 5 nm resolution of motion, and hence provided flexibility in selecting appropriate defocus distances. The precise motion of the POS allowed better phase image results than those obtained with the stepper motor configuration.

Figure 3.2 shows the motion of the microscope objective controlled by the POS. When the sample is in crisp focus, the objective is positioned at the "in-focus plane" (reference plane) as shown in the figure. The POS then moves the objective downwards or upwards (depending on the algorithm) along the optical axis by a distance equal to the "defocus distance" as shown in the figure. The sample becomes out of focus, and the objective is positioned at a "defocus plane." A camera records the intensity pattern whenever the objective is positioned at a defocus plane. In the 2D QPI experiments performed at the Optics Laboratory, the objective was moved to 15 consecutive defocus planes above and below the in-focus plane. The intensity pattern of the sample was recorded at every step. Consequently, a total of 31 intensity patterns were collected for every 2D sample (15 defocus planes on either side of the in-focus plane, and when the objective is at the in-focus plane). Together, the 31 intensity patterns constitute one stack of intensity patterns.

The MFPI-PC method (2D QPI) requires only one stack of defocused intensity patterns. However, the TDPM method (3D QPI) uses tomographic reconstruction [50, 163]. Hence, to obtain sufficient information about the object to reconstruct its phase image using TDPM, the defocused intensity patterns need to be recorded from multiple angles. One way to achieve this is to keep the sample stationary and rotate the incident beam to illuminate the sample from multiple directions. However, in such beam configurations, it is typical that not all angles can be covered. Thus, there is a "missing cone" [164] in the spatial frequency domain which needs to be filled using *a priori* knowledge of the object [165]. However, it is not possible to have knowledge of the sample when imaging an unknown sample. A better alternative is to rotate the sample instead of the illumination beam.

Therefore, the previous QPI system was designed to rotate the optical fiber samples in

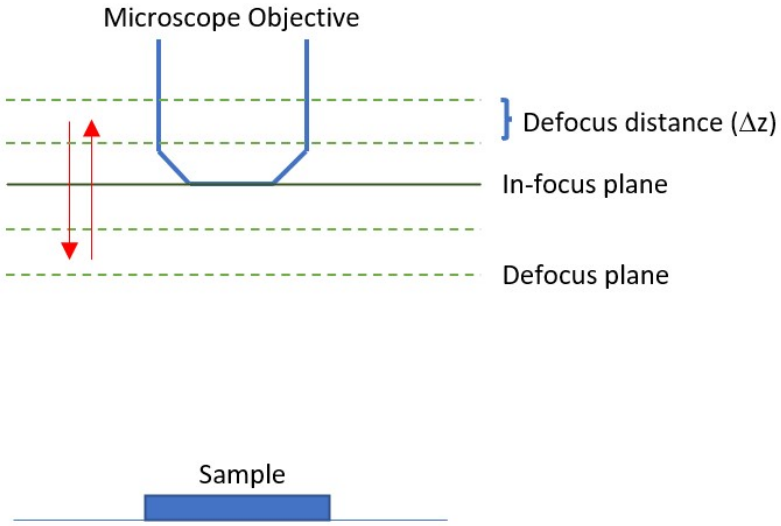

Figure 3.2: Schematic diagram showing the motion of the objective through multiple defocus planes. The objective is moved using the POS.

specific steps to cover the range from 0-180 degrees. The optical fiber was held in place using two fiber rotation chucks attached to the two rotation stages on both ends of the fiber. The rotation stages would operate in sync and rotate the entire fiber sample. This proved to be a reliable and repeatable way of rotating the sample, and hence it has been adopted in the new QPI system. At every angle of rotation, a new stack of defocused intensity patterns was recorded by the camera.

Although the previous QPI system was extensively used by Micah Jenkins and Yijun Bao for their research and many important results were obtained from its use, it had its drawbacks. The POS used in the previous system had a maximum range of $100\ \mu\mathrm{m}$, whereas the cladding diameter of a standard SMF-28 fiber is $125\ \mu\mathrm{m}$. Consequently, the information recorded in the multiple defocused intensity patterns was not sufficient to cover the entirety of the fiber sample. The small range of the POS was a major drawback as it limits the use of the system for fibers with a diameter larger than the scanning range of the POS. This problem was circumvented in the past with the use of index-matching oil,

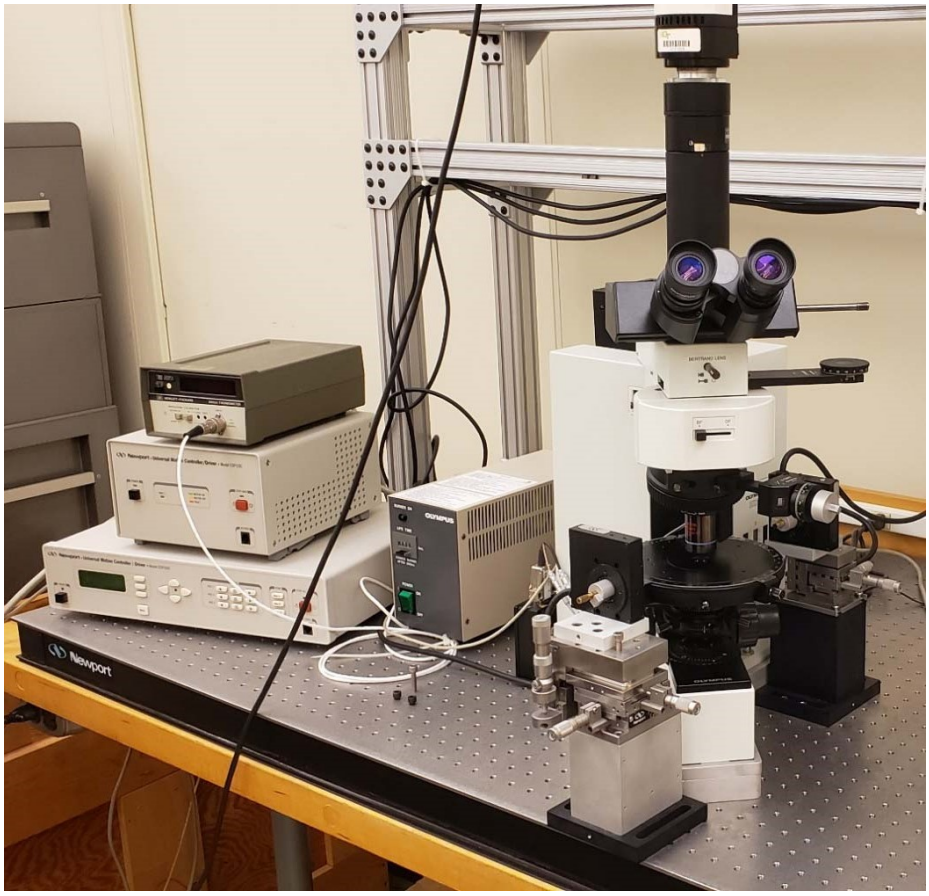

Figure 3.3: Photograph of the previous QPI system

which was also important to create a uniform refractive index matching medium around the fiber. The use of oil increased the RI of the medium which increased the effective range of the POS. When an index-matching oil with $n_{\text{oil}} = 1.46$ was used, the effective range of the POS became $1.46 \times 100\ \mu\text{m} = 146\ \mu\text{m}$. However, even with the increased effective range, the POS needed to travel its full range to record sufficient information in the stack of defocused intensity patterns. Therefore, the previous system was programmed to use the scanner over the full range for all fiber samples. Furthermore, at each angle of fiber rotation in TDPM, the stack of defocused intensity patterns contained hundreds of recordings. It led to a large amount of data transfer between the camera and the computer. The camera used in the previous system (QImaging Retiga 1300R) was connected to the computer using a "Firewire" connection, which was outdated. Upgrading the interface between the camera

and the computer would minimize the latency in the data acquisition process. Furthermore, developments in the camera technology could be adopted by incorporating a new camera for the system.

The main aim of developing the new QPI system was two-fold - to have another system based on the same principles as the previous system and to incorporate new hardware and improved software. An advantage of having a similar system is the ability to verify the results obtained on one system by repeating the experiment on the other system. It acts as an independent verification of the results. However, since the new system would have better hardware and wider capability, some results obtained on the new system will not be replicated on the previous system.

The following section describes the new QPI system with all its working components and the LabVIEW control program. The working principle of the new system is same as the previous system, except with better hardware and improvements in the operating program.

3.2 New QPI System

3.2.1 Experimental Configuration

The newly developed QPI system consists of an Olympus BX60 Microscope, a mercury arc lamp, Pixelink M5D-CYL Monochrome Camera, Physike Instrumente PI P-725.4CD piezoelectric objective scanner with a PI E-709 Digital Piezo controller, Newport ESP300 Motion controller, and Newport SR50PP motorized rotation stages. Figure 3.4 shows a schematic diagram of the new QPI system with its various components.

As shown in Fig. 3.4, the new QPI system does not require extensive changes to a standard Olympus BX60 microscope. The mercury arc lamp is widely used with the microscope. The use of an interference filter makes the wavelength quasi-monochromatic, which is necessary for QPI measurements. In both the previous and the new QPI system, an IF546 interference filter is used which allows only a narrow band of wavelengths around 546 nm to pass through the optical system. The sample is uniformly illuminated by the mercury arc

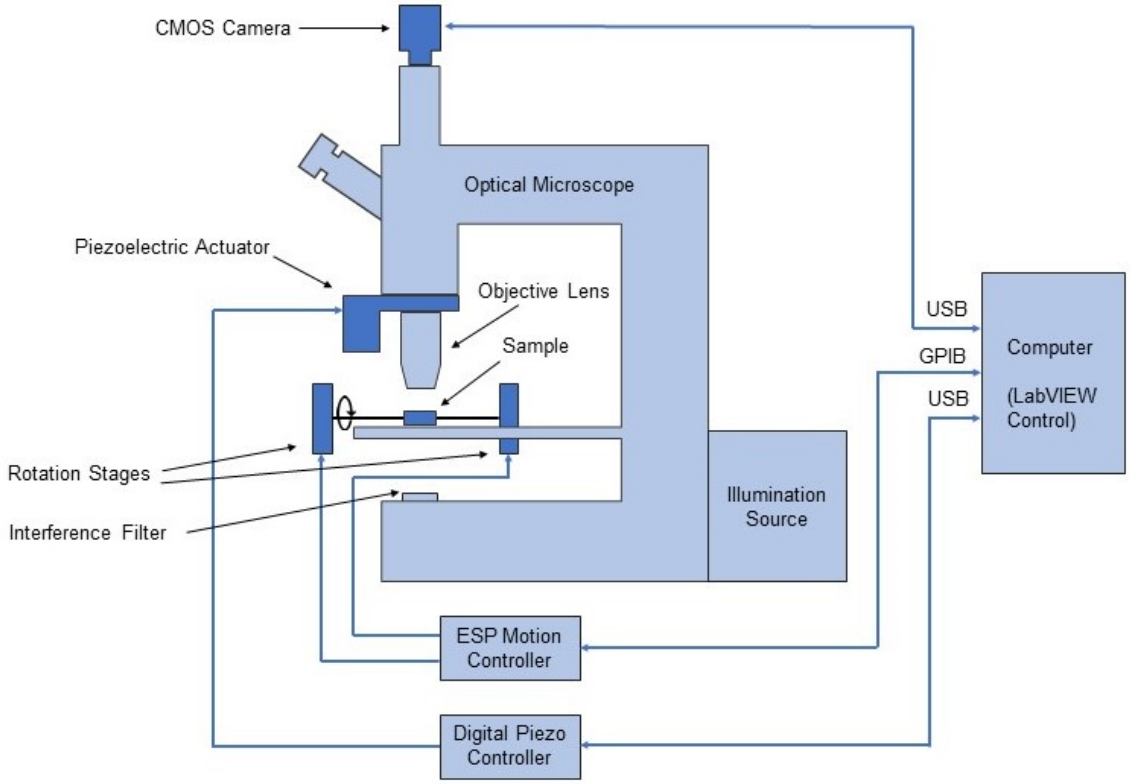

Figure 3.4: Schematic diagram of the new QPI system.

lamp which is an extended source (not a point source). Therefore, it acts as a good source of partially coherent illumination. The QPI theories developed by Jenkins and Bao make use of partially coherent illumination to determine the POTFs associated with the sample [48, 82]. The POS is attached to the turret of the microscope, and the objective lens is attached to it. It is shown as "Piezoelectric actuator" in Fig. 3.4. The POS moves the objective lens through multiple defocus planes along the optical axis, and allows the camera to record the defocused intensity patterns. It is controlled using the PI E-709 Digital Piezo Controller that communicates with the computer via a USB interface and operates the POS according to the LabVIEW program. The POS in the new system has a full scanning range of $400\ \mu\mathrm{m}$ which is four times that of the POS in the previous system. This allows QPI imaging of thicker objects that wouldn't be possible on the previous system. Furthermore, the new POS has a 1.5 nm resolution in motion as compared to that of 5 nm of the POS in the previous system. This allows for more precise control and smaller defocus distances if

required. Longer range of the POS also allows the objective to be positioned at the defocus planes that are farther from the in-focus plane. A larger number of defocused intensity patterns improves intensity derivative estimation [160] albeit at the expense of more processing time. However, with the ability to record a larger number of defocused intensity patterns, the user can reconstruct a more accurate phase image if desired. Description of various system components is given below.

Fig. 3.4 shows the position of the two Newport SR50PP rotation stages that hold and rotate the fiber. The two rotation stages are micro-step-drive stepper motors and are controlled by the Newport ESP300 motion controller. The rotation stages and the motion controller in the new system are the same as in the previous QPI system. The rotation stages have a resolution of 0.004° and an accuracy of $\pm 0.02^\circ$. Typically, the fiber rotation increment angle is set to either 9° or 12°. The motion controller is connected to the computer via a GPIB interface.

The camera is situated at the top of the microscope and is an important part of the system. Unlike the CCD camera in the previous QPI system, the new system has a CMOS camera that has better performance. Furthermore, the image resolution of the new camera is 5.01 megapixels as opposed to 1.3 megapixels of the camera in the previous QPI system. The new camera is connected to the computer via a USB 3.0 interface resulting in much faster data transfer than the IEEE 1394 (Firewire) interface in the previous system. The data transfer speed is important due to the large number of intensity patterns that are recorded in one experiment. This is a step towards making the system function in "real-time".

Lastly, the workstation computer connected to the new system has Intel Core i7 8th generation processor and 32 GB RAM, as compared to the Intel Core 2 Duo processor and 1.96 GB RAM in the previous QPI system. LabVIEW 2019 software package is used in the new system to communicate with all the components and operate them in a particular sequence. The previous system uses LabVIEW 2012 which is outdated. The new system uses IMAQ-dx LabVIEW drivers for controlling the camera operation. These drivers from

National Instruments were developed specifically for image acquisition purposes. If the camera device uses a USB 3.0 interface to communicate with the computer, then National Instruments requires that the camera be compatible with the USB3 Vision standard. The camera used in the new system also follows the USB3 Vision standard. Since many companies are adopting this interface standard for their USB devices, a new camera device from a different manufacturer could be used in the new system without making major changes to the LabVIEW program. It generalizes the use of the program and provides flexibility in choice of the camera. The new camera must also be compatible with the USB3 Vision standard. In the previous system, the data acquisition was programmed using custom LabVIEW drivers for the camera, making the program dependent on the particular camera model and manufacturer. Using a different camera in the previous QPI system would require major changes to the LabVIEW control program.

Table 3.1 shows the similarities and differences between the previous and the new QPI system. Important specifications of various components in the two systems are delineated.

In Fig. 3.5 the photograph of the newly developed QPI system is shown with its various components. In Fig. 3.6 the experimental configuration to image an optical fiber sample is shown. The middle portion of the fiber is carefully placed on a slide, and index-matching oil is used to create a uniform index-matching medium around the fiber. Two cover slips are placed on each side of the fiber as spacers and a third cover slip is placed on top to cover the fiber sample. The user must align the rotation stages with the microscope stage before the intensity patterns are recorded. The objective lens is attached to the POS and is moved along the optical axis according to the LabVIEW program. After a stack of intensity patterns is collected, the fiber is rotated by the "fiber rotation increment angle," for the next stack of intensity patterns. This process is repeated till the angle of rotation exceeds 180 degrees.

Since the 2D QPI method (MFPI-PC) does not require intensity patterns recorded from multiple angles, there is no use of rotation stages and the motion controller. Therefore,

Table 3.1: Table showing the similarities and differences between the previous Optics Laboratory QPI system and the new QPI system.

Component	**Attribute**	**Previous QPI system**	**New QPI system**
Microscope	Model	Olympus BX60	Olympus BX60
Piezoelectric Objective Scanner	Model	PI P-721.SL2	PI P-725.4CD
	Full Scanning Range (vertical axis)	100 μm	400 μm
	Scanning Resolution (vertical axis)	5 nm	1.5 nm
	Digital Piezo controller	PI E-709	PI E-709
Camera	Model	QImaging Retiga 1300R	Pixelink M5DM-CYL
	Type	Monochrome	Monochrome
	Image Resolution	1.3 MP	5 MP
	Interface	IEEE 1394 (Firewire)	USB 3.0
	Pixel size	7.4 μm	3.45 μm
	Bit depth	12-bit	12-bit
	LabVIEW Drivers	Custom drivers	NI IMAQ-dx package (USB3 Vision standard)
Motion Controller	Model	Newport ESP300	Newport ESP300
	No. of Axes	3	3
	Interface	GPIB	GPIB
Rotation Stages	Model	Newport SR50PP	Newport SR50PP
	Motor Type	Micro step drive stepper	Micro step drive stepper
	Angular resolution	0.004°	0.004°
	Typical Accuracy	±0.02°	±20°
Control Software	Name	LabVIEW 2012	LabVIEW 2019
	Support	custom device drivers	Exclusive image acquisition package IMAQ-dx.
	Program	Camera device specific	Generalized program
Workstation	Processor	Intel Core 2 Duo	Intel Core i7 8th Gen
	RAM	1.96 GB	32 GB

the fiber configuration shown in Fig. 3.4 does not involve rotation in case of MFPI-PC. As explained further in the chapter, there are two separate LabVIEW programs for MFPI-PC and TDPM that decide if the rotation stages are moved.

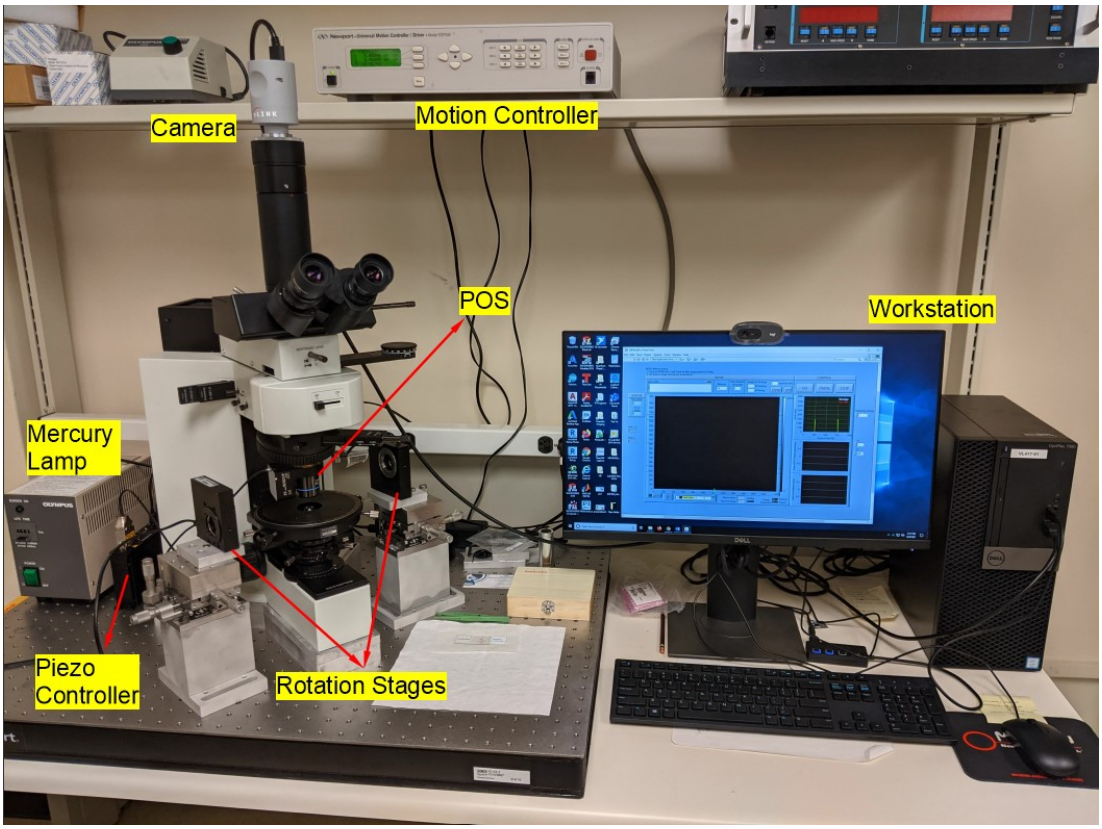

Figure 3.5: Photograph of the new QPI system

3.2.2 LabVIEW Program

LabVIEW 2019 software acts as an interface between the system and the user via its "front panel". It enables the user to monitor the various aspects of the data acquisition process. A LabVIEW program is called a "VI" and has a ".vi" filename extension. There are two programs that have been developed for the new system namely "MFPIPC_QPI.vi" and "TDPM_QPI.vi" for the MFPI-PC and TDPM methods respectively. The detailed working of the two programs is described in this section.

TDPM LabVIEW program

The program execution in LabVIEW is not serial. That is, the program is built using a block diagram interface where the sequence of operations is determined using the "data flow" in the diagram. Every LabVIEW VI has two windows - the front panel, and the

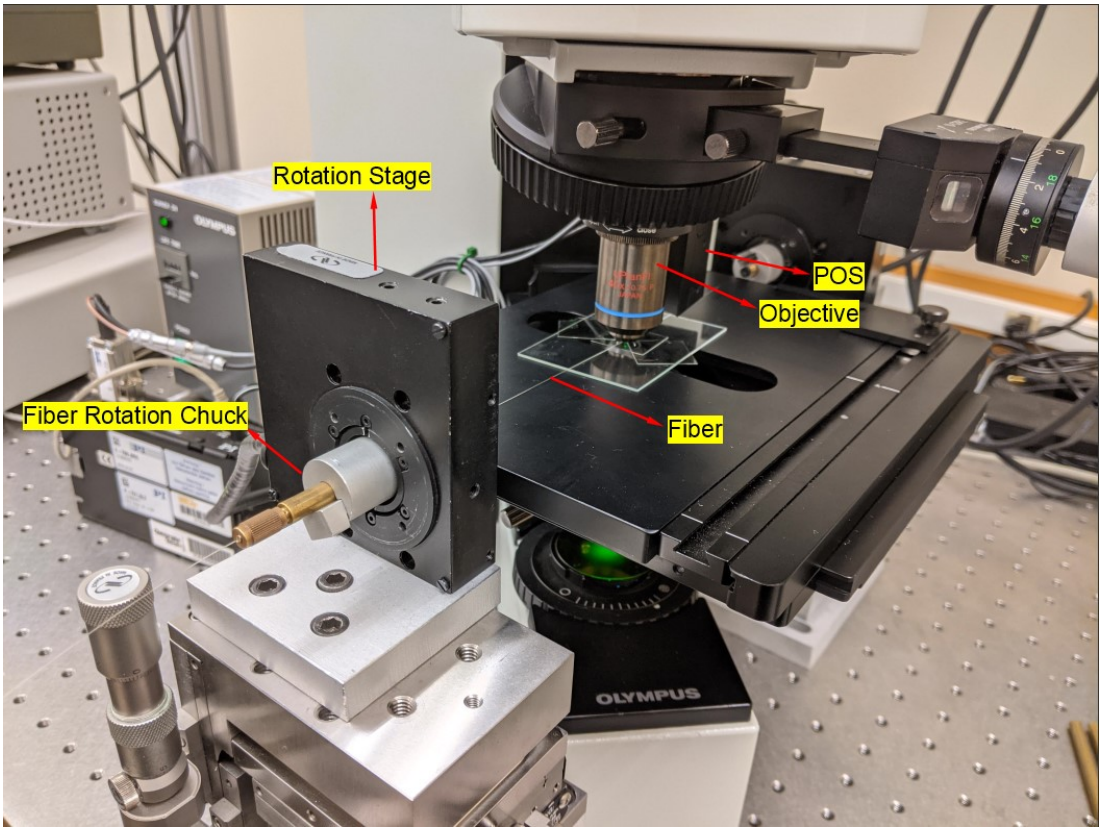

Figure 3.6: Experimental configuration to image a fiber sample. The fiber is held in two fiber-rotation chucks attached to the two rotation stages.

block diagram. The front panel window is an interface between the user and the system whereas the block diagram controls the logic of operations. The front panel is used to get input from the user, as well as to show the current values of parameters. Figure 3.7 shows an example LabVIEW program to take the temperature input from the user in Fahrenheit and convert it into Celsius. Figure 3.7a shows the front panel interface of the LabVIEW program containing all the indicators and input entries. The block diagram window in Fig. 3.7b shows the logic of operations associated with the different entries and indicators on the front panel.

LabVIEW has several case structures and loop structures that are useful in developing the logic of operations. Figure 3.8 shows the various structures and VI blocks used in the TDPM LabVIEW program. These are explained below:

1. A Stacked Sequence Structure (SSS) is used to perform operations in a specific order.

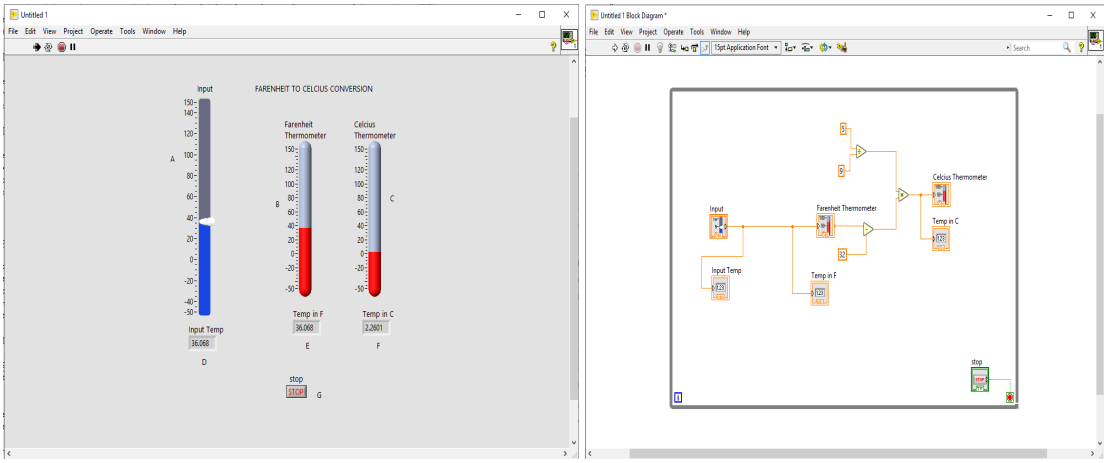

(a) LabVIEW front panel interface. (b) The block diagram window.

Figure 3.7: The front panel and block diagram of an example LabVIEW program to convert the temperature in Fahrenheit to Celsius.

It has a series of frames containing various operations. The execution is performed frame by frame, i.e., operations in Frame 1 are not executed until operations in Frame 0 are complete, and so on. The frame number is visible on the top of this structure, and the frames can be switched using arrow buttons on both sides.

2. While loop. All the operations contained in this structure will keep running until the "stop condition" is satisfied. The stop condition is programmed to the "red button" on the bottom right of the structure.

3. For loop. The "N" on the top left corner of this structure shows the total loop count. The operations defined in this structure will be executed only N number of times. The loop will terminate automatically after N runs.

4. True/False case structure. The green square on the left edge of this structure is a Boolean condition. If this condition is True, then operations contained in the "True" (visible on the top edge of the structure) case will be executed. Similarly, if the condition is false, operations contained in "False" will be executed.

5. Camera Open VI. This VI is a part of the LabVIEW IMAQ-dx package and is used

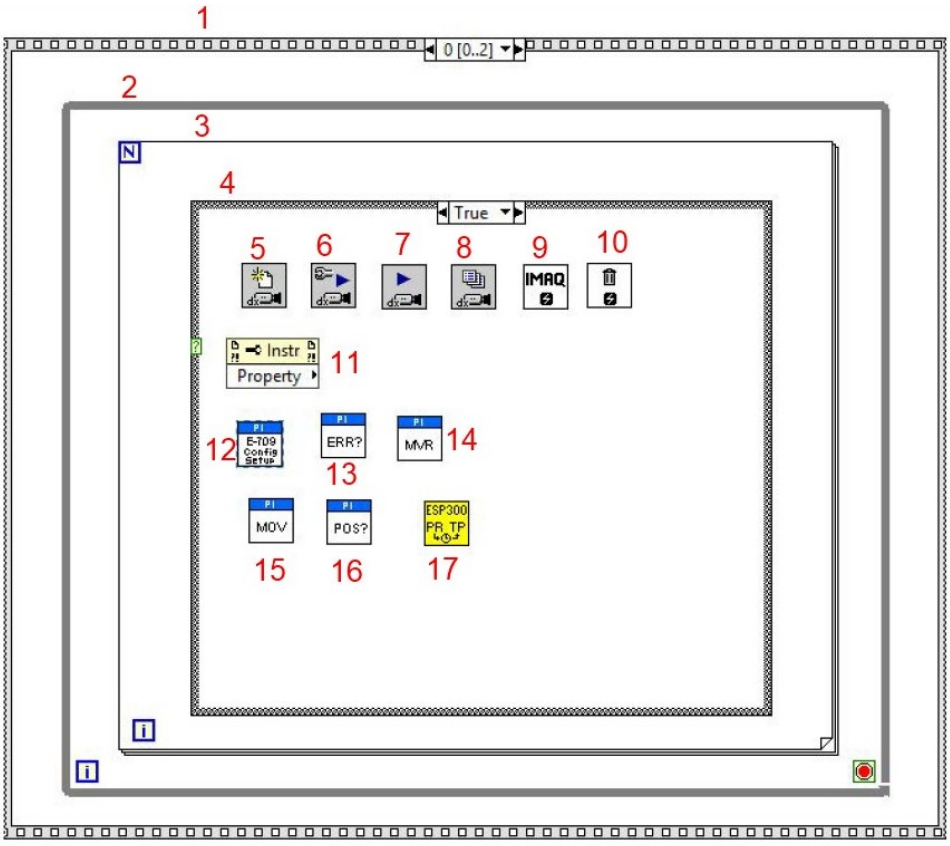

Figure 3.8: Items 1-4 are the various case structures and loop structures in LabVIEW. Items 5-11 are VIs that are a part of the NI IMAQ-dx and Vision Utilities packages. Items 12-16 are VIs used to control the PI piezoelectric scanner, and item 17 is the VI used to control the Newport motion controller.

to access the camera for use.

6. Configure Grab VI. This VI is also a part of LabVIEW IMAQ-dx. It is used to configure the camera for grabbing (capturing) an image as an operation in the program.

7. Grab VI. This block is used to capture an image through the camera. This block is wired to the Configure Grab VI and the IMAQ create VI for capturing and storing the image.

8. Enumerate Attributes. It is a VI from the IMAQ-dx package which helps to enumerate the various configuration parameters (like exposure, gain etc.) of the camera. These parameters can be accessed and changed according to the application.

9. IMAQ Create. This VI creates a temporary memory location to store an image.

10. IMAQ Dispose. This VI destroys the captured image and is used to free up the memory reserved via IMAQ create.

11. Property node. It is a LabVIEW block that allows the programmer to access or alter the values of a specific attribute of a connected device. Eg. Using the property node, the exposure time attribute is changed in the TDPM VI.

12. E-709 Config setup. This VI is responsible for initialization of the Digital Piezo controller and the POS. This VI must be present in every VI that uses the E-709 controller, and must be executed before performing any operation with the controller.

13. "ERR?". This VI acts as an error query and notifies if there is an error in the operation of the E-709 controller.

14. MVR. This VI allows the POS to be moved relative to the current position of the POS by a specific distance in microns.

15. MOV. This VI is similar to MVR, except it allows the POS to be moved to an absolute position instead of a relative position. The absolute position of the POS is zero at the highest point and 400 at the lowermost point. Setting the POS to position 200 brings the POS halfway down.

16. "POS?". This VI acts as a query to obtain the current position of the Piezoelectric Objective Scanner (POS). The current position is useful in determining the motion of the POS in the next operation.

17. This VI block is used to control the Newport motion controller and rotate the Newport SR50PP rotation stages by a specific angle increment.

The front panel of the TDPM LabVIEW program is shown in Fig. 3.9 . The different parts of the front panel are numbered in the image and are explained as follows:

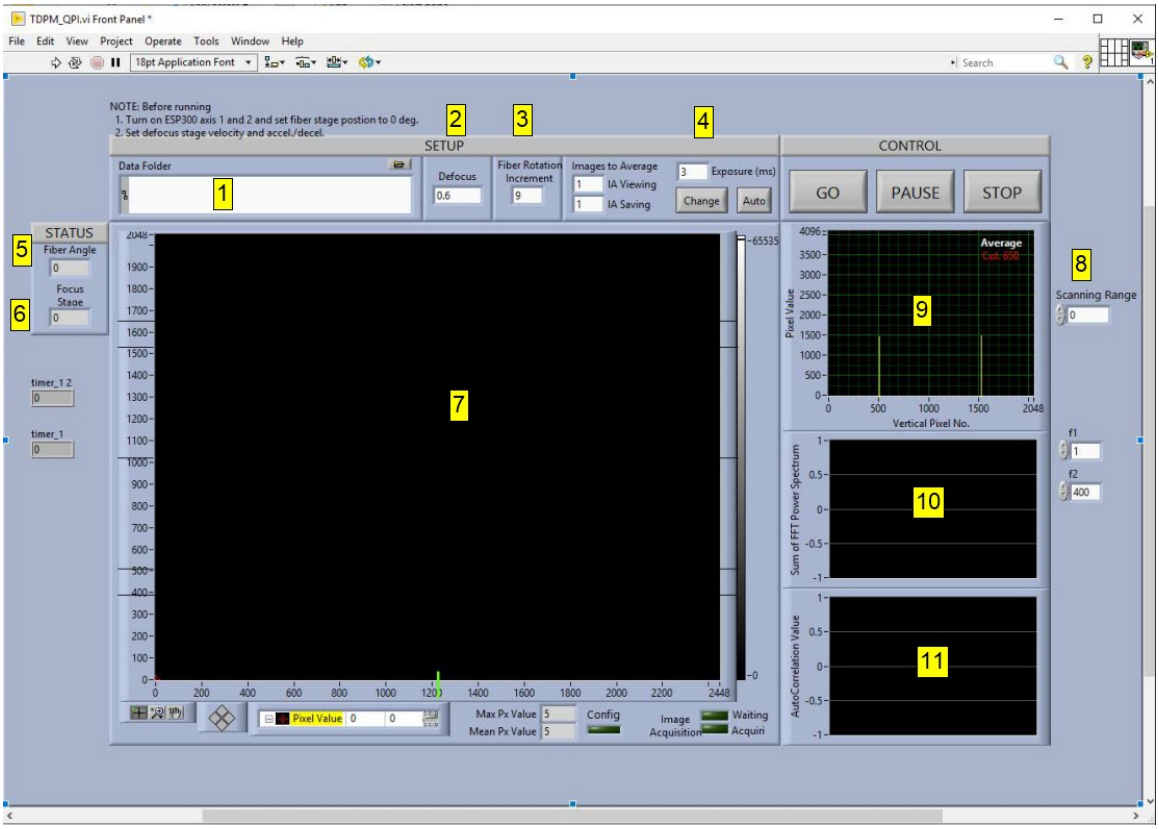

Figure 3.9: Front Panel of the TDPM LabVIEW program.

1. Destination Folder address entry. The user must press the "folder icon" on the top right of this entry to browse to the folder in which the recorded intensity patterns will be saved. Once the folder is selected, the entry will be auto-filled with the path to the destination folder.

2. Defocus Distance. This is the distance (in microns) between two defocus planes along the optical axis of the microscope. This is the step size in increment or decrement in the position of the POS (refer to Fig. 3.2). In the block diagram, this entry is linked to the VIs that are responsible for moving the POS.

3. Fiber Rotation Increment angle (degrees). This entry provides the step size angle for rotation of the fiber via the rotation stages.

4. Exposure time (ms). This entry allows the user to change the camera exposure set-

tings. The “Change” button applies the value in the entry box and the “Auto” button implements the “Auto exposure” to set the exposure time automatically.

5. Fiber Angle indicator. This indicator on the left of the panel shows the current position of the rotation stages. Since both the stages rotate in sync, this value indicates the position of both the rotation stages. The value stays constant while the stack of intensity patterns is recorded at a particular angle. The value is updated when the stages rotate to a new position.

6. Focus stage position indicator. This indicator shows the current position of the POS relative to the focal plane, i.e., the value at the focal plane is 0, the values for planes below the focal plane are positive, and the values above the focal plane are negative. For the POS, a positive increment in its position corresponds to the POS moving down by the specified value.

7. Pixel value map. It is the space on the front panel that displays the data from the camera. When the program is run, the pixel map shows the live feed from the camera until the “GO” button is pressed. The live feed is paused while the intensity patterns are recorded and saved. The dimensions of the intensity patterns captured using the new Pixelink camera are 2448x2048 pixels.

8. Scanning Range (microns). This entry on the right of the panel defines the total scanning range of the POS. This range is the total distance the POS covers in moving from the topmost point to the bottom-most point on the optical axis. The POS in the new system has a maximum range of 400 microns. If the user needs the POS to move like in the previous system, then the value “100” must be entered here, as the maximum range of the POS in the previous system was 100 microns.

9. Pixel graph. This plot shows the variation of the pixel value over all rows for column 1224 (middle column).

10. Sum of FFT power spectrum. This plot calculates and displays the sum of the FFT power spectrum of the image array (after all the columns are averaged).

11. Auto-correlation plot. This plot displays the auto-correlation value for the image array (after all the columns are averaged).

The block diagram of the TDPM LabVIEW program uses three nested stacked sequence structures (SSS), each containing multiple frames. Some VIs like the IMAQ Create VI, Camera Open VI, and the Configure Grab VI, are programmed out of the scope of SSS. Fig. 3.10 shows the schematic diagram highlighting the order of execution of the various frames in the SSS. SSS1 is the outermost SSS while SSS3 is the innermost SSS among the nested SSS. In Fig. 3.11 and Fig. 3.12, the operations performed in each frame of the three SSS are shown. The detailed execution is explained further.

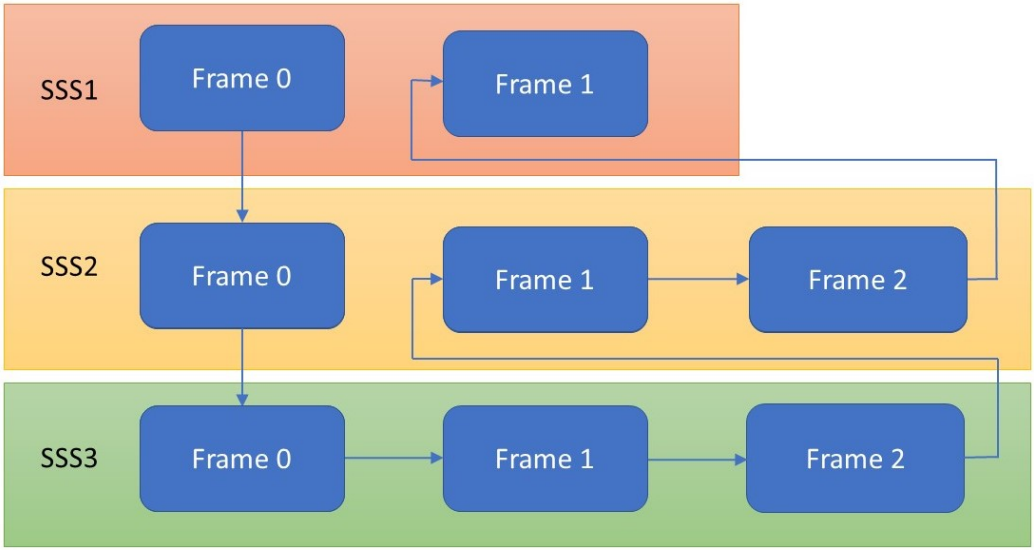

Figure 3.10: Order of execution of the various frames in the three stacked sequence structures.

The outermost structure (SSS1) contains two frames - Frame 0 and Frame 1. Frame 0 in SSS1 is responsible for the initialization of POS and setting the auto exposure for the camera. In Fig. 3.13, Frame 0 of SSS1 is shown. It contains two frame structures - one for setting the exposure (top) and the other (bottom) for initializing the POS and

Figure 3.11: Summary of operations performed by each frame in SSS1 and SSS2.

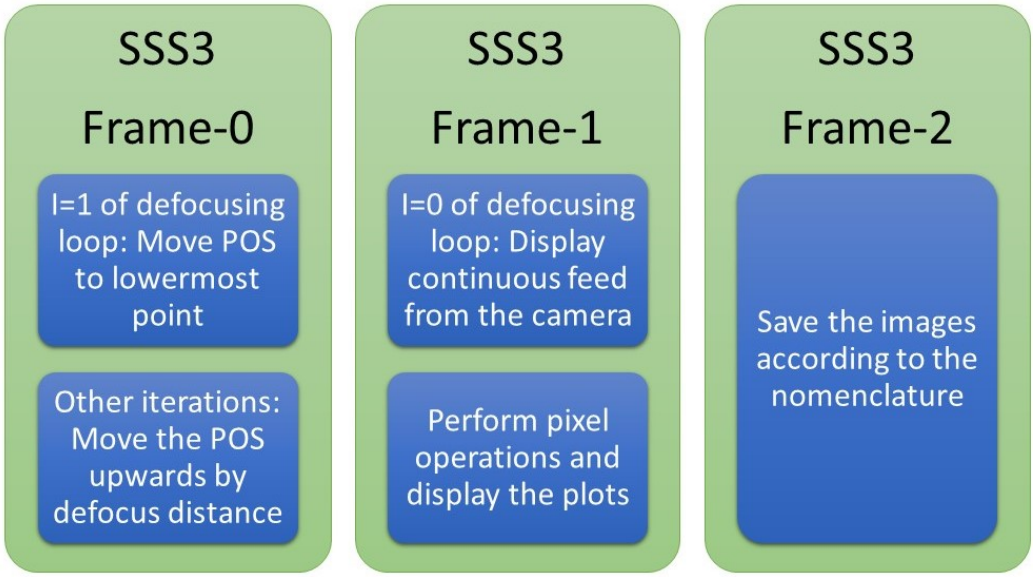

Figure 3.12: Summary of operations performed by each frame in SSS3.

bringing it to the middle position (position 200). The top frame structure performs the following series of operations. First, the auto exposure of the camera as set as the "active attribute" (using property node) and the camera is calibrated for auto exposure. Second, the program undergoes a delay of 2 seconds. Third, the new value of the camera exposure time is updated in the entry on the front panel.Lastly, the auto exposure is set to "off". This enables the user to adjust the exposure settings manually if required. The three frames in the bottom frame structure are executed at the same time as the top frame structure. The bottom structure performs following operations. First, the E-709 Config setup VI is

executed for initializing the POS and the POS is brought to the middle position (position 200). The "Config" light at the bottom of the front panel remains lit until the E-709 is initialization process is completed. Second, the program pauses for 1sec. to allow the POS to stabilize. Third, the "POS?" VI is used to obtain the current position of the POS and this value is displayed at the "Focus Stage Position" indicator as the "0" position. Frame 1 in SSS1 contains the two other nested SSS with rest of the operations of the program.

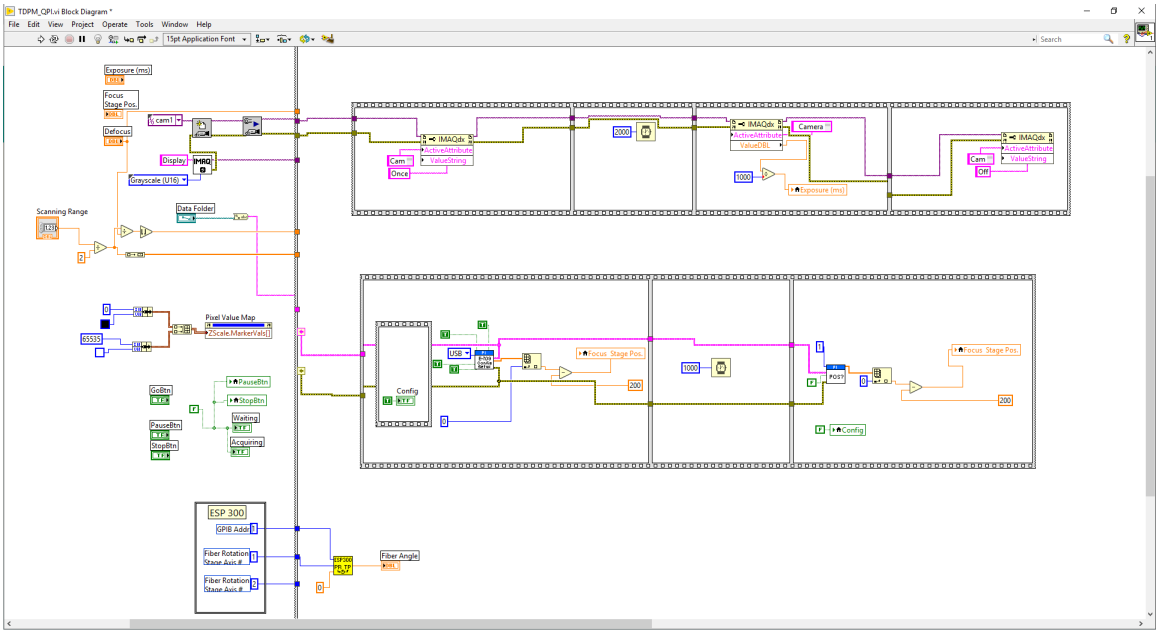

Figure 3.13: Frame 0 of the SSS1. Operations in this frame initialize the POS and implement the auto exposure.

Frame 1 of SSS1 contains a "while loop" named "Fiber Rotation Loop" (yellow in Fig. 3.14), which contains the next stacked sequence structure SSS2. Frame 0 of SSS2 contains a "for loop" named as the "Defocusing loop" (green in Fig. 3.14), which further contains the third stacked sequence structure SSS3. Every iteration of the "Fiber rotation loop" performs all the operations responsible for the data acquisition, POS movement, and saving the recorded intensity patterns, at a particular angle of rotation stages, after which, the stages are rotated to the next angle.

SSS2 contains three frames. Frame 0 contains the defocusing loop which contains the operations to record and save the intensity patterns for a particular POS position. In the next

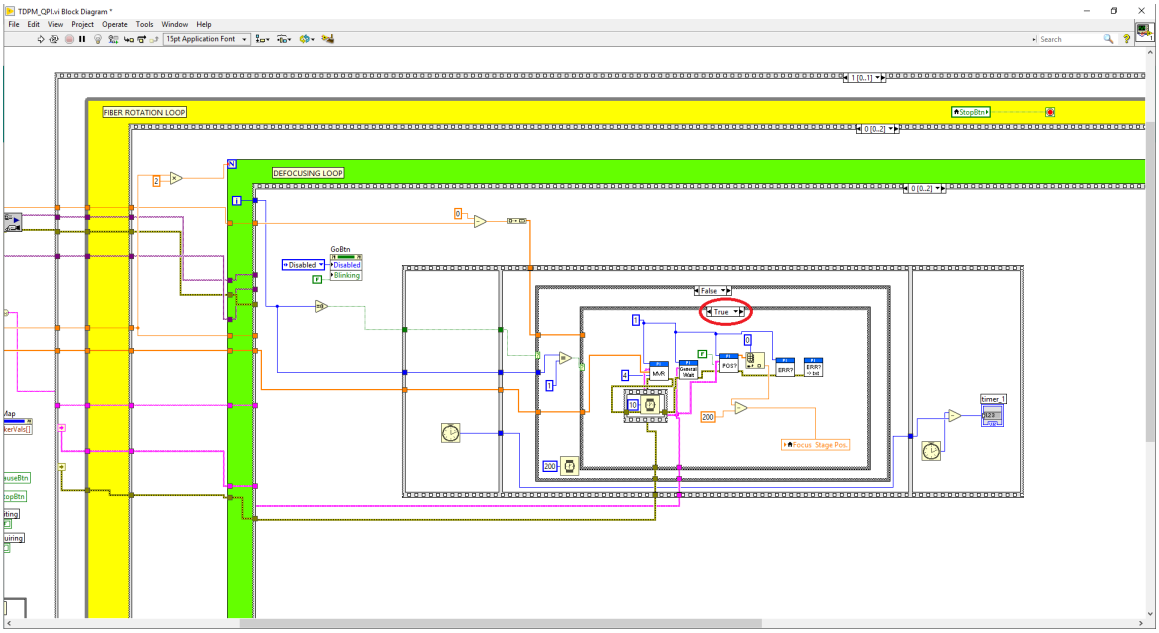

Figure 3.14: Fiber rotation loop (yellow) and the defocusing loop (green). The red circle highlights the deciding True/False condition for Frame 0 of SSS3.

iteration, the POS is moved again. The entire SSS3 is contained within the "Defocusing loop" which is a "for loop" with the total number of iterations given by the total number of intensity patterns to be recorded. The total number of intensity patterns to be recorded is given by the operation:

$$N = \text{floor}(Z/\Delta z) \tag{3.1}$$

where N is the total number of intensity patterns, Z is the scanning range in microns, and Δz is the defocus distance in microns. In Fig. 3.14, the highlighted red circle shows the True/False condition in Frame 0 of SSS3 that decides the way POS should move. When the loop count (I) of the defocusing loop is 1, the condition is True, and the POS is moved to the lowermost point of the scanning range. Otherwise, the condition is false and the POS is moved upwards by a distance equal to the defocus distance. As shown in Fig. 3.14, MVR block is used to perform this operation.

Frame 1 of SSS3 contains the operations to display continuous feed from the camera

to the pixel map in the front panel. The initial loop count of any "for loop" in LabVIEW is zero. When the loop count (I) of the defocusing loop is zero, Frame 0 does not perform any operations, and the execution is transferred to Frame 1. In this frame, the intensity pattern is recorded (using "Grab" VI), converted into an array, and processed to obtain the plots and values required on the front panel (blue region in Fig. 3.15). There is a provision to change the exposure time of the camera from the front panel, by either changing the value in the entry or by pressing the "Auto" button. The exposure change works the same way as described before in the section. The blue region in Fig. 3.15 contains the "image grab" operation, array operations, and the exposure change operation. The intensity pattern is recorded and then converted into an array. "Max" and "Mean" values of this array are calculated and displayed on the bottom of the front panel in their respective entries. Simultaneously, this array is also displayed on a pixel map visible on the front panel. Column 1224 from the image array is separated, and its values are plotted on the pixel graph (No. 9 in Fig. 3.9). All the columns from the array are then averaged, and the FFT spectrum block, along with the summation block is used to obtain the sum power FFT spectrum of the image. Similarly, Auto-correlation values are obtained and plotted on the front panel. These operations are the same as in the previous QPI system. These operations are a part of the "while loop" that continues to operate until the user either presses the "GO" button or the "STOP" button.

When the user presses the "GO" button, the "while loop" in Frame 1 of SSS3 is terminated and the execution moves to the next frame. As mentioned before, Frame 1 of SSS3 only performs its operations when the loop count (I) of the defocusing loop is 0. For all other loop counts, the "GO" button has already been pressed and the execution is first passed to Frame 0 and then to Frame 2. Frame 1 moves the POS, and Frame 2 commands the camera to record the intensity pattern, names it according to the decided nomenclature, and saves the image to the destination folder. Frame 2 of SSS3 is shown in Fig. 3.16.

After all the intensity patterns in one stack are recorded, the defocusing loop is termi-

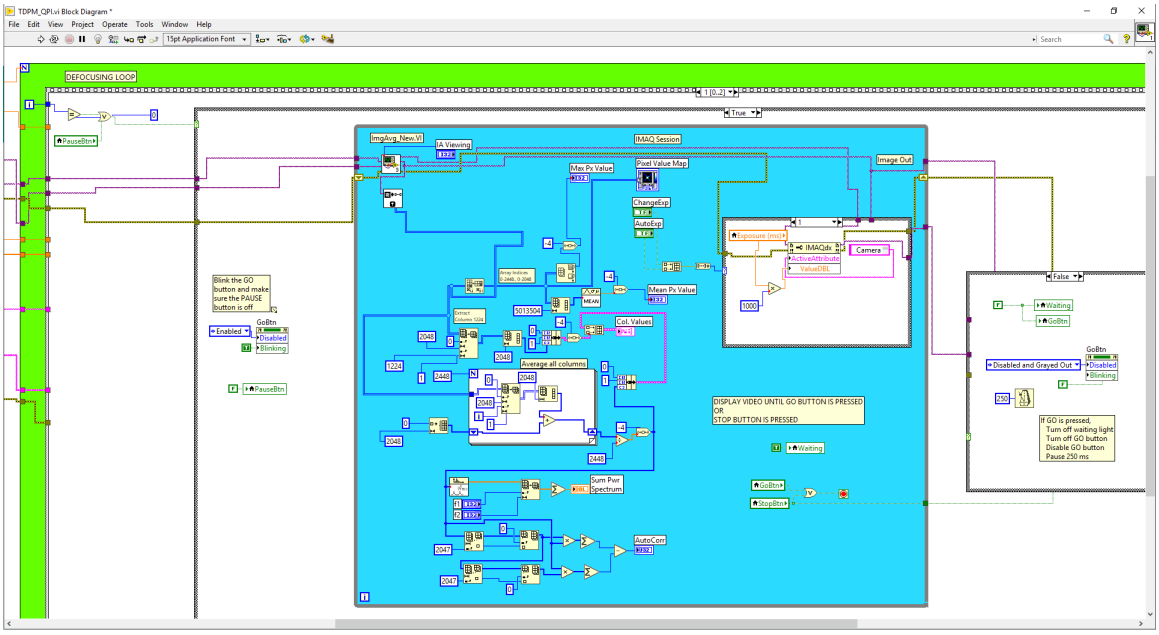

Figure 3.15: Frame-1 of SSS3. This frame contains all the operations for displaying the continuous feed from the camera before the user presses the "GO" button to start the image capture process.

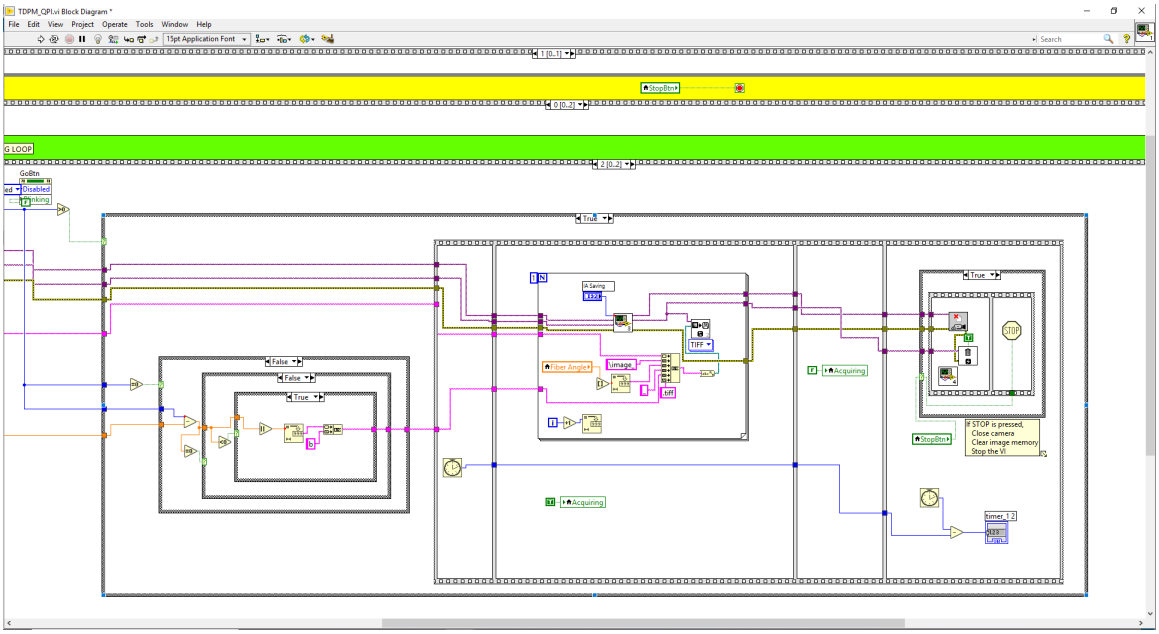

Figure 3.16: Frame 2 of SSS3. This frame performs operations of recording the intensity pattern and saving it to the destination folder with an appropriate name.

nated and the execution is transferred to Frame 1 of SSS2 (next step of the fiber rotation loop). This frame is shown in Fig. 3.17. The operations in this frame brings back the POS

to the middle “in-focus” plane to get it ready for the next iteration of the defocus loop (next stack of intensity patterns). The execution then shifts to Frame 2 of SSS2 which commands the ESP300 motion controller to rotate the rotation stages by the specified increment angle. This command to ESP300 motion controller is given using the ESP300_PR_TP.VI (No. 17 in Fig. 3.8). The operation mentioned above is shown in Fig. 3.18. After the rotation is performed, the system is ready to record the next stack of intensity patterns. The program does not begin the data acquisition process for the next stack until the user presses the “GO” button again. Such a feature helps the user to re-center and re-align the fiber (if required) before the next stack is recorded.

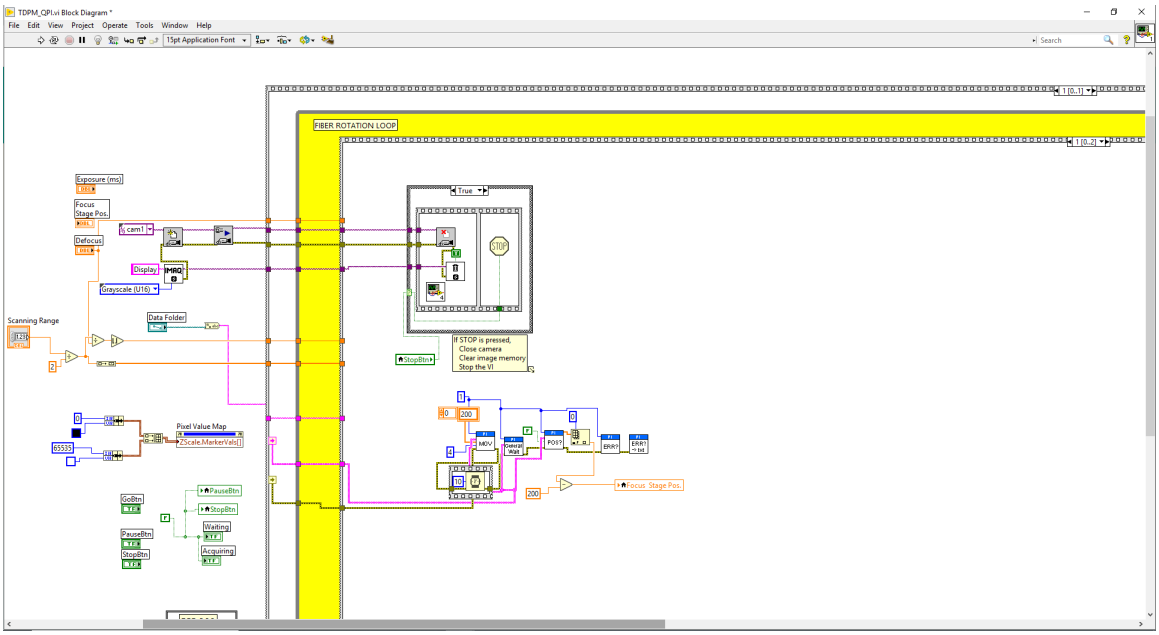

Figure 3.17: Frame 1 of SSS2. This frame brings the POS back to the middle “in-focus” plane for the next stack of intensity patterns.

During the entire sequence, the user can “PAUSE” or “STOP” the program at any time as needed. The program should be run until after the stack of patterns for 180 degrees is recorded. The user then needs to press the “STOP” button to end the program completely.

According to the datasheet, the pixel size in the Pixelink camera, is 3.45 microns x 3.45 microns. However, with various optical components in the optical path of the camera, the “Effective Pixel Size (EPS)” becomes the quantity of interest. EPS was measured to be 4.61

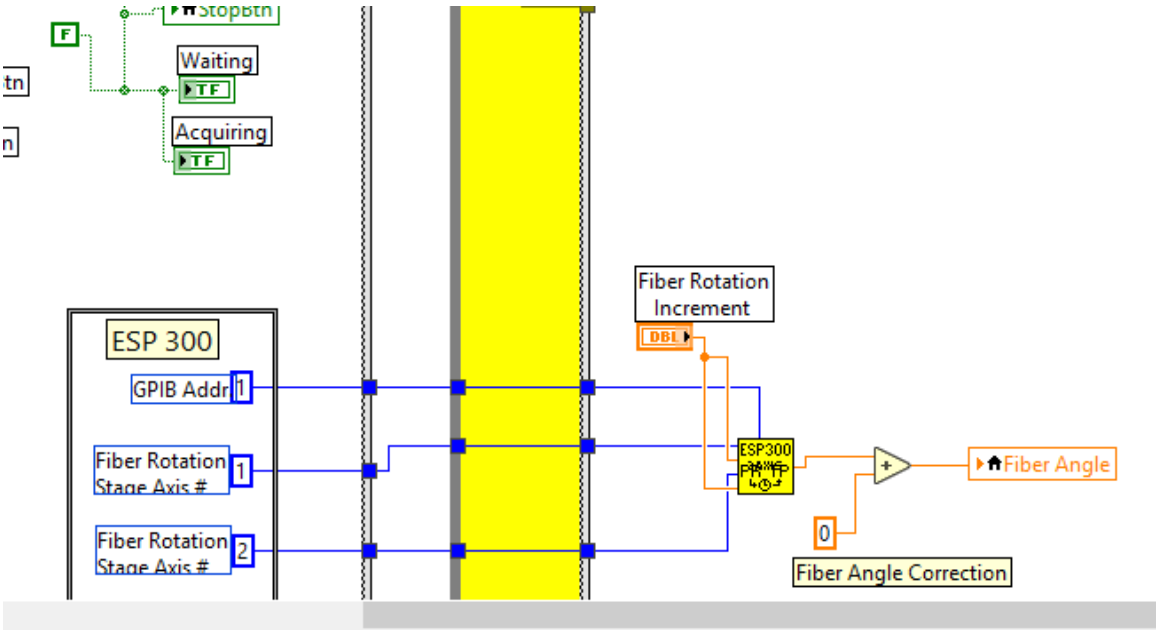

Figure 3.18: Frame 2 of SSS2. This frame commands the ESP300 motion controller to rotate the SR50PP rotation stages by the specified angle increment value.

microns, without the effect of objective magnification. This value is used in calculating the defocus distance for the data acquisition process. The formula to calculate the defocus distance is given by:

$$\Delta z = \frac{\Delta x \cdot \omega}{n_{\text{oil}}} \tag{3.2}$$

where Δz is the defocus distance, Δx is the EPS for a given objective magnification, "ω" is a free parameter used in the TDPM image processing code, and "n_{oil}" is the refractive index of the index matching oil. The EPS for a given objective magnification is given by:

$$\Delta x = \frac{4.61\ \mu\text{m}}{M_{\text{obj}}} \tag{3.3}$$

where $4.61\mu m$ is the measured EPS of the without the effect of objective magnification, and M_{obj} is the magnification of the objective lens in use. The ω parameter in the previous QPI system was $M_{\text{obj}}/10$ and remains the same in the new system. Therefore, combining

Eq. (3.2) and (3.3), the expression for defocus distance is given by:

$$\Delta z = (0.461\ \mu\mathrm{m}/n_{\mathrm{oil}}) \tag{3.4}$$

MFPI-PC LabVIEW program

The LabVIEW program for 2D QPI (MFPI-PC method) has the same working principle as the TDPM program. However, 2D QPI does not require defocused intensity patterns recorded from multiple angles. Hence the rotation stages are not used. Consequently, the ESP300 motion controller also remains unused in this program. Since the rotation is not involved, there is no need for a "fiber rotation loop" or an SSS2 in the LabVIEW block diagram. Thus, only two stacked sequence structures are used in the program - SSS1 (responsible for initialization of the system) and the SSS3 from the TDPM program (containing the defocusing loop and POS operations). There is only one stack of intensity patterns recorded for 2D QPI, and hence the process is completed much quicker than the data acquisition process for TDPM.

The user must set the microscope in Koehler illumination before using it for QPI with any of the LabVIEW programs. The procedure to set the microscope in Koehler illumination as well as the complete procedure to operate the QPI system is described in a "user manual". The user manual was developed as a reference guide for a new user, and is included as Appendix A.

The new QPI system was used for performing multiple 2D QPI experiments using the MFPI-PC method. In Chpt. 4, the results of these experiments are discussed, and are used to validate the 2D QPI theories developed at the Optics Laboratory.

CHAPTER 4
EXPERIMENTAL RESULTS

The new QPI system described in Chpt. 3 was used to perform multiple 2D QPI experiments using the MFPI-PC method, with custom-fabricated phase masks as test objects. In the present chapter, results of the experiments performed using disk and annular illumination are analyzed and the two are compared using spatial frequency response. Results of the 2D QPI experiments are also compared to the theoretical analysis from [81, 82, 156].

The requirement for custom-fabricated phase masks, their design, and the various values associated with the two phase masks are discussed in the following section.

4.1 Phase Masks

The 2D QPI methods developed at the Optics Laboratory, Georgia Tech were validated with specific objects like a visible transmission grating [48], a Corning SMF-28 optical fiber [48], and a Thorlabs MLA150-7AR microlens array [82].

However, it was determined that a standard calibrated test object with known spatial and phase variations was required to improve the experiments by avoiding the use of specific test objects. Such an object would be useful to compare the performance of the QPI methods under annular and disk illumination. In order to meet this requirement, researchers at the Optics Laboratory at Georgia Tech designed two "phase masks", namely "G01", and "G02". Both the phase masks were made from S1-UV grade Silica substrates. Patterns similar to the USAF Resolution Test Chart were etched on the two masks using Electron Beam Lithography (EBL). In Fig. 4.1, the resolution test chart patterns etched on the phase masks are illustrated. In both G01 and G02, the bars (ridges) were raised above the surface of the mask. The substrate had a uniform thickness and the bars had a specific height in the vertical direction. The gaps between the patterns (lateral dimensions) were same in both

the G01 and G02 masks. However, the height of the ridges was different in the two masks, which determined the phase delay in the light transmitted through the ridges. Since the entire mask was fabricated using the same silica substrate, the refractive index was uniform throughout the mask in both G01 and G02. Detailed information about the dimensions of the patterns on the masks and a summary of the fabrication parameters is provided in Appendix B.

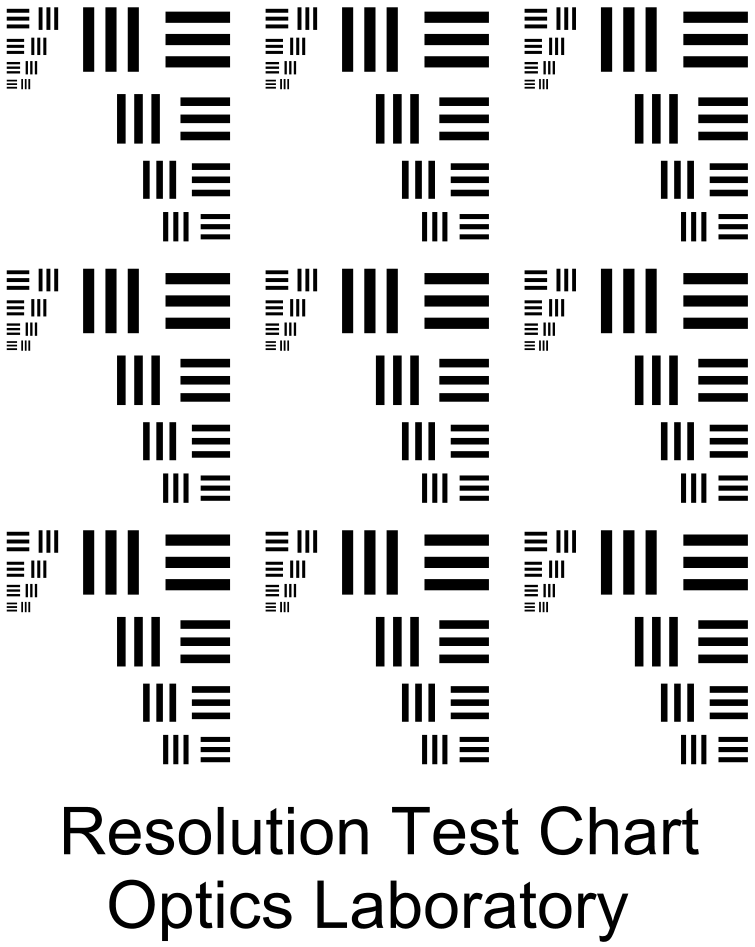

Figure 4.1: USAF Resolution Test Chart patterns on the phase masks G01 and G02.

Phase delay in light transmitted through different regions in a sample is dependent on the Optical Path Length (OPL). The OPL is given by the product of refractive index and the thickness of the sample along the optical axis. Since the refractive index was uniform

throughout the phase mask, the OPL depended only on the thickness of the mask along the optical axis. Furthermore, since the thickness of the substrate background was uniform, the phase delay was dependent only on the height of the ridges. The schematic diagram in Fig. 4.2 shows a phase mask that is illuminated from below. A ridge (bar) is represented by the raised section (region B) in the figure whereas the substrate background is represented by regions A and C. The height of the ridge is represented by h. The refractive index of the silica substrate, n_2, is 1.4601 for a wavelength of 546 nm. The term n_1 is the refractive index of air.

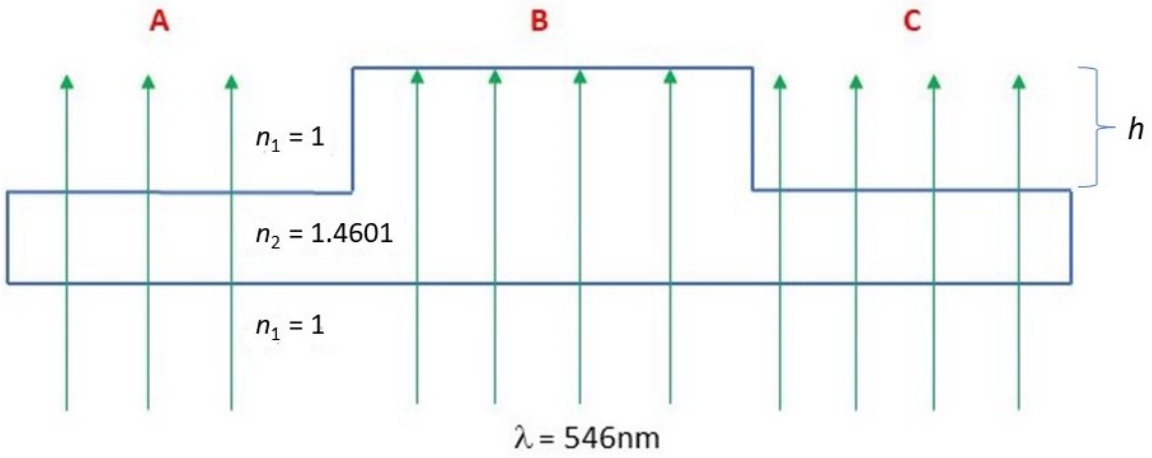

Figure 4.2: Schematic diagram showing the light transmitted through various regions in the phase mask. Light passing through region B experiences a phase delay (ϕ) compared to the light through regions A and C.

As shown in Fig. 4.2, the light transmitted through the ridges (light in region B) travels a longer distance (h) in a higher RI medium as compared to the light transmitted through the rest of the mask (light in regions A and C travel the h distance through air). Therefore, the light transmitted through the ridges has a phase delay (ϕ) compared to the light through the air, given by:

$$\phi = 2\pi f \Delta t \tag{4.1}$$

where $f = c/\lambda$, and Δt is the difference between the time required for light to travel

distance Δx through the ridge and through air. Therefore,

$$\Delta t = \frac{h(n_2 - n_1)}{c} \tag{4.2}$$

From Eq. (4.1) and Eq. (4.2),

$$\phi = 2\pi(n_2 - n_1)\left(\frac{h}{\lambda}\right) \tag{4.3}$$

The "etch depth" or the height of the ridges (h) was measured using atomic force microscopy as 74.8 ± 1.8 nm in G01, and 179 ± 3 nm in G02. Using Eq. (4.3) and the etch depth values, the phase delay (ϕ) in light transmitted through ridges compared to the light transmitted through the air was calculated to be 0.396 radians for G01, and 0.948 radians for G02. Table 4.1 provides a summary of the various values associated with the two phase masks.

Table 4.1: Summary of the characteristics of the two custom-fabricated phase masks. The masks are made from S1-UV grade fused silica (RI of silica at 546 nm is 1.4601).

Attribute	**G01**	**G02**
Etch Depth	74.8 nm	179.0 nm
Etch Depth Standard Deviation	1.8 nm	3.0 nm
Optical Phase Delay of Ridges at 546 nm	1.257 rad.	3.007 rad.
Optical Phase Delay of Air at 546 nm	0.861 rad.	2.060 rad.
Optical Phase Difference between Ridges and Air (ϕ)	0.396 rad.	0.948 rad.

4.2 2D QPI Experiments and Results

Results of the 2D QPI experiments performed on the G02 phase mask using the MFPI-PC method are discussed in this section. The phase images from disk and annular illuminations were compared and the potential advantages of using annular illumination [82] were verified experimentally.

First, an overview of the experimental configuration is provided in the following subsection.

4.2.1 Experimental Configuration

The configuration used for the experiments included the new QPI system (Chpt. 3), an Olympus UmPlanFl 50x objective with NA equal to 0.75 (NA_{o} = 0.75), an Olympus U-POC-2 condenser (C1) for disk illumination, and an Olympus U-PCD2 phase contrast condenser (C2) for annular illumination. The condenser C1 and the microscope objective used in the experiments are shown in Fig. 4.3, and the condenser C2 is shown in Fig. 4.4.

Figure 4.3: Left: Olympus U-SC swing out achromatic condenser with adjustable NA setting (used for disk illumination). Right: Photograph of the Olympus UmPlanFl 50x objective used in the experiments (The objective is attached to the POS).

The condenser C2 has annuli of different sizes for use with corresponding phase contrast objectives in PCM experiments. However, for 2D QPI experiments, the condenser C2 was used with conventional microscope objectives. Similar to the experiment presented in [82], the "40x" setting in condenser C2 was used. The condenser annulus corresponding to the "40x" setting had $NA_{\mathrm{c}} = 0.331$ and $NA_{\mathrm{ci}} = 0.293$. To match the condenser NA in case of disk illumination to that in case of annular illumination, the condenser C1 was set to

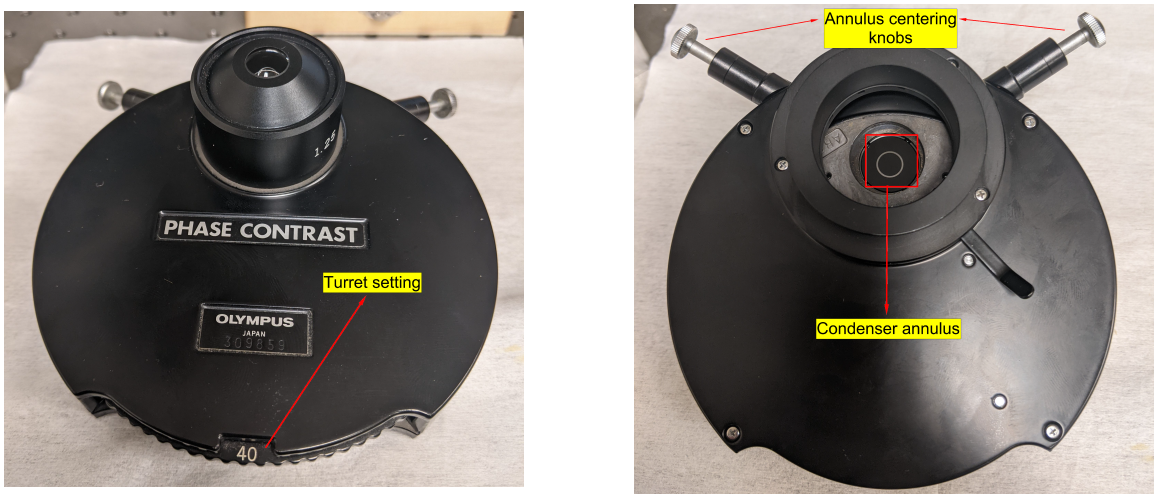

Figure 4.4: Olympus U-PCD2 phase contrast condenser. Left: top face of the condenser with turret setting. Right: bottom face of the condenser with annulus centering knobs and condenser annulus highlighted in red (used for annular illumination).

have NA_c of 0.331. Naturally, the inner NA of the condenser in case of disk illumination was zero. The schematic representation shown in Fig. 2.3 provides a visual reference to understand the various NA values mentioned above.

The defocus distance between the two consecutive defocus positions of the objective was set to be 0.6 microns. The POS moved the objective by 0.6 microns after an intensity pattern was recorded. The intensity patterns were recorded when the objective was positioned at any of the 15 defocus planes above or below the "in-focus" plane. In total, 31 intensity patterns (including one with objective at the in-focus position) were used to reconstruct the phase image of the G02 mask.

The EPS of the camera without the effect of objective magnification was measured to be $4.61\ \mu\text{m}$. In the new QPI system with the 50x objective, the EPS of the camera was 92.2 nm, i.e. every pixel in the intensity pattern corresponded to 92.2 nm.

The results of the 2D QPI experiments on G02 phase mask are discussed in the following sub-section.

4.2.2 Results

A stack of defocused intensity patterns was recorded each for the disk and the annular illumination cases. The two images in Fig. 4.5 depict the intensity patterns recorded when the objective is at the "in-focus" plane (left), and when the objective is at the 7th defocus plane above the "in-focus" plane (right). The patterns on the G02 mask were transparent when the mask was in crisp focus, as shown in the left image in Fig. 4.5, and thus satisfied the "weak scattering" condition often observed in unstained biological samples.

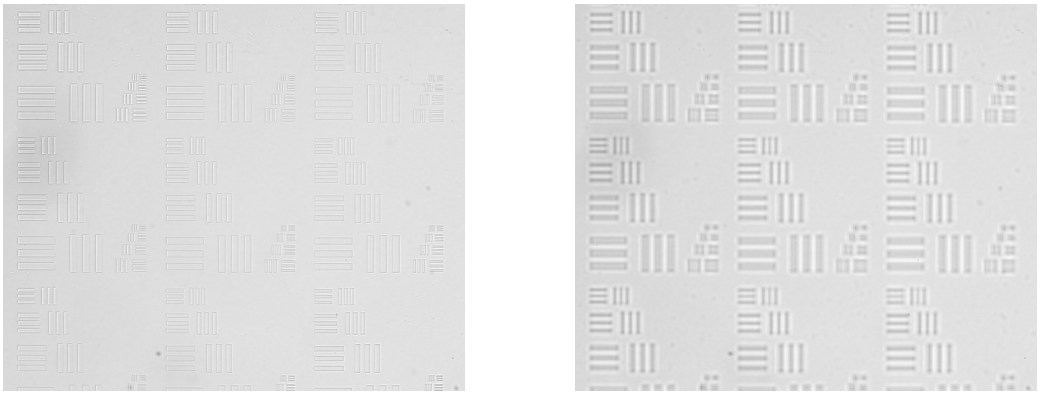

Figure 4.5: Intensity pattern recorded by the camera when objective is at the "in-focus" plane (left), and when the objective is at the 7th defocus plane above the in-focus plane (right).

Figure 4.6 depicts the phase images reconstructed using the WLS-MFPI-PC method [82] for the disk and the annular illumination cases. The reconstructed phase images show the test chart patterns in high contrast. The red outlined regions on the phase images contain a unique set of patterns on the mask, and also signify the imaging area used for the spatial frequency response analysis explained in the later section. Annular illumination phase image shows a higher contrast between the ridges and the background.

Phase Measurement

Figure 4.7 and Fig. 4.8 show the phase variation over the rows highlighted by yellow lines in the G02 mask phase images for disk and annular cases respectively (Fig. 4.6). The phase

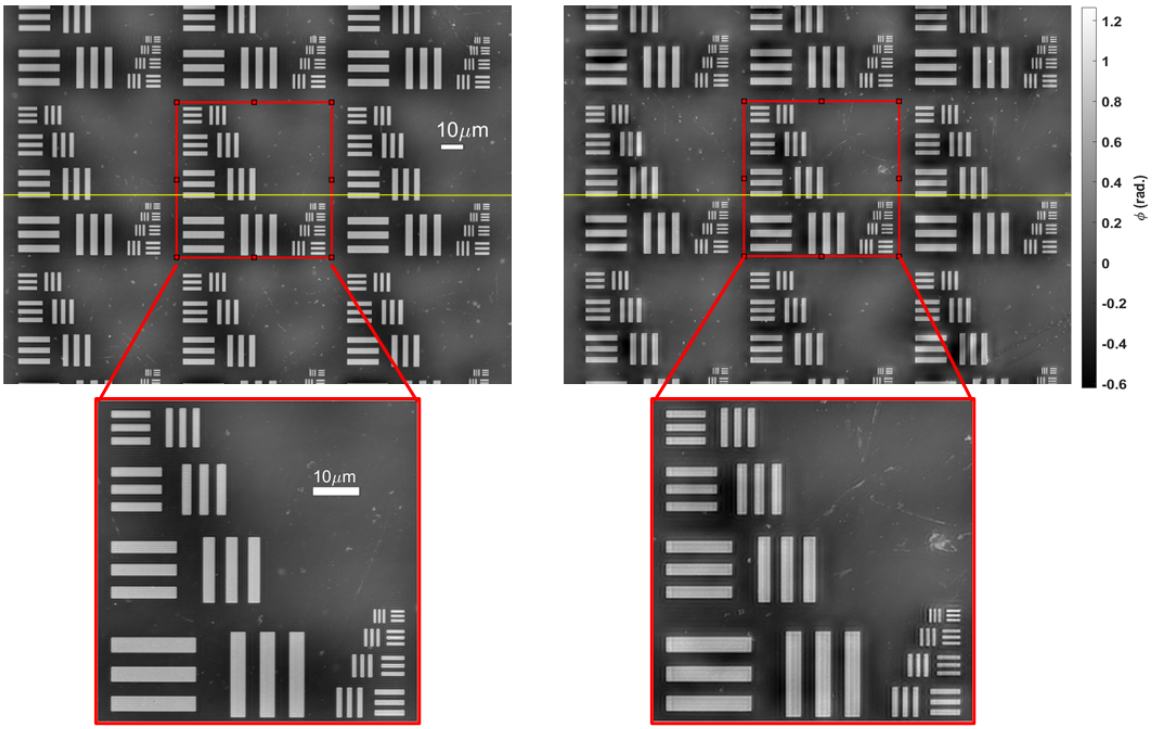

Figure 4.6: Reconstructed phase images using for disk illumination (left) and annular illumination (right) cases. The magnified region shows the image area used for spatial frequency response analysis.

variation exhibits sharp edges and a low frequency component in the background in both the cases. The low frequency component affects the background and the ridges equally which makes the top and bottom edges of the ridges parallel in the line profile. To calculate the phase delay in ridges, an approximate linear fitting was used to eliminate the effect of background variation. Since, all the ridges on the mask were of equal height, the phase delay of the light through all the ridges was expected to be equal. In the disk illumination phase image, the average phase delay was measured to be 0.9689 rad. with a standard deviation of 0.0415 rad. whereas in the annular illumination phase image, the average phase delay was 0.9311 rad. with a standard deviation of 0.0623 rad. Note that the ideal value from AFM measurements for G02 mask was 0.948 rad.

Although the measured values are close to expected values, better phase measurements can minimize the approximations in linear fitting and improve the results. Nevertheless, the measured phase values for both the illumination cases are within one standard deviation

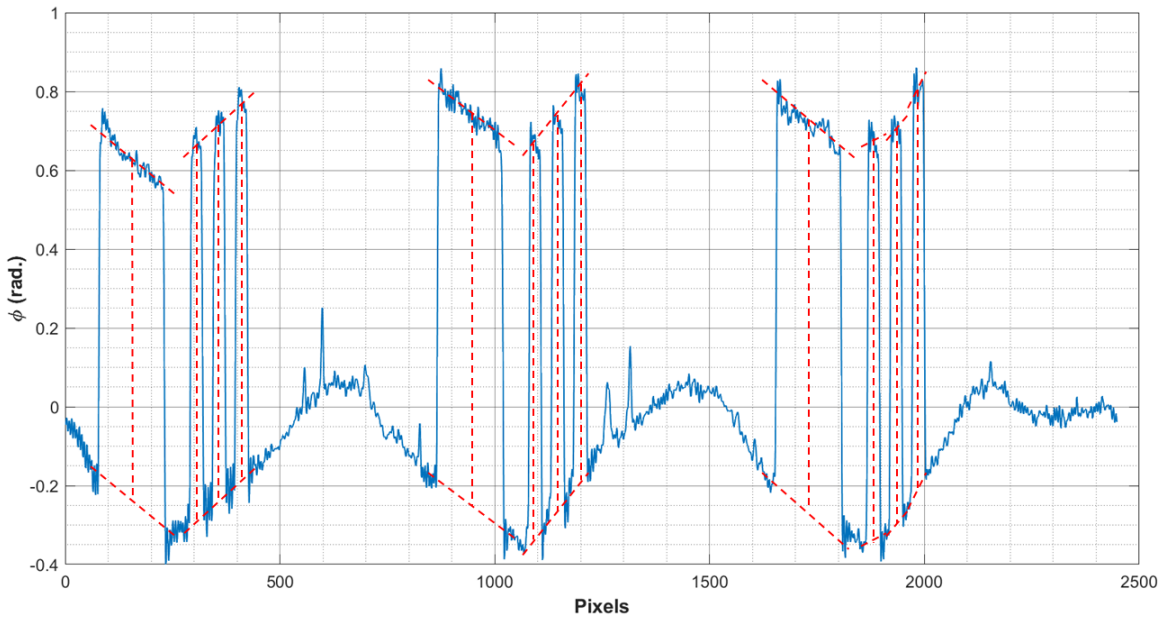

Figure 4.7: Line profile over the highlighted row (yellow) in disk illumination phase image of the G02 mask.

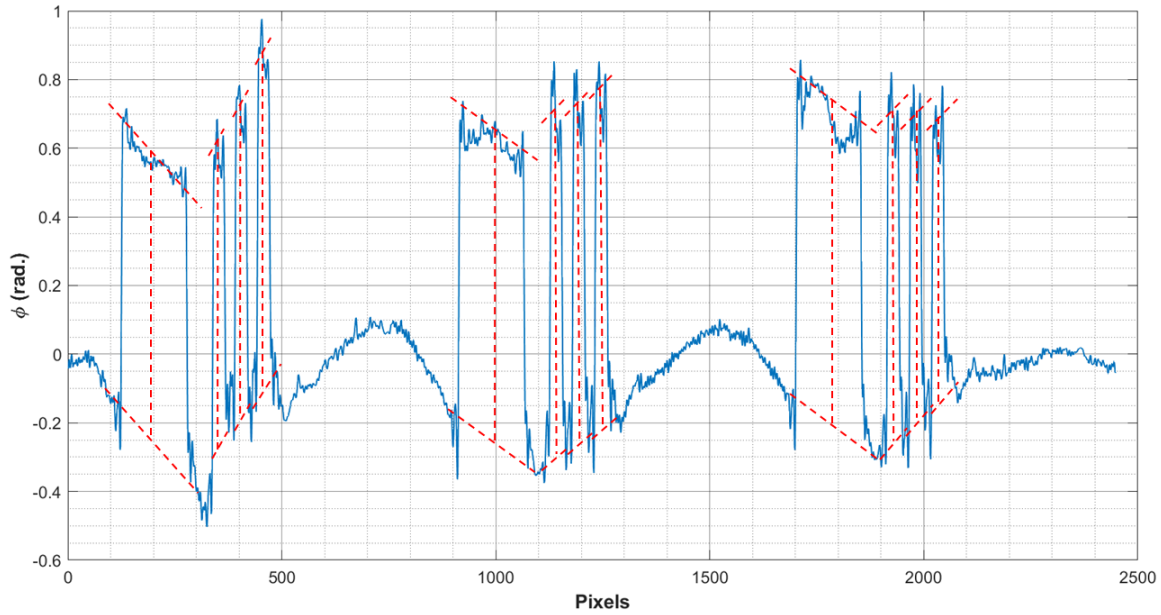

Figure 4.8: Line profile over the highlighted row (yellow) in annular illumination phase image of the G02 mask.

from the ideal value. Thus, the WLS-MFPI-PC method is highly reliable for phase recovery and holds promise for ubiquitous applications in phase imaging.

Spatial Resolution Estimation

The smallest patterns on the G02 phase mask had a center-to-center distance of $1\ \mu\mathrm{m}$. Figure 4.9 illustrates a magnified image of the smallest patterns on the mask for the disk illumination (left) and the annular illumination (right) cases. In both the cases, the smallest patterns are resolved clearly and do not represent the smallest resolvable distances. However, the higher contrast in annular case resolves the smallest patterns better than the disk case, and corresponds to a higher resolution.

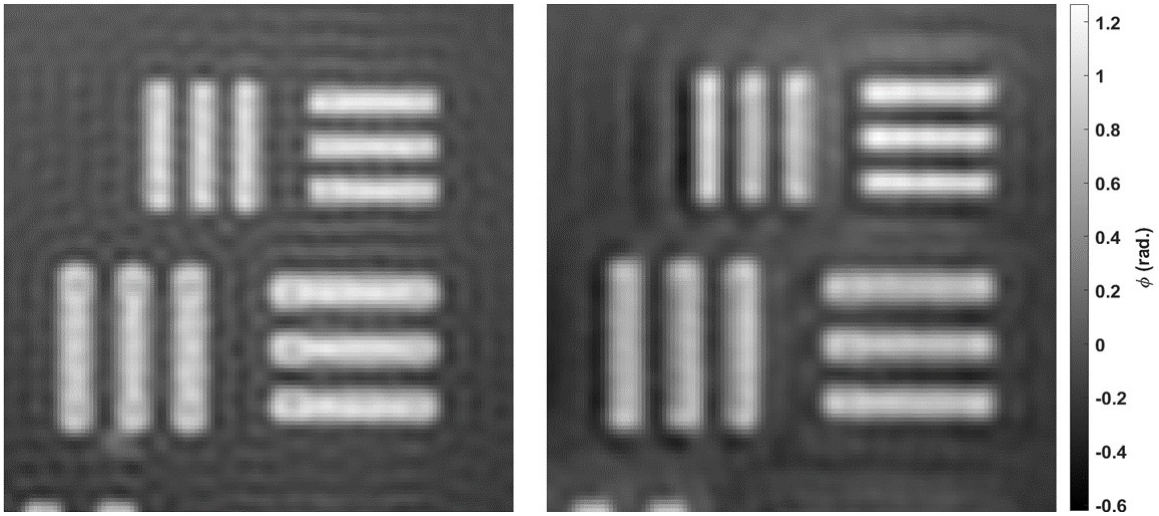

Figure 4.9: Smallest patterns on the G02 phase mask observed in (a) disk illumination (left), and (b) annular illumination (right).

A standard 1951 USAF resolution test chart comprises numerous groups of elements consisting of two patterns of three bars each. The number of lines per millimeter (spatial frequency, f_x) for any element is given by the formula:

$$f_{x,(K,n)} = 2^{K+(n-1)/6}\ \mathrm{lines/mm} \tag{4.4}$$

where *K* is the group number (G) and *n* is the element number (E). Fig. 3(b) in [138] displays a phase image of a standard 1951 USAF resolution test chart with the resolution represented by group 11 element 4 (G11E4) (highlighted in Fig. 3(c) in [138]). By comparing the smallest patterns in the disk and annular illumination phase images with the test

chart patterns in Fig. 3(b) from [138], the resolution in phase images corresponding to both the illumination types can be estimated.

Upon visual comparison, it was observed that the smallest patterns in the disk illumination case were resolved similar to the group 10 element 2 (G10E2) and the smallest patterns in annular case were resolved similar to the group 9 element 6 (G9E6) from Fig. 3(b) in [138], as shown in Fig. 4.10 and Fig. 4.11. Since the resolution is G11E4, the ratios of dimensions of G10E2 to G11E4 and G9E6 to G11E4 were used to estimate the resolution for disk and annular illumination cases respectively. It was calculated as follows:

$$R_{\text{Disk}} = \frac{f_{x,(10,2)}}{f_{x,(11,4)}}(1\ \mu\text{m});\ R_{\text{Annular}} = \frac{f_{x,(9,6)}}{f_{x,(11,4)}}(1\ \mu\text{m}) \tag{4.5}$$

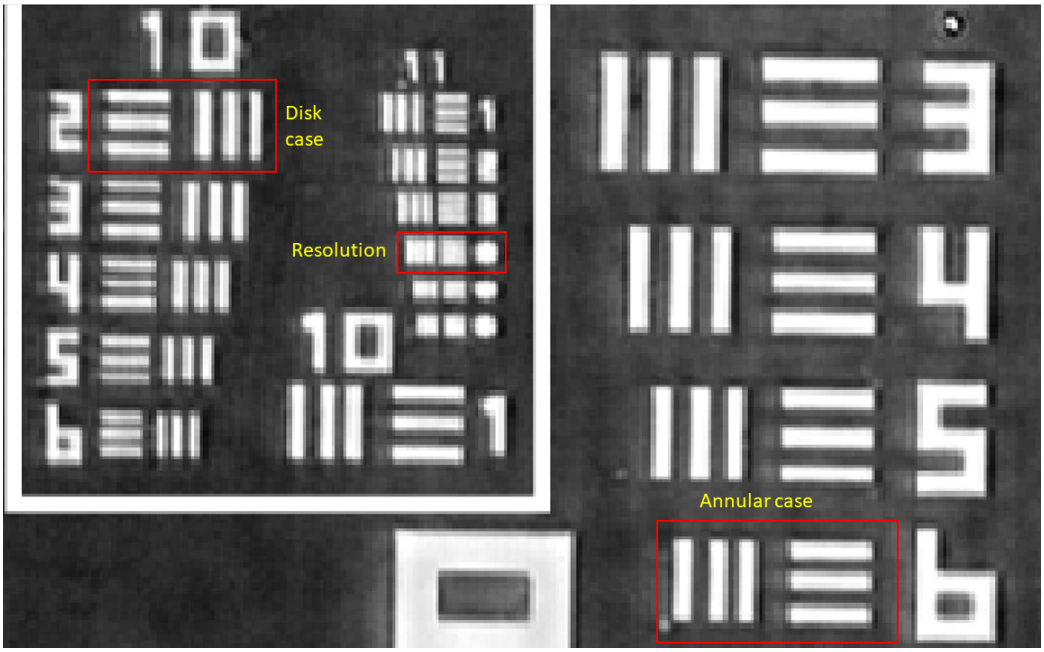

Figure 4.10: Comparison of disk and annular illumination phase images of G02 mask with Fig. 3(b) from [138]

Using Eq. (4.4) and Eq. (4.5), the resolution for disk illumination case was calculated to be 396.85 nm, and the resolution for annular illumination case was calculated to be 314.98 nm . The Rayleigh criterion for resolution limit of a microscope system is given by $0.61\lambda/(NA_{\text{c}} + NA_{\text{o}})$. For a wavelength of 546 nm, NA_{c} of 0.331 and NA_{o} of 0.75,

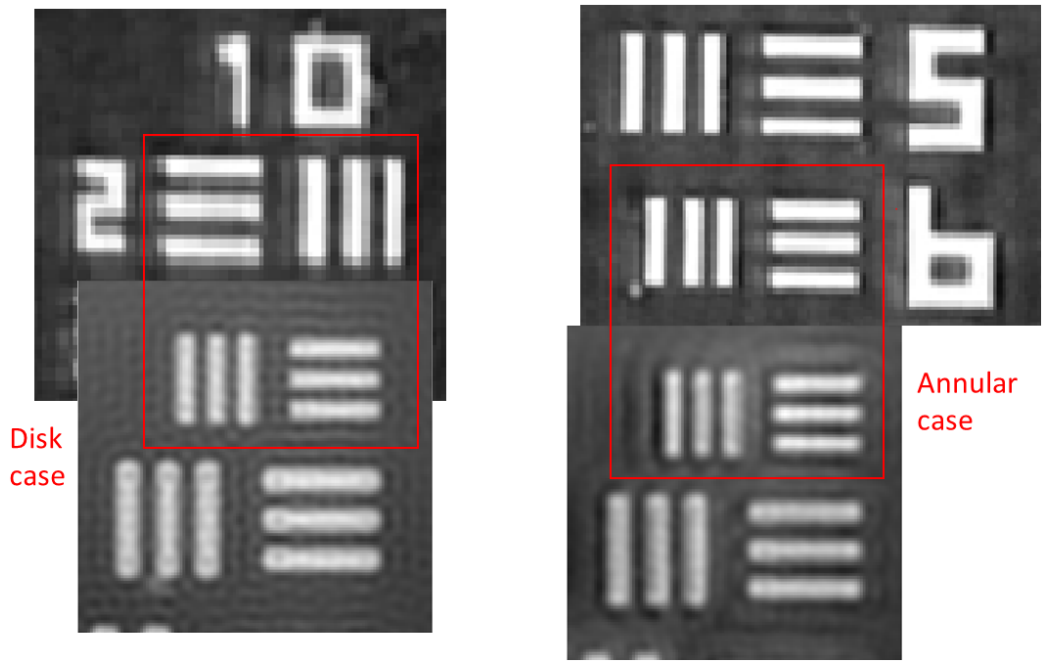

Figure 4.11: Smallest patterns in disk illumination case (in Fig. 4.9 left) are resolved similar to group 10 element 2, whereas the smallest patterns in annular case (Fig. 4.9 right) are resolved similar to group 9 element 6 from [166]

the theoretical resolution limit was calculated to be 308.1 nm. Therefore, the estimated resolution for the annular case is closer to the theoretical limit compared to that of disk illumination, validating the advantage of using annular illumination for higher contrast and spatial resolution.

Theoretical predictions and simulation results

In WLS-MFPI-PC, phase is recovered by inversion of individual PCTFs corresponding to each order of SGDF, instead of a common WD-PCTF for all SGDF orders (Fig. 2.4). This is because the individual PCTFs can have a larger absolute value than the WD-PCTF at a particular spatial frequency and lead to a better phase recovery. However, for this research, WD-PCTF variation as a function of spatial frequency was used for comparing the performance of disk and annular illumination. This was because the WD-PCTF for the combination of NA_{c}, NA_{ci} and NA_{o} used in this research did not go to zero in mid-frequency range, and provided a simpler alternative to having a combined PCTF from all

SGDF orders for their specific frequency regions. A larger WD-PCTF value is preferable for phase recovery as it corresponds to a higher SNR. Since WD-PCTF magnitude was sufficiently high in mid-range frequencies, its use for analysis instead of individual orders of SGDF still remains valid. The WD-PCTFs for disk and annular cases can be calculated by using Eq. (2.9) with Eq. (2.15), Eq. (2.18), and either Eq. (2.16) (disk illumination) or Eq. (2.20) (annular illumination). Figure 4.12a represents the 2D WD-PCTF for disk illumination case (T_{WD}) as a function of spatial frequency. For ease of understanding and comparison, an averaged 1D plot of the 2D WD-PCTF was calculated by utilizing the radial symmetry of the function. The 2D plot was divided into concentric rings of thickness $0.0146\ \mu\mathrm{m}^{-1}$ (1 pixel in frequency domain). One average value was calculated from each ring. With appropriate shifting of frequency axis, a 1D average of the radially symmetric 2D WD-PCTF was calculated and is shown in Fig. 4.12b. It should be noted that the 2D plot is a two-sided plot in all directions, whereas the 1D average plot shows the one-sided plot. Similarly, Fig. 4.13a shows the 2D WD-PCTF for annular illumination case (T_{WA}) and Fig. 4.13b shows its averaged 1D plot as a function of spatial frequency.

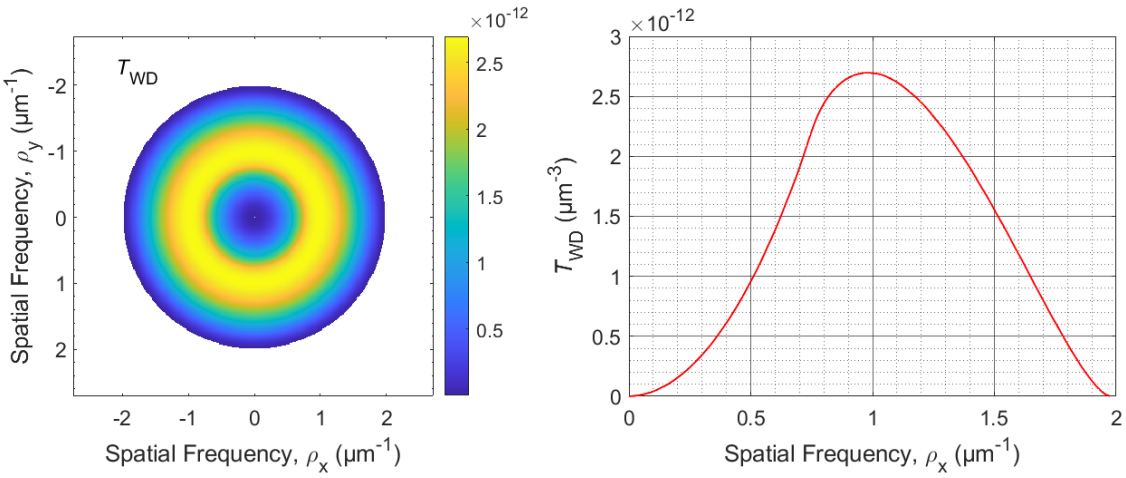

(a) (b)

Figure 4.12: 2D WD-PCTF for disk illumination case as a function of spatial frequency and its 1D average plot.

In Fig. 4.14, the averaged 1D plots of both T_{WD} and T_{WA}, as well as the plot of ratio

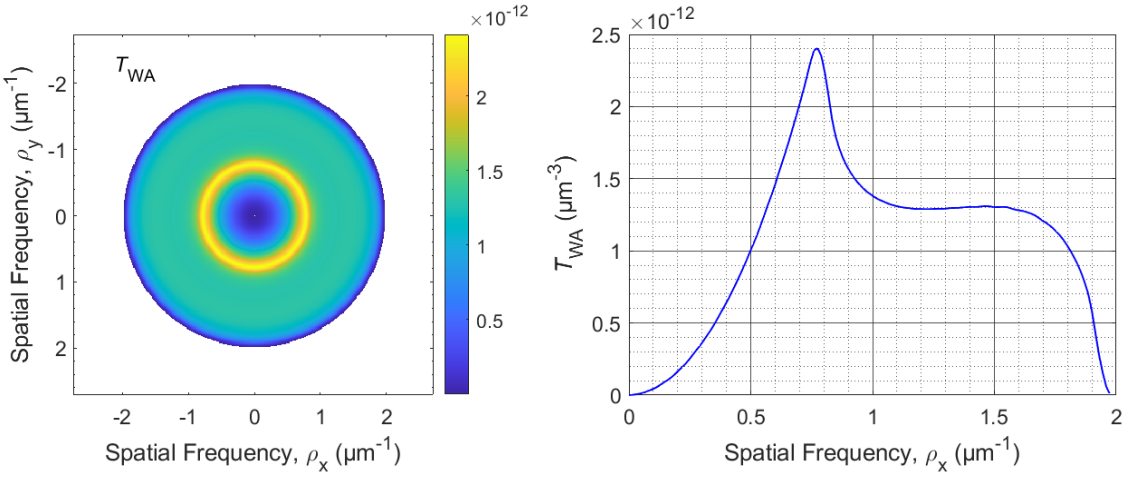

(a) (b)

Figure 4.13: 2D WD-PCTF for annular illumination case as a function of spatial frequency and its 1D average plot.

$T_{\mathrm{WA}}/T_{\mathrm{WD}}$ are shown. The variation of WD-PCTF as a function of spatial frequency shown in Fig. 4.14 has three regions. In the low-frequency region, the WD-PCTF for disk and annular illumination are almost the same, implying no advantage of one type over the other. In the mid-frequency region, the WD-PCTF for disk has a higher value than the annular WD-PCTF, implying that the phase recovery has a higher SNR for disk illumination. In high-frequency region, the annular WD-PCTF has a higher value than the WD-PCTF for disk case, implying that annular illumination is advantageous in higher spatial frequencies. This was explained in detail by Bao in [82]. Furthermore, the plot of log of ratio T_{WA} to T_{WD} predicts that the advantage of annular illumination in higher frequencies is much greater than its disadvantage in the mid-frequency region. In the following section, the difference in performance of the two illumination types based on experimental data is compared to the trend predicted by the three regions in the theoretically calculated WD-PCTF curves depicted in Fig. 4.14.

Furthermore, simulations were performed to compare the two illumination types and to check if their performance as a function of the spatial frequency followed the trends predicted by the theory. Figure 4.15a shows the reference phase image or the "ideal" case

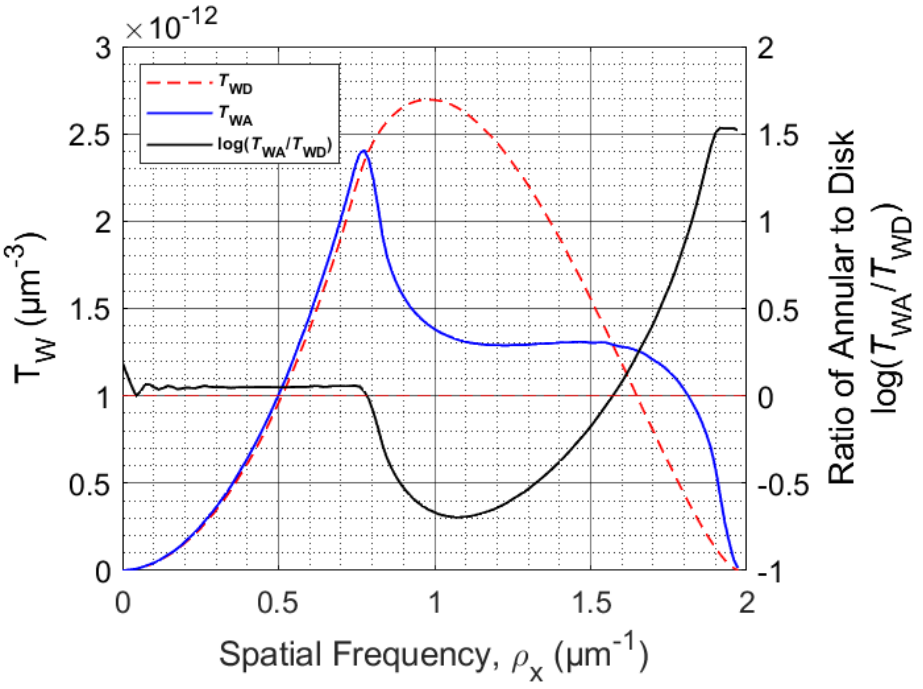

Figure 4.14: Averaged 1D plots of T_{WD}, T_{WA}, and the ratio $T_{\mathrm{WA}}/T_{\mathrm{WD}}$.

used in the simulations. It contains a set of patterns same as the one the G02 mask with a uniformly zero-valued background. However, the ridges have a phase delay value of 0.1 rad. instead of 0.948 rad. as in the G02 mask to make a closer approximation to the "weak object" assumption used in the MFPI-PC theory [48, 82]. Figure 4.15b and Fig. 4.15c illustrate the simulated phase images using the WLS-MFPI-PC method, with the same configuration parameters as the experimental configuration described previously. An SNR of 56 dB is used to approximate the noise in experimental conditions.

The spatial frequency response of the images is calculated using the 2D FFT of the images with zero frequency component at the center. The 2D FFT for the ideal case, disk illumination case, and the annular illumination case will be referred to as F_{ideal}, F_{Disk}, and F_{Annular} respectively. The "deviation" of the frequency response of the simulated images from the frequency response of the ideal image is given by:

$$\delta_{\mathrm{Disk}} = F_{\mathrm{Disk}} - F_{\mathrm{ideal}} \tag{4.6a}$$

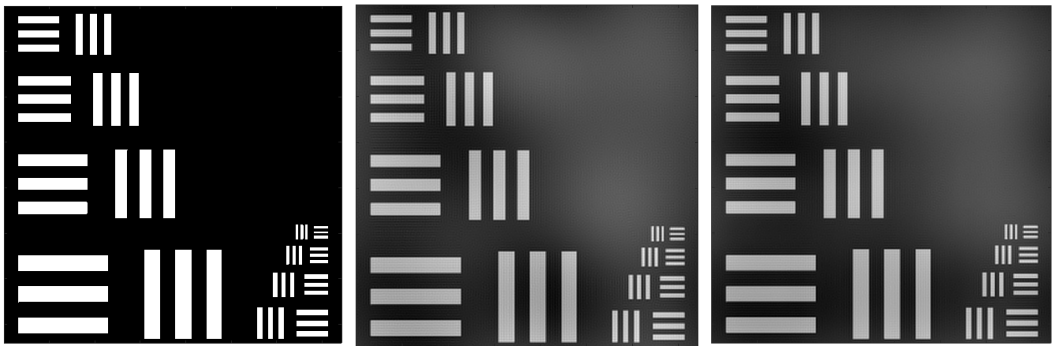

(a) Ideal image (b) Disk illumination (c) Annular illumination

Figure 4.15: Ideal image and the simulated phase images.

$$\delta_{\text{Disk}} = F_{\text{Annular}} - F_{\text{ideal}} \tag{4.6b}$$

where δ_{Disk} and δ_{Annular} refer to the 2D "deviation" from ideal case. This quantity is also used to calculate the deviation for experimental images in the following section. Figure 4.16 shows the averaged 1D plots of δ_{Disk} and δ_{Annular} normalized with respect to F_{ideal}. In the low frequency region, both the disk illumination (dotted) and the annular illumination (solid) curves have almost equal value of deviation, representing the similar performance region depicted in Fig. 4.14. In the mid-frequency region, the deviation in both annular and disk illumination is low, like the low-frequency region. In the high-frequency region, the deviation in the disk case is very high as compared to that in the annular case, implying a strong advantage of annular illumination in higher spatial frequencies. It should be noted that the deviation in frequency response cannot be quantitatively compared to the changes in WD-PCTF magnitude, as there is no explicit relationship between the two quantities.

The normalized difference of deviation ($\Delta\delta$) for simulated images is given by:

$$\Delta\delta = \frac{(\delta_{\text{Disk}} - \delta_{\text{Annular}})}{F_{\text{ideal}}} \tag{4.7}$$

where δ_{Disk} and δ_{Annular} refer to the deviation in the disk and annular cases respectively, and F_{ideal} refers to the spatial frequency response of the ideal image. This quantity directly

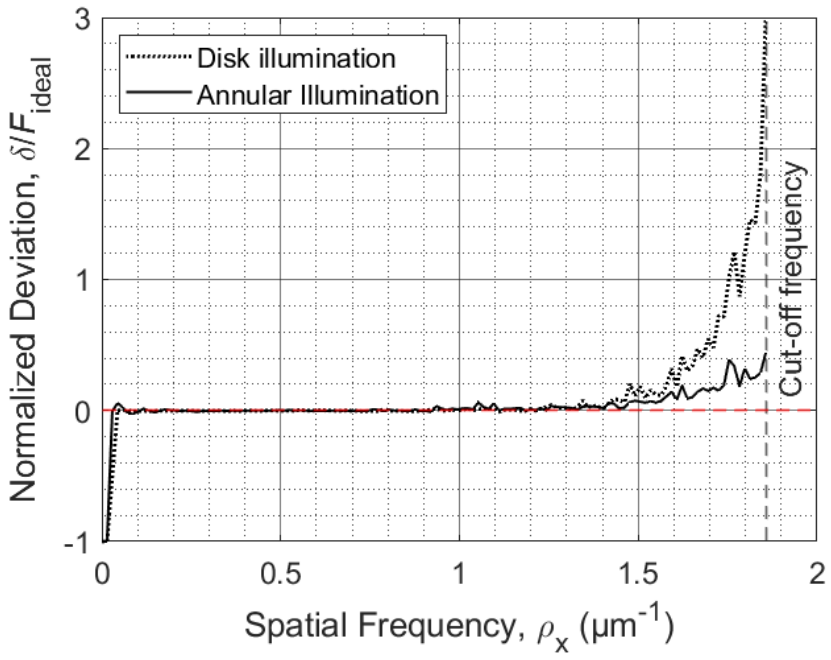

Figure 4.16: Averaged 1D plots of the normalized deviations for simulated phase images for disk and annular illumination cases.

represents the difference of performance of annular illumination over disk illumination in terms of the deviation of the spatial frequency response from the ideal response. If the normalized deviation is greater in the disk case than in the annular case, then $\Delta\delta$ is positive, whereas if it is higher in the annular case than in the disk case, then $\Delta\delta$ is negative. This quantity is also used in the following section to analyze the experimental images and compare it to the WD-PCTF curves.

Figure 4.17 shows the averaged 1D plot of $\Delta\delta$ (solid) and the log of the ratio $T_{\mathrm{WA}}/T_{\mathrm{WD}}$ (dotted). The three performance regions depicted in Fig. 4.14 are simulated successfully. Although the mid-frequency region in Fig. 4.16 does not show any noticable difference in the two illumination types, the difference becomes clear in Fig. 4.17 when the ratio of the two normalized deviations is depicted. Furthermore, the solid curve demonstrates that the advantage of annular illumination in higher frequencies outweighs its disadvantage in mid-frequency regions. This is because the positive peak of $\Delta\delta$ has a much higher absolute value than its negative peak. The cut-off frequency in both Fig. 4.16 and Fig. 4.17 is same

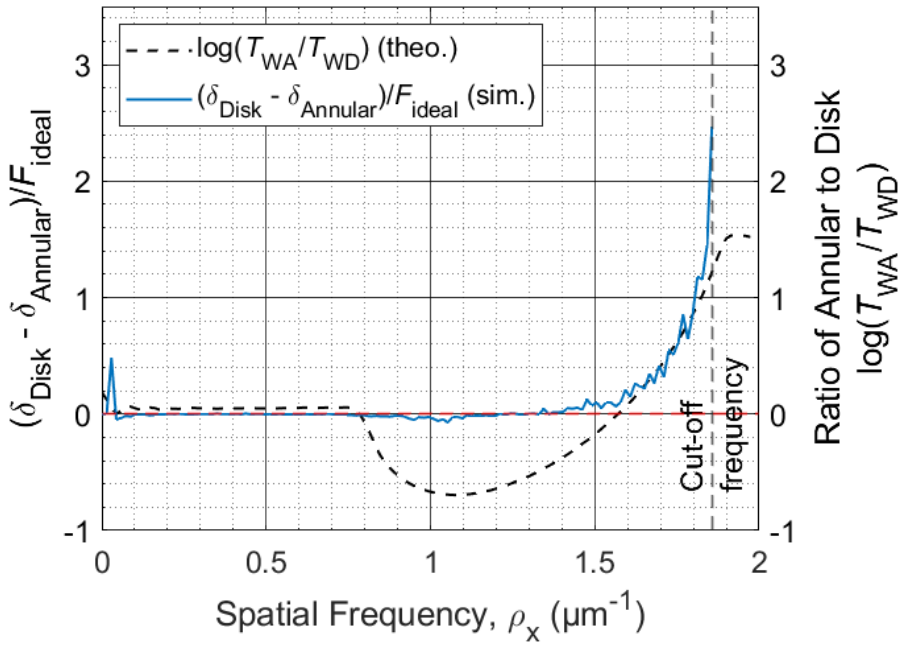

Figure 4.17: Normalized difference of deviation, $\Delta\delta$, for simulated images and the plot of $\log(T_{\mathrm{WA}}/T_{\mathrm{WD}})$.

as that in the experimental cases, and is dependent on the regularization threshold used in processing.

In the following section, a similar analysis is performed for experimental data and the performance of the two illumination types is compared to the simulation results and the theoretical predictions from [82]. The two illumination types are compared using normalized deviations (δ) and the normalized difference of deviation ($\Delta\delta$), to verify the trends in performance predicted by theory.

Experimental results and analysis

The present work comprises a detailed comparison of the performance of disk and annular illumination as a function of spatial frequency, using the WLS-MFPI-PC method. In order to make such a comparison, the spatial frequency responses of the experimental phase images from both the illumination types were compared to the spatial frequency response of an "ideal image". Furthermore, the comparison with "ideal response" was then com-

pared to the WD-PCTF variation over the same range of spatial frequencies to validate the theoretical model and predictions presented in [82].

Figure 4.18a shows the ideal image used as a true standard to compare the experimental performance of disk and annular illumination as a function of spatial frequency. The background in the ideal image is uniformly zero whereas the bars have a value of 0.948 corresponding to the ideal phase delay of 0.948 rad. expected in the light through the ridges in G02 mask. Figure 4.18b and Fig. 4.18c show the experimentally reconstructed phase images used for analysis of disk and annular illumination cases respectively (same as magnified area from Fig. 4.6). All three images have equal dimensions of 742×742 pixels with a pixel size of 92.2 nm. It is important to have the same pixel size in all three images. This ensures that the three images are sampled equally when their spatial frequency response is calculated and compared.

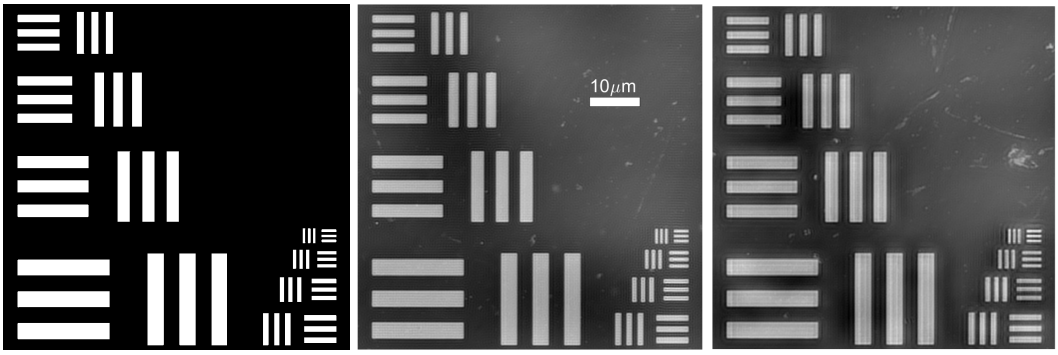

(a) Ideal image (b) Disk illumination (c) Annular illumination

Figure 4.18: Ideal image and the experimental images used for frequency response analysis.

Figure 4.19a and Fig. 4.19b show the 2D deviations for disk and annular illumination cases normalized with respect to the spatial frequency response of the ideal case, F_{ideal}. Here, F_{ideal}, F_{Disk}, and F_{Annular} correspond to the spatial frequency responses of the ideal and experimental images shown in Fig. 4.18. The radii of the two circles are defined by the cut-off frequency for disk illumination. It is the spatial frequency value at which the transfer function magnitude is lower than the regularization threshold used in processing. The averaged 1D plots of the two normalized quantities are presented in Fig. 4.20. The

dotted curve represents the disk illumination case whereas the solid curve represents the annular illumination case. In the low frequency region, the solid and the dotted curve have almost equal value, implying no advantage of using one illumination type over the other. In the frequency range 0-0.15 μm^{-1}, the value of transfer function is very low, which results in an unexpected peak due to the effect of noise. In the mid-frequency region, the deviation in annular case is higher compared to the disk case, implying an advantage of using disk illumination over annular type. However, in the high frequency region, the deviation from ideal is very high for disk illumination compared to the deviation for the annular case which is closer to zero value. This shows a strong advantage of annular illumination over the disk type. Low value of normalized deviation illustrates that the response for annular case is closer to the ideal response compared to the disk case in higher frequency region. Since the recovery of the fine details of a sample in the phase image is dependent on the higher spatial frequency components, the advantage of using annular illumination is significant. The two experimental curves in Fig. 4.20 clearly depict the three distinct regions from the theoretically calculated WD-PCTF curves in Fig. 4.14.

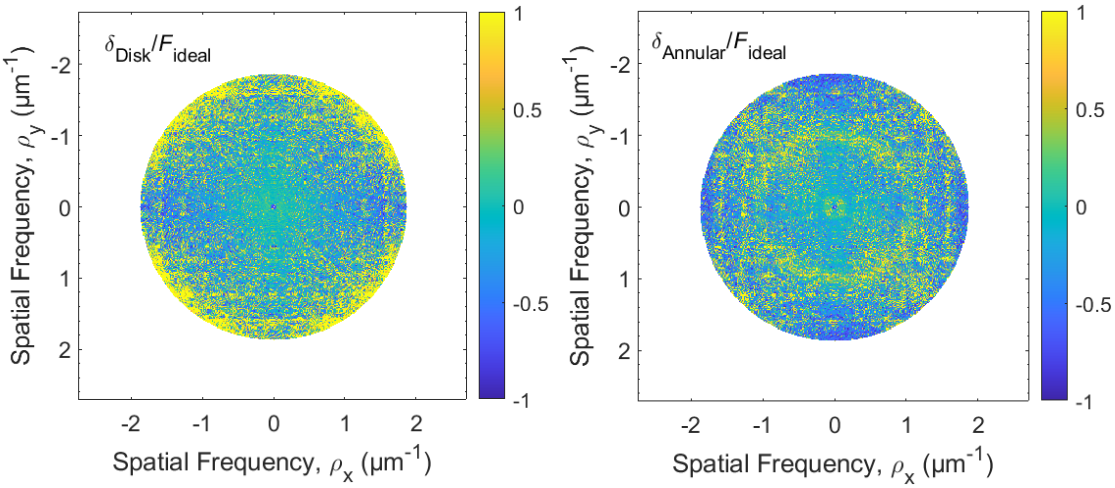

(a) Disk illumination, $\frac{\delta_{\text{Disk}}}{F_{\text{ideal}}}$.

(b) Annular illumination, $\frac{\delta_{\text{Annular}}}{F_{\text{ideal}}}$.

Figure 4.19: 2D deviations for experimental phase images using disk and annular illuminations, normalized with respect to F_{ideal}, as a function of spatial frequency.

Figure 4.21 shows the 2D plot of $\Delta\delta$ as a function of spatial frequency. The averaged

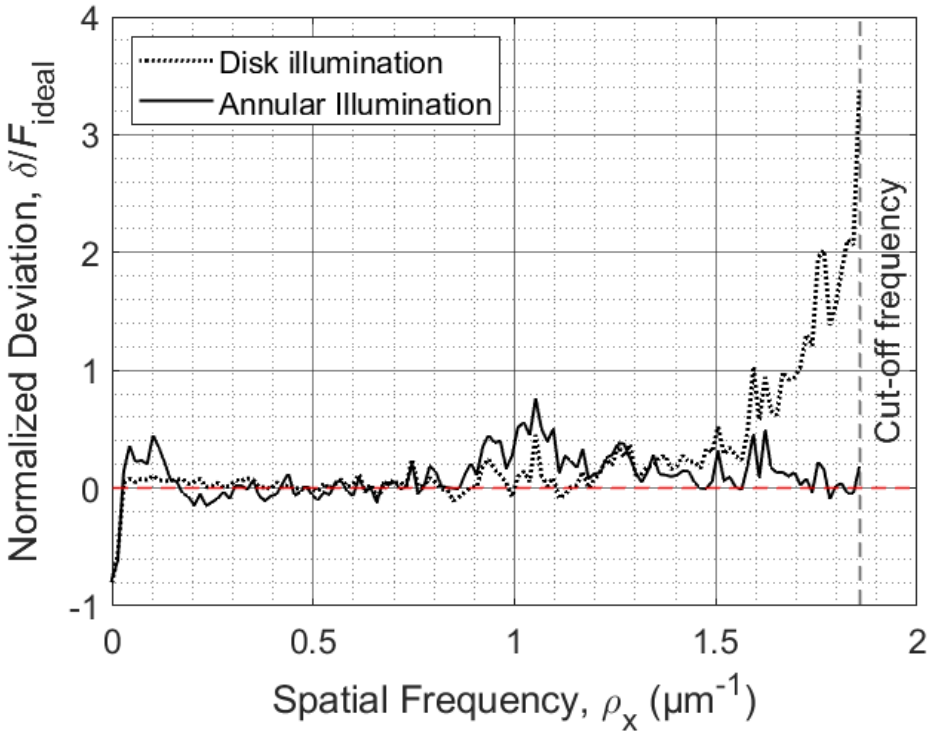

Figure 4.20: Averaged 1D plots of the normalized deviations for experimental phase images using disk and annular illumination types.

1D plot of $\Delta\delta$ as a function of spatial frequency is presented in Fig. 4.22, along with the 1D plot of the ratio of annular WD-PCTF to disk WD-PCTF (from Fig. 4.14). The experimentally obtained blue curve representing the normalized difference of deviation clearly highlights the three regions depicted by the theoretically calculated black curve and qualitatively follows its trend. Furthermore, the experimental curve validates the theory by showing that the advantage of annular illumination in higher spatial frequency compared to disk illumination is much higher than its disadvantage in mid-frequency regions.

It should be noted that the blue curve comes from the comparison of spatial frequency responses whereas the black curve comes from the ratio of WD-PCTF magnitudes. There is no analytical expression representing a relationship between the WD-PCTF magnitude and the spatial frequency response. However, it is known that a higher absolute value of the transfer function results in higher SNR, resulting in reliable phase recovery. Thus the

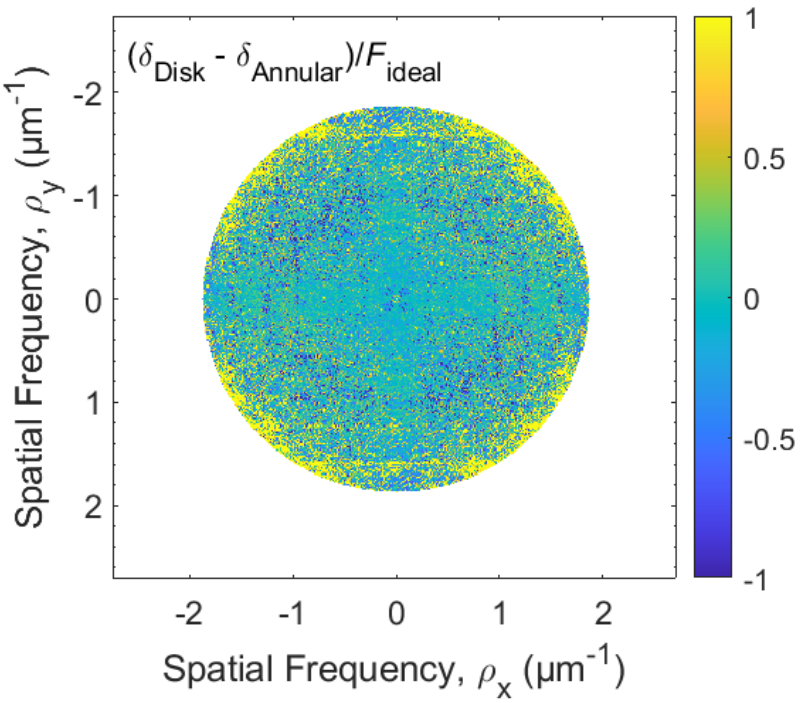

Figure 4.21: 2D plot of Normalized difference of deviation in disk and annular cases.

WD-PCTF and the experimental spatial frequency response curve can be used to compare the trend followed by the two curves.

In conclusion, the robustness of the WLS-MFPI-PC method and its reliability for phase reconstruction was illustrated using high contrast phase images of a standard-type phase test chart and the line profiles. The spatial resolution limits for both disk and annular illumination were estimated using a phase image of a standard USAF resolution test chart. Then Fig. 4.14, Fig. 4.20, and Fig. 4.22 were presented to compare the frequency response of disk and annular illumination phase images to that of the ideal case, and validate the theoretical predictions from [82] showing a significant advantage of annular illumination in recovery of higher spatial frequency components. Furthermore, the difference in performance of disk and annular illumination as a function of spatial frequency was analyzed and was found to match the trend from the three regions depicted in the theoretically calculated WD-PCTF curves.

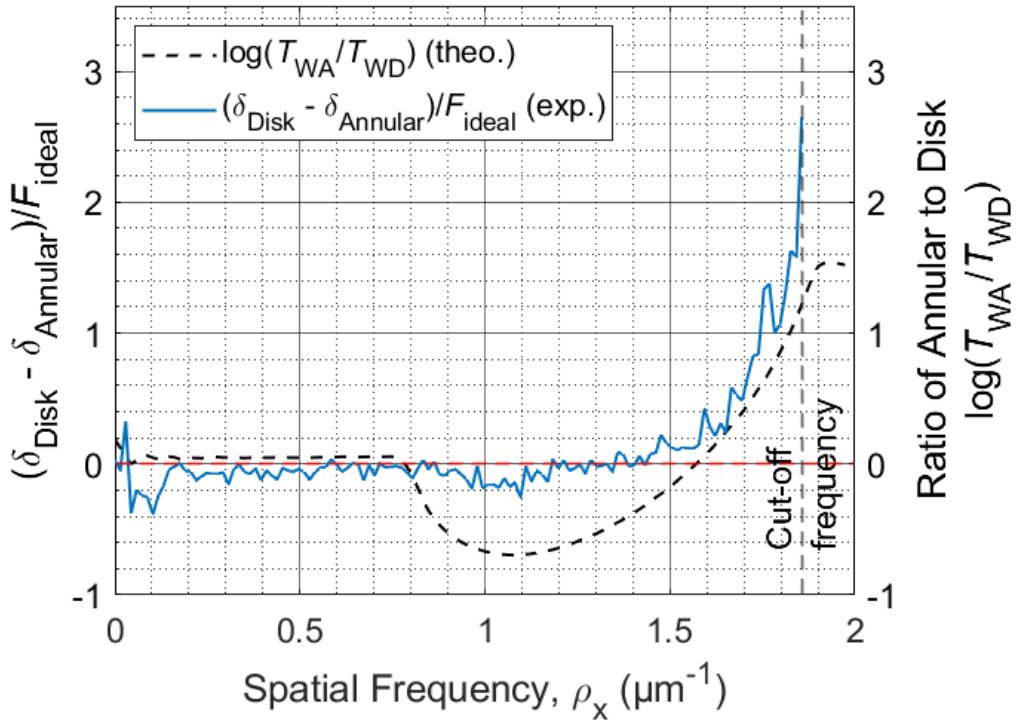

Figure 4.22: Averaged 1D plot of normalized difference of deviation and the ratio of annular WD-PCTF to disk WD-PCTF as a function of spatial frequency.

CHAPTER 5
RESEARCH SUMMARY AND FUTURE WORK

5.1 Summary of completed work

The main objective of this research was to analyze the performance of disk and annular illumination types in QPI and to provide an experimental validation of the theoretical model and predictions presented in [82]. This was completed by:

1. Developing a state-of-the-art QPI system for performing 2D and 3D QPI.

2. Performing 2D QPI experiments on custom-fabricated standard-type phase masks with disk and annular illumination, using the WLS-MFPI-PC technique.

3. Analyzing the spatial frequency response of the reconstructed phase images for disk and annular illumination cases, and comparing it to the theoretical predictions from [82].

The newly developed state-of-the-art QPI system was developed using conventional components and no extensive modifications to a standard bright-field microscope, or need for custom elements. Thus, a standard microscope setup in any lab can be used as a QPI system without making major modifications. The system comprised a microscope, a camera, an objective scanner to move the objective, and rotation stages to rotate the fiber. A phase-contrast condenser was used for annular illumination. LabVIEW 2019 was used to control the working of the system. The new QPI system and its working was described in Chpt. 3.

The phase images from the 2D QPI experiments performed on the phase masks were analyzed using spatial frequency response. An ideal image was used to compare the per-

formance of WLS-MFPI-PC using disk and annular illuminations. The following points were concluded from the analysis of phase images:

1. The phase images showed the patterns on the transparent phase mask in high contrast.

2. Annular illumination provided higher contrast in phase images, corresponding to a higher spatial resolution.

3. The phase values recovered using both the illumination types were close to the ideal values, and accurate within one standard deviation.

4. The expected value of phase delay was 0.948 rad., the phase delay value for disk illumination value was measured to be 0.9689 ± 0.0415 rad., whereas the phase delay value for annular illumination case was measured to be 0.9311 ± 0.0623 rad.

5. Spatial resolution limit was estimated for both the illumination types. The resolution limit for annular illumination case was estimated to be close to the theoretical resolution limit.

6. The theoretical resolution limit for the microscope configuration was 308.1 nm. The estimated resolution for disk illumination case was 397 nm, whereas the estimated resolution for annular illumination case was 315 nm.

7. Spatial frequency response comparison using an ”ideal image”:

    - The spatial frequency response in higher spatial frequency region for annular illumination case was better than that for disk illumination. Thus, annular illumination showed a performance advantage in high spatial frequencies.
    - In the low-frequency region, both the illumination types performed similarly. In the mid-frequency region, disk illumination had a slight advantage. In high spatial frequencies, annular illumination had a significant advantage.

- This trend was found to match the trend predicted by the WD-PCTF curves shown in Fig. 4.14 and in [82].

8. Annular illumination was proved to be advantageous in achieving higher spatial resolution and recovery of higher spatial frequency components.

Since the theory presented by Bao in [82] gives correct results, this analysis can be used to predict the improvement in high-spatial frequency response for a given combination of phase contrast condenser and objective lens and thus determine if the combination would be sufficient for a particular application, before using it. Furthermore, for a given objective lens, this analysis can be used to optimize the annulus dimensions for 1) the highest spatial resolution, 2) the best trade-off between high-frequency gain and mid-frequency loss, or 3) other requirements according to the specific application. In conclusion, annular illumination presents a promising low-cost approach for high-spatial frequency imaging.

5.2 Future Work

5.2.1 Phase Resolution Limit and New Results

The smallest patterns in phase images from Fig. 4.6 are resolved clearly and hence do not represent the resolution limit. Therefore, a ”phase resolution target” is required to determine the phase resolution limit i.e. the minimum detectable change in phase. Such a target is being designed and will be fabricated in the near future. The ”phase resolution mask” will have thin films of various deposition thicknesses to test the minimum thickness that can be detected accurately, in terms of phase delay. This can provide the axial resolution limit for the QPI methods and the two illumination types for a given QPI method. A series of experiments can be conducted to reconstruct the phase images for multiple configurations, and the images can be analyzed to calculate the average phase delay and its standard deviation. The axial resolution can be used to compare the performance of disk and annular illumination, in addition to the spatial frequency response-based comparison presented

earlier.

It is also important to experimentally determine the resolution limit. The resolution limit mentioned in Chpt. 4 is an estimation and should be tested using masks with correspondingly sized patterns. The existing masks do not have sufficiently small patterns and perhaps a new mask with even smaller patterns can be envisioned to test the spatial resolution.

Furthermore, experiments with different combinations of annuli and objectives can be performed to generate corresponding phase images. These phase images can be analyzed to verify if the results are consistent with other combinations.

5.2.2 Improvements in QPI System

The new QPI system developed as a part of this research is dependant on LabVIEW software for control and execution. This restricts the use of components to the ones that are compatible with the software. Furthermore, LabVIEW presents restrictions in the way the components can be used and programmed. This is because only the features accessible using LabVIEW can be used and programmed in the system.

In contrast, if the control program is developed using C++ or equivalent language then the system components can be selected and used as required, without depending on a commercial software and its compatibility requirements. Therefore, a C++ based improved QPI system should be developed with libraries for individual components and devices. Such a program could be open source and hence lead to widespread use of QPI.

In addition to the above improvements, the QPI system needs an improved mechanism to move the sample in lateral direction. This is important in applications like FBG characterization which requires accurate alignment of the FBG with optical setup, to generate good phase images. If the fiber is misaligned, it becomes difficult to re-align the fiber at the same exact location, and this can deteriorate the quality of the reconstructed phase images. If the microscope stage is moved then to preserve the alignment of the fiber with

the rotation stages, it is necessary that the fiber rotation stages move with it. Therefore, a microscope stage system is needed, with rotation stages attached to the microscope stage, and servo motors for movement in the three axes. Such a system is being developed at the Optics Lab and is expected to be ready for use in the near future.

Annular illumination for QPI experiments used in this research was produced using a standard phase contrast condenser. However the condenser had fixed set of annuli that cannot be changed according to imaging requirements or objective NA. This does not allow for the best use of annular illumination, and the resulting phase images may not be of the best quality, due to a mismatch between the NA of condenser annulus and NA of the objective. Therefore, a programmable LED array could be used as a source for annular illumination. The NA of the annular illumination produced using such an array could be easily changed by modifying the program. This would ensure the best use of annular illumination, and improve the performance of the QPI system.

5.2.3 FBG Characterization

One of the major applications of QPI is in the field of FBG characterization. FBGs have periodic refractive index variations in the longitudinal direction that allow only specific light wavelengths through the FBGs, whereas other wavelengths are reflected. The reflected wavelengths depend on the period of the grating and the effective refractive index in the fiber core. Recently, cross-sectional refractive index variations were observed in FBGs [51] that may be a result of the nonlinear effects in the manufacturing process. These cross-sectional variations were not observed previously and hence represent a new area of study.

Using QPI methods described in Chpt. 2 and the QPI system described in Chpt. 3, these cross-sectional RI variations should be studied in detail. The effect of these RI variations on the performance of FBGs should be analyzed in context of the applications of FBGs. Furthermore, the study of these RI variations can provide an insight into the nonlinear ef-

fects that generate these variations, as a result of the manufacturing methods. The existing manufacturing methods can be modified to either enhance or diminish these nonlinear effects depending on the effect of the cross-sectional RI variations on FBG applications. For example, if the cross-sectional RI variations help act as an advantage to the FBG performance for sensing applications, then the manufacturing processes for FBG sensors may be modified to enhance the RI variations.

Furthermore, various types of FBGs manufactured using different methods should be studied using QPI to characterize the effect of various structural nuances on their performance. With the results from such a study, QPI methods could be incorporated into the manufacturing processes to verify that the product exactly meets the design requirements.

5.2.4 Computational Advancements

The 3D QPI techniques like iterative TDPM have extensive computational requirements because of the large number of images and the iterative nature of algorithms. Conventionally, the phase images were processed using MATLAB which executes the program serially and takes long time to reconstruct final phase images. However, if the processing was performed in parallel, the processing time would be significantly reduced. As a result, a GPU-based parallel processing approach is being used to develop a new algorithm that makes use of CUDA libraries and reconstructs the phase images in short time. An Nvidia GTX GPU was used and a workstation was assembled to enhance the computational processing capabilities at the optics laboratory. When the developments are completed, the TDPM image processing time will be significantly reduced and it will be a step towards real-time 3D QPI using TDPM.

5.2.5 Concluding Remarks

The primary objective of this research was to compare the performance of disk and annular illumination in QPI, which was completed. The results showed that annular illumination

has significant advantages in higher spatial frequencies. Furthermore, the phase recovery performance as a function of spatial frequency followed the trends predicted by the theory. A thorough study of QPI using MFPI-PC was done and a new QPI system was developed for performing 2D QPI experiments used in this research. The use of annular illumination should be studied further as it represents a promising approach for improvements in phase imaging.

Appendices

APPENDIX A

W417 LAB QPI SYSTEM USER MANUAL

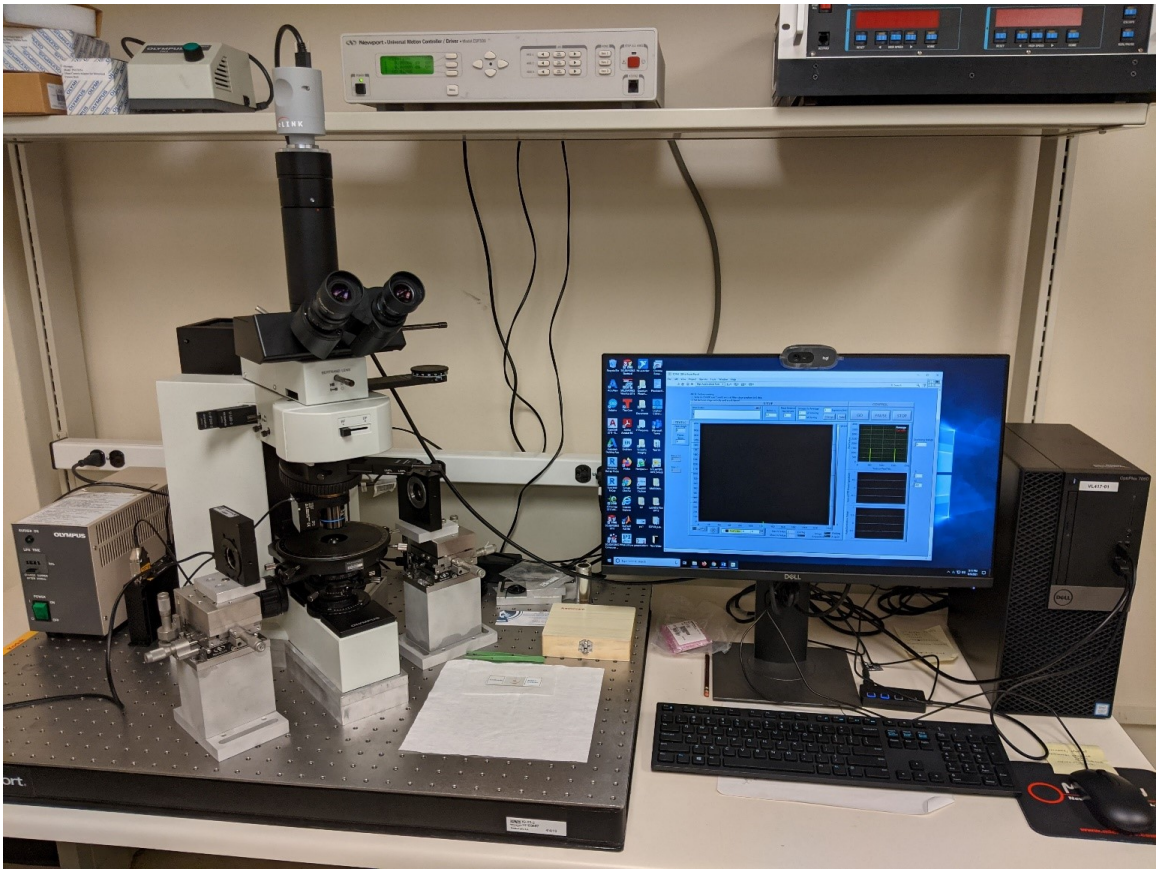

Prepared By:

Pranav P. Kulkarni

Gabriel A. Krivian

16th October 2021

A.1 Hardware and Software Overview

This document provides an overview of the W417 lab QPI system microscope hardware and LabVIEW software, and how they can be used to perform 2D and 3D quantitative phase imaging (QPI) measurements. The schematic of the 417 QPI system is shown in Fig. A.1. The system uses a non-interferometric method with a partially coherent light source to acquire phase images of weakly scattering objects such as phase masks, optical fibers, or biological cells. An Olympus BX60 microscope is used as the base optical microscope, and a Pixelink M5D 5 Megapixel CMOS camera is used to capture the images. A PI P725 Piezoelectric scanner connected to the objective lens of the microscope shifts the focal plane of the microscope along the optical axis of the sample at the set "defocused distances" specified in the LabVIEW program. An image at each of these defocused distances is then captured with the camera and stored to be processed later. A set of rotation stages is also connected to the system to enable the user to perform 3D QPI. The optical fiber (or capillary) is inserted into the rotation stages on either side of the microscope stage. These stages rotate the optical fiber by an amount specified in the LabVIEW program before the images are taken. Once all images have been taken at a given tomographic angle, the rotation stages rotate the sample again. This process continues until all images have been acquired for each tomographic angle and the sample has rotated through a total of 180°.

The entire system is controlled by virtual instruments (VIs) programmed in LabVIEW running on the Dell workstation computer adjacent to the microscope. The particular VI that is used depends on the task being performed, but in all cases, the interface remains the same. With the interface shown in Fig. A.2, the user can view 1) the images being captured, 2) the rotation angle of the sample with respect to its initial position, 3) the focus stage position, 4) the pixel values of a vertical column, 5) the Fast Fourier Transform (FFT) power spectrum, and 6) the autocorrelation values. With this interface, the user can also set parameters such as defocus distance, total scanning range, fiber rotation increment, and

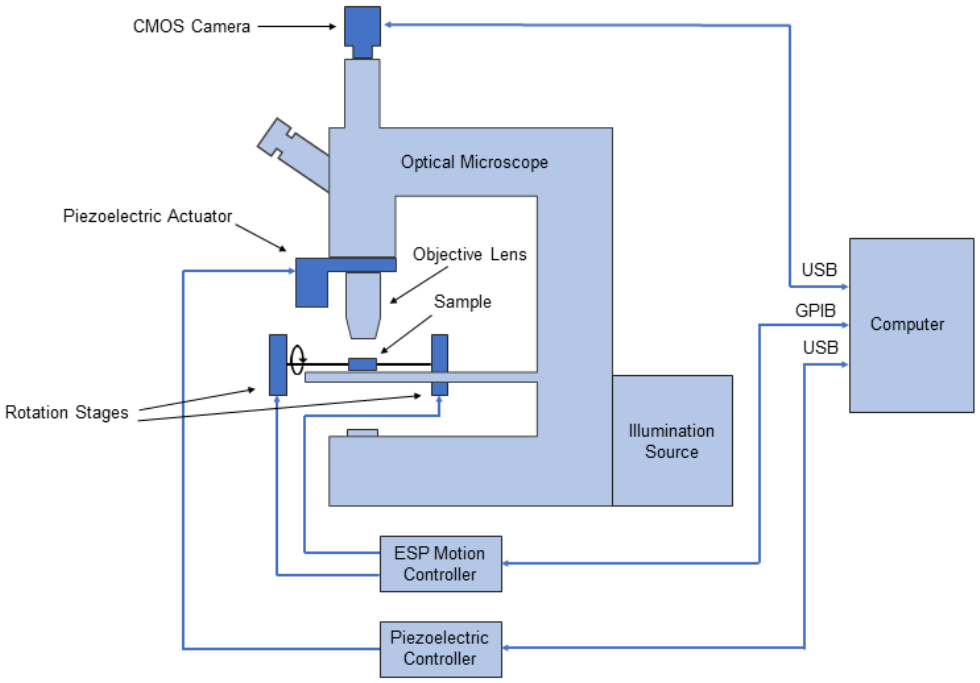

Figure A.1: Schematic diagram of the W417 QPI system.

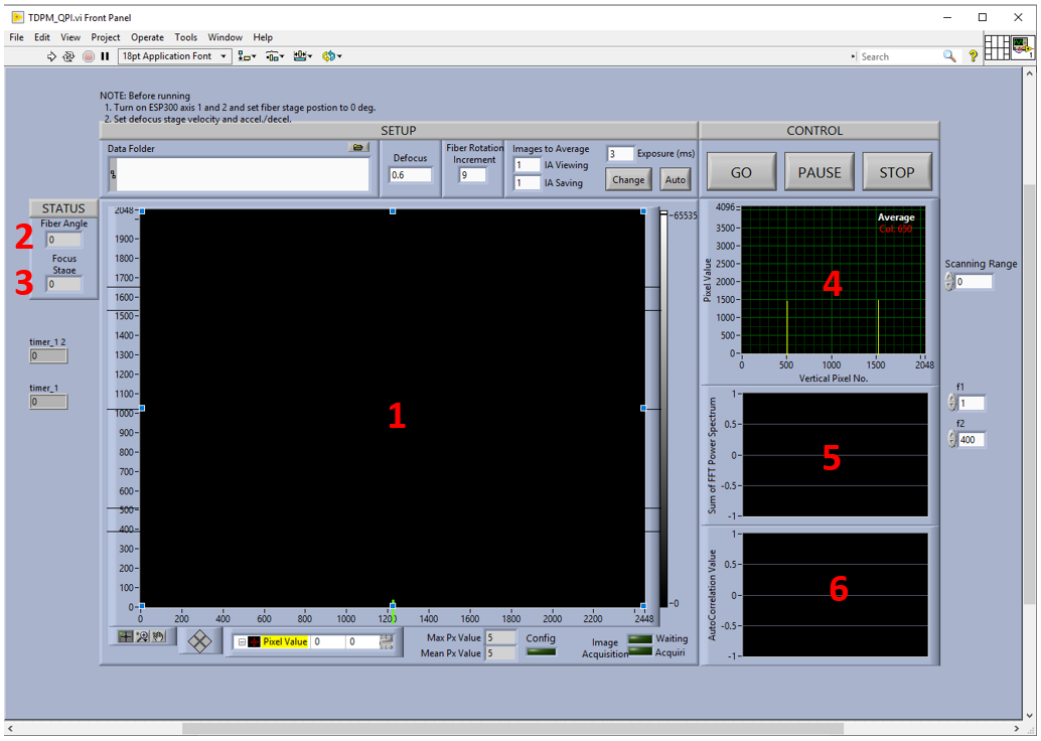

Figure A.2: Front panel interface of TDPM VI.

exposure.

A.2 Components of the W417 QPI System

1. **Olympus BX60 Microscope** (Printed copy of User Manual is kept in the lab)

    - Olympus Achromat 0.9 condenser with swing out lens and numerical aperture (NA) setting (disk illumination)
    - Olympus U-PCD2 phase contrast condenser (annular illumination).
        - http://www.olympus.com.cn/upload/accessory/20114/2011471445146256342.pdf
    - Olympus Mercury arc lamp
    - PI P725.4CD Objective Scanner
        - https://www.pi-usa.us/en/products/microscope-stages-bio-imaging-life-sciences/p-725-pifoc-objective-scanner-with-long-travel-range-200375/
    - PI E-709 Digital Piezo Controller
        - https://www.pi-usa.us/en/products/controllers-drivers-motion-control-software/piezo-drivers-controllers-power-supplies-high-voltage-amplifiers/e-709-compact-and-cost-optimized-digital-piezo-controller-605200/
    - Pixelink M5DM-CYL 5MP Monochrome Camera with USB3 Vision.
        - https://pixelink.com/products/microscopy/usb-30/23-sensors/m5d/
    - Newport ESP300 3-axis Motion Controller
        - https://www.newport.com/medias/sys_master/images/images/h2f/haa/8797091299358/ESP300-User-Manual.pdf
    - Newport SR50PP Motorized Rotation Stages.
        - https://www.newport.com/p/SR50PP
    - Dell Workstation

- Intel Core i7 8th Gen; 32 GB RAM.
- LabVIEW 2019
- MATLAB R2018b

A.3 Laboratory Procedures

A.3.1 Equipment Initialization

Olympus BX60 Microscope

1. Remove all plastic caps and covers from the microscope.

2. Turn on the mercury arc lamp and record the start time in the log book (Fig. A.3 and Fig. A.4).

   CAUTION: The lamp should be allowed to warm up and stabilize for at least one hour before any measurements are performed. This warm-up time can be used to prepare and align the fiber sample. The lamp should not be turned on if it will not remain on for at least one hour.

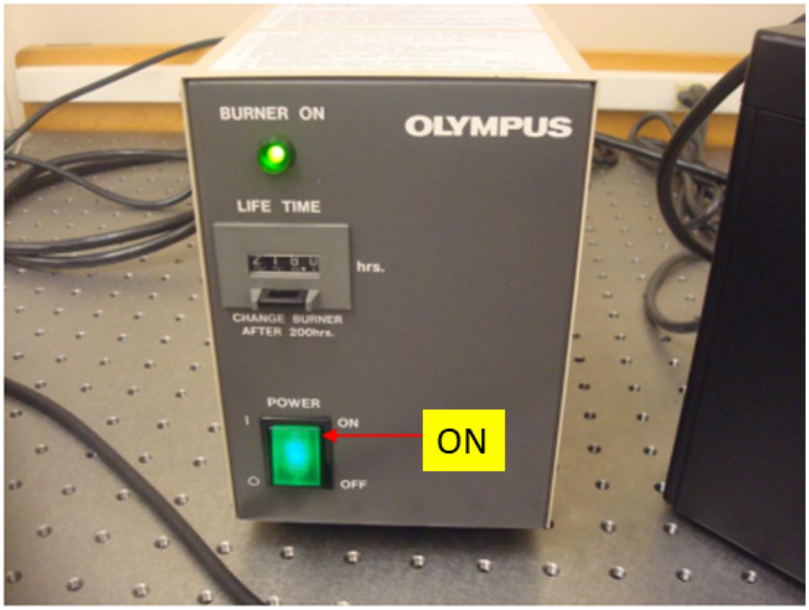

Figure A.3: Mercury arc lamp.

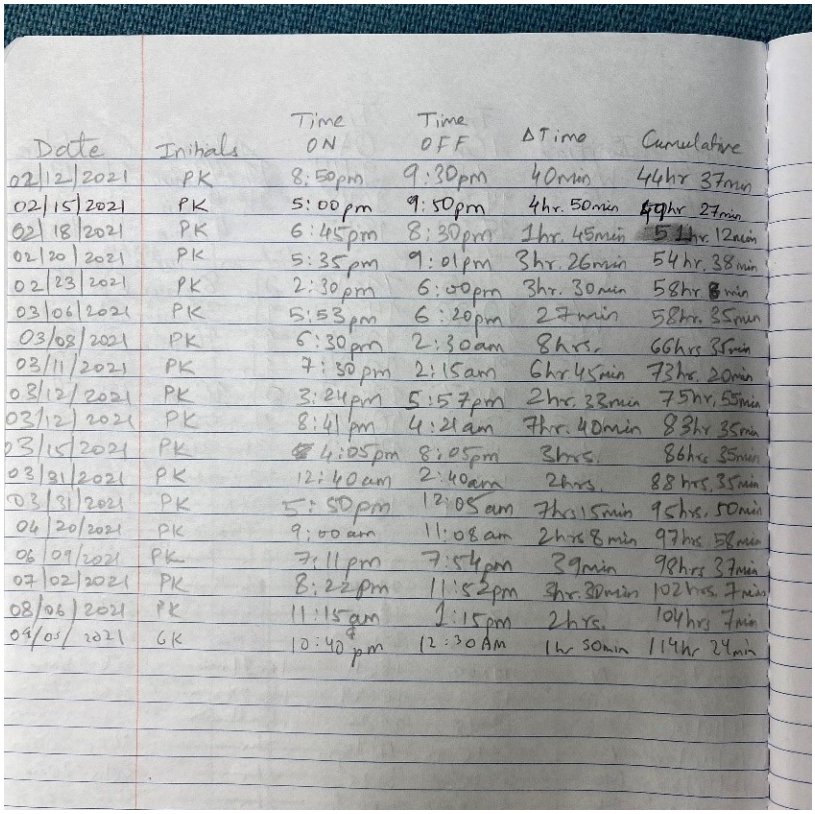

Date	Initials	Time ON	Time OFF	ΔTime	Cumulative
02/12/2021	PK	8:50pm	9:30pm	40min	44hr 37min
02/15/2021	PK	5:00pm	9:50pm	4hr. 50min	49hr 27min
02/18/2021	PK	6:45pm	8:30pm	1hr. 45min	51hr. 12min
02/20/2021	PK	5:35pm	9:01pm	3hr. 26min	54hr. 38min
02/23/2021	PK	2:30pm	6:00pm	3hr. 30min	58hr. 8min
03/06/2021	PK	5:53pm	6:20pm	27min	58hr. 35min
03/08/2021	PK	6:30pm	2:30am	8hrs.	66hrs. 35min
03/11/2021	PK	7:30pm	2:15am	6hr. 45min	73hr. 20min
03/12/2021	PK	3:24pm	5:57pm	2hr. 33min	75hr. 53min
03/12/2021	PK	8:41pm	4:21am	7hr. 40min	83hr. 33min
03/15/2021	PK	4:05pm	8:05pm	3hrs.	86hrs. 33min
03/31/2021	PK	12:40am	2:40am	2hrs.	88 hrs. 33min
03/31/2021	PK	5:50pm	12:05am	7hrs. 15min	95hrs. 50min
04/20/2021	PK	9:00am	11:08am	2hrs. 8min	97hrs. 58min
06/09/2021	PK	7:11pm	7:54pm	39min	98hrs. 37min
07/02/2021	PK	8:22pm	11:52pm	3hr. 30min	102hrs. 7min
08/06/2021	PK	11:15am	1:15pm	2hrs.	104hrs. 7min
09/05/2021	GK	10:40pm	12:30AM	1hr. 50min	114hr. 24min

Figure A.4: Log book to record the lamp use.

3. A slider on the side of the microscope can be used to set the beam splitter.

    - For viewing with eyepieces, push the slider all the way in.
    - For viewing with both the camera and the eyepieces, put the slider in the middle.
    - For viewing only with the camera, pull the slider all the way out. (This position is appropriate for capturing images).

4. Make sure the light is directed to the “transmitted” path (Fig. A.6).

5. There are three light intensity filters that can be used to adjust the intensity of illumination.

    - Light Balancing Daylight (LBD) filter makes the light bluer by reducing the warmer colors, making the light appear more like daylight illumination.

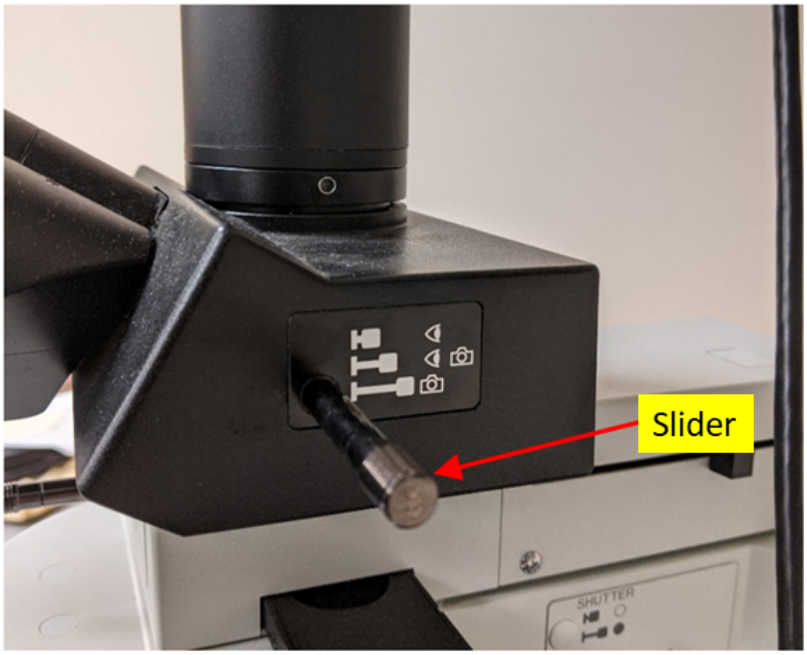

Figure A.5: Slider (showed by red arrow) to set the beam splitter.

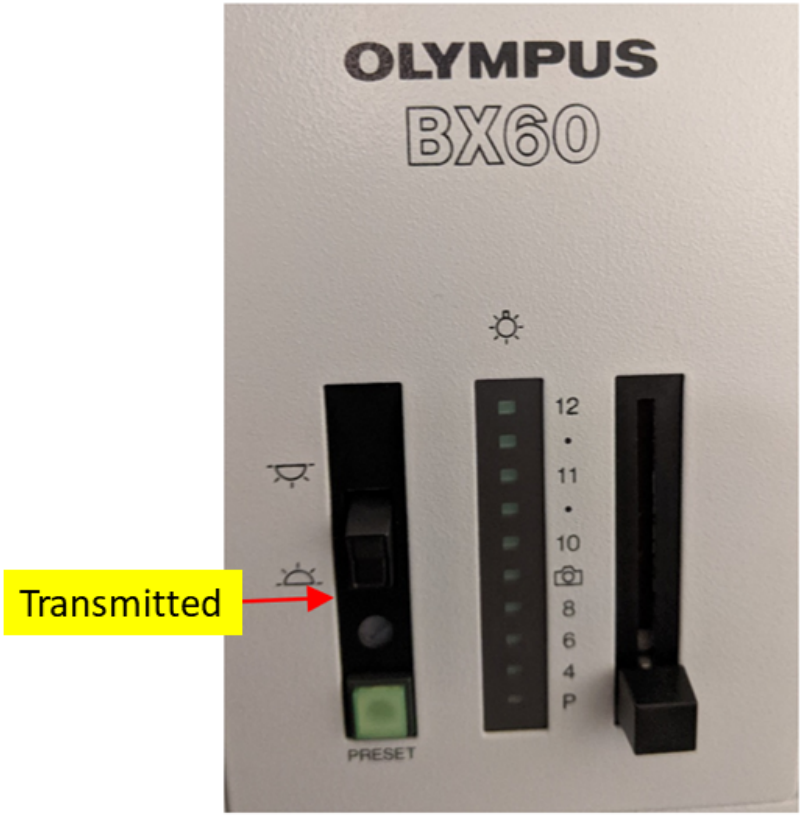

Figure A.6: Red arrow shows the location of the ”transmitted” setting.

- Neutral Density (ND) filters are used to balance the light intensity as required (Fig. A.7).
  - ND25 allows 25% transmittance.
  - ND6 allows 6% transmittance.
- For lower magnifications, all three filters can be added. As magnification is increased, filters can be removed as required (higher magnification objectives need higher light intensity).

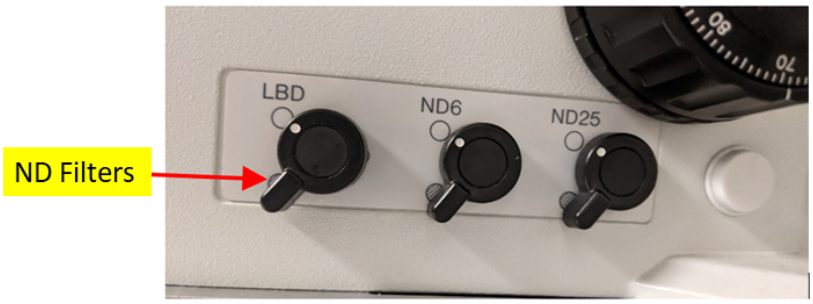

Figure A.7: Light intensity filters (to insert a filter, rotate the knob to bring the white dot to the position shown by red arrow).

Newport ESP300 Motion Controller and Camera

1. Turn on the ESP300 Motion controller.

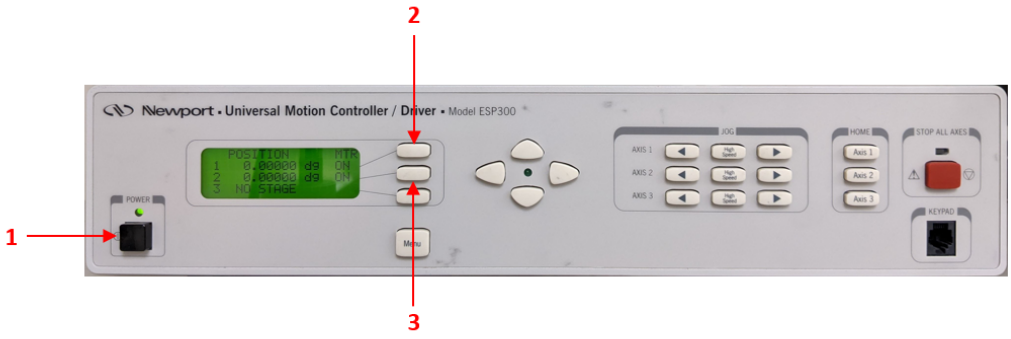

Figure A.8: ESP300 motion controller. (1) Power button on. (2) Axis 1 on. (3) Axis 2 on.

2. Turn on axis-1 and axis-2 (fiber rotation angle controller).

3. Make sure the camera is attached to the microscope and is connected to the computer via its USB cable.

4. Make sure the digital piezo controller (PI E-709) is connected to power and the computer (Fig. A.9).

Figure A.9: E-709 Piezo Controller. (1) Fiber optic connection to translator; (2) USB connection to computer; (3) Power connection to wall power supply.

A.3.2 **Koehler Illumination Setup**

1. Make sure the interference filter IF546 is placed on the lamp (allows only 546 nm wavelength). Since all our QPI experiments assume a quasi-monochromatic wavelength, having the filter in place is important.

2. Attach the 10x objective and rotate the turret to bring the objective in the light path.

3. Place the sample microscope slide (kept near the system) on the stage in the light path and make sure the swing-out lens of the condenser is in the light path (Fig. A.10).

4. Rotate the condenser height adjustment knob and move the condenser to the uppermost position (Fig. A.11).

5. Use the coarse and fine adjustment knobs to bring the slide in focus.

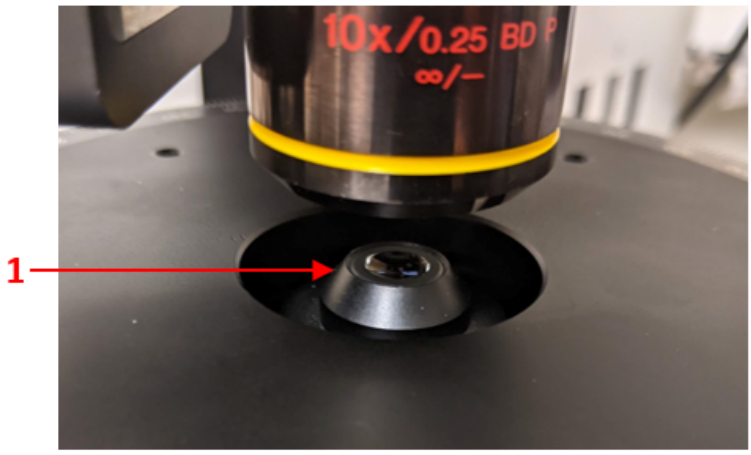

Figure A.10: Swing-out lens in the light path.

Figure A.11: Condenser height adjustment knob.

6. Rotate the field diaphragm to “closed” position, corresponding to minimum light (Fig. A.13).

7. Use the condenser height adjustment knob to adjust the condenser height such that the field diaphragm appears crisply focused when viewed through the microscope (Fig. A.14).

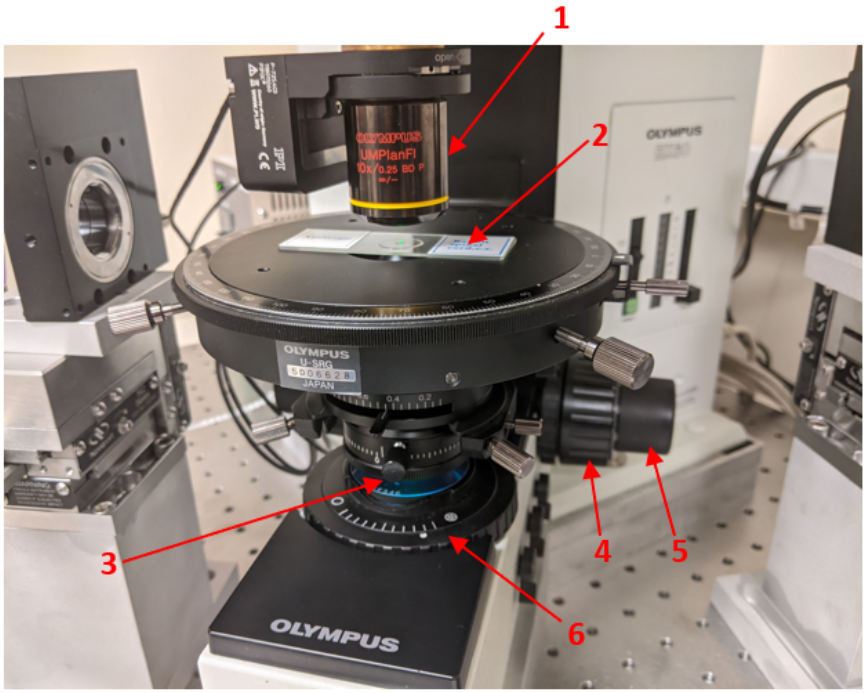

Figure A.12: (1) 10x objective; (2) sample slide; (3) IF546 interference filter; (4) Coarse adjustment knob; (5) Fine adjustment knob; (6) Field diaphragm.

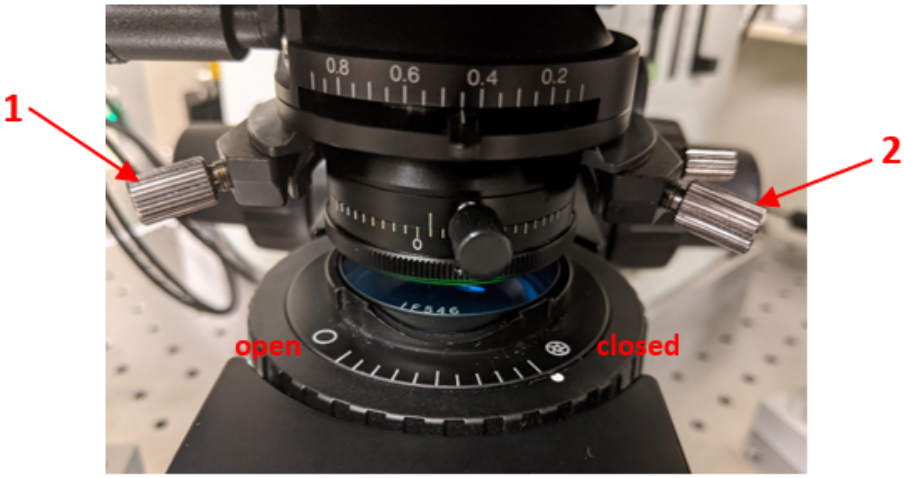

Figure A.13: Field diaphragm in the ”closed” position corresponding to minimum light. (1) & (2) condenser centering knobs.

8. Use the condenser centering knobs to center the view of the field diaphragm (Fig. A.15).

9. Rotate the field diaphragm towards the open position.

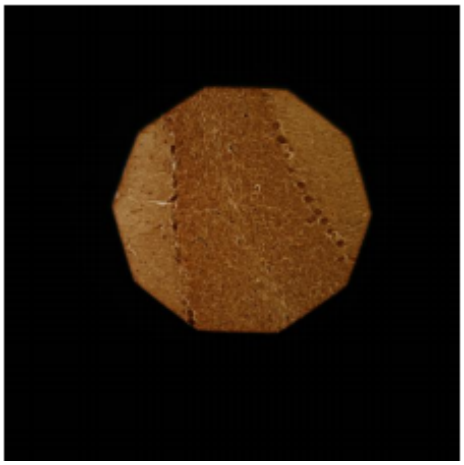

Figure A.14: Field diaphragm in crisp focus after adjusting the condenser height.

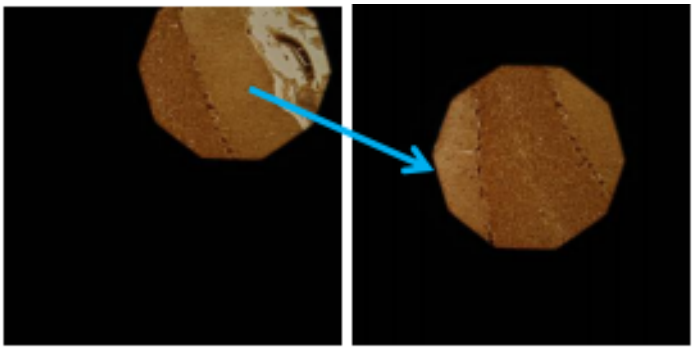

Figure A.15: Centering the field diaphragm using condenser centering knobs.

10. As the field diaphragm is opened and the view approaches the edge of the field of view, use the condenser centering knobs to fine tune the position of the light.

11. Once the light is optimally centered, open the light just beyond the field of view, not more (Fig. A.16).

12. Adjust the condenser aperture diaphragm to set the NA of the condenser to desired value. For good contrast, set the NA of the condenser at about 70-80% of NA of the objective.

13. Koehler Illumination is now established for this objective.

    CAUTION: Koehler Illumination is objective specific. Re-establish Koehler illumination for every objective.

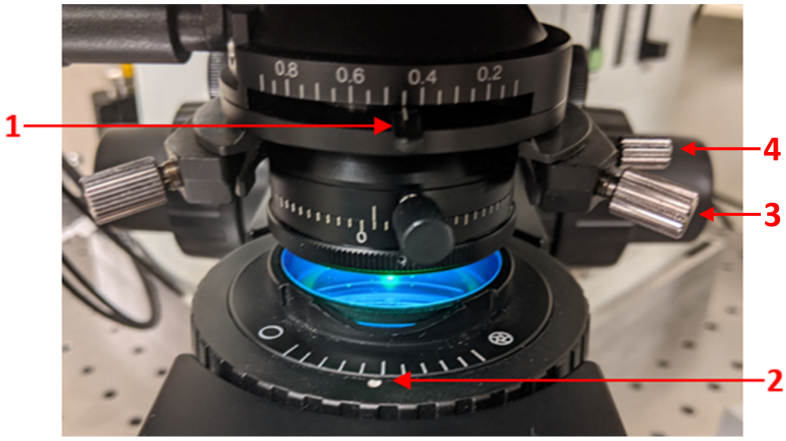

Figure A.16: (1) Condenser aperture diaphragm; (2) Opening the field diaphragm such that the illumination just exceeds the field of view; (3) Condenser centering knobs; (4) Condenser fastening/release screw.

A.3.3 **Removing the condenser**

1. Raise the sample stage and condenser as close to the objective lens as possible without hitting it with the coarse adjustment knob.

2. Loosen the condenser fastening/release screw.

3. Lower the condenser height with the condenser height knob just until it clears the sample stage, and the condenser can be removed.

4. Remove the condenser (Fig. A.17, Fig. A.17).

Using the U-PCD2 phase contrast condenser

NOTE: The U-PCD2 phase contrast condenser is used to do experiments requiring annular illumination.

1. Place the U-PCD2 condenser into the microscope and tighten the condenser fastening screw (Fig. A.19, Fig. A.20).

2. Set the microscope in Koehler illumination using the “0” setting on the turret.

3. Then, rotate the turret to bring the appropriate annulus in the light path.

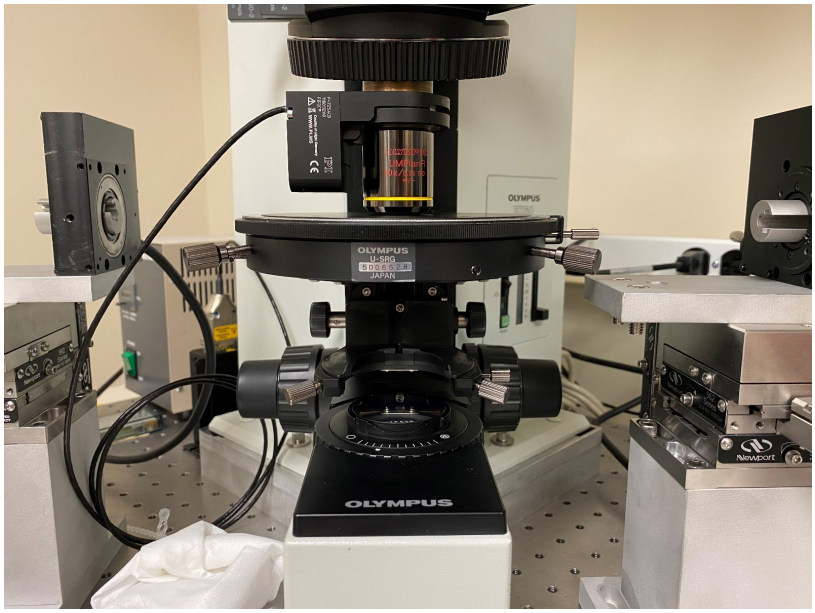

Figure A.17: Microscope without condenser.

Figure A.18: Condenser removed from microscope.

4. To center the annulus position, insert the “Bertrand Lens” slider which can be found on the body of the microscope (Fig. A.21).

5. View the annulus through the eyepiece and make sure the center of the annulus coincides with the center of the field of view. The annulus position can be adjusted using the two adjustment knobs on the U-PCD2 condenser.

Figure A.19: U-PCD2 Phase contrast condenser. (1) Annulus selector. (2) & (3) annulus centering knobs.

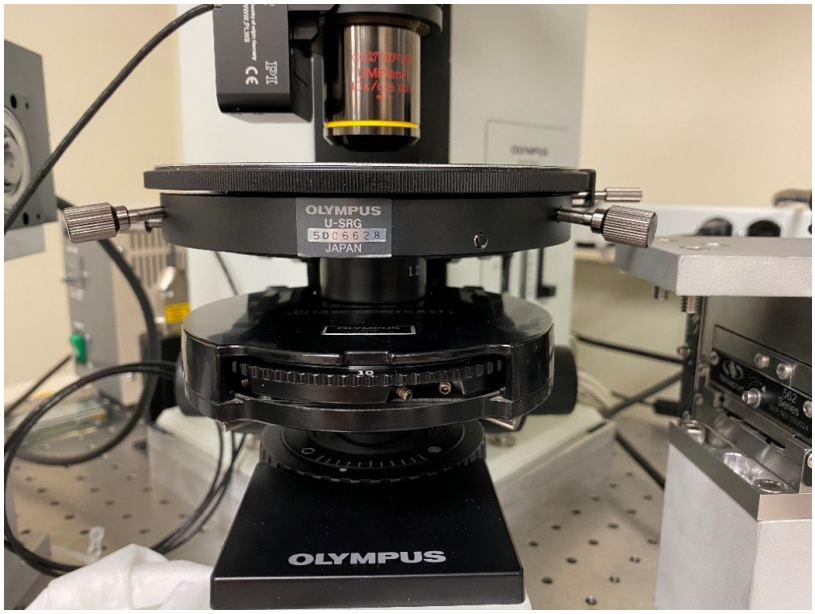

Figure A.20: U-PCD2 Phase contrast condenser in microscope.

6. Steps on how to attach the U-PCD2 condenser to the system are provided in the condenser manual, which is kept in the W417 lab near the microscope.

A.3.4 **Sample Preparation**

Prepare the Microscope Slide, Cover Slip Supporting Fibers, and New Fiber Sample:

Figure A.21: Bertrand lens selector knob. Pushed into the microscope Bertrand lens is selected, pulled out of the microscope the Bertrand lens is omitted.

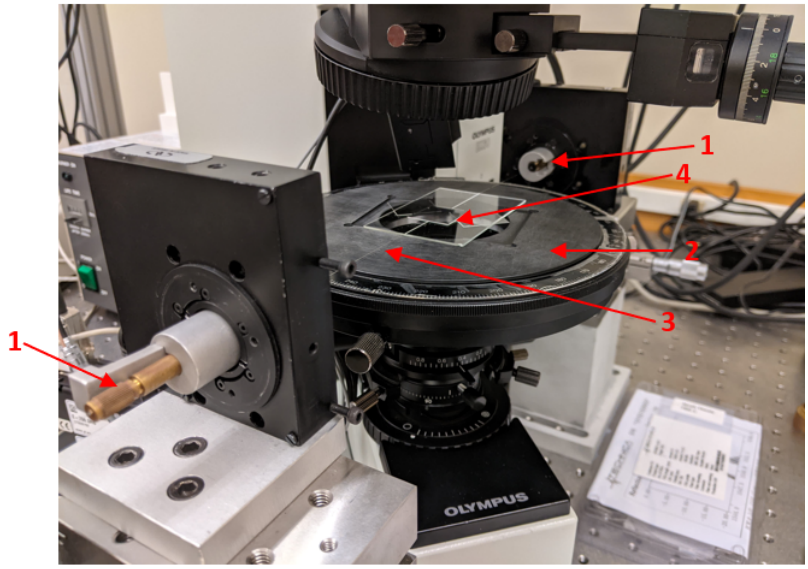

Figure A.22: Fiber rotation apparatus for QPI experiments. (1) Fiber rotation chuck; (2) stage plate; (3) Fiber; (4) cover slips.

1. Using a copious amount of KimWipes, clean the microscope slide and cover slip using 60% isopropyl alcohol (IPA) and a compressed gas duster (if available).

   Tip: wearing latex glove tips might be helpful in the process. The goal is for both slide and cover slip to be rid of any oily residue and dust, as these will perturb

the measurement.

2. From a fiber spool of interest, cut off about one foot of fiber using the fiber cutter.

3. Using standard fiber handling practices strip about one inch of fiber in the middle (Fig. A.23).

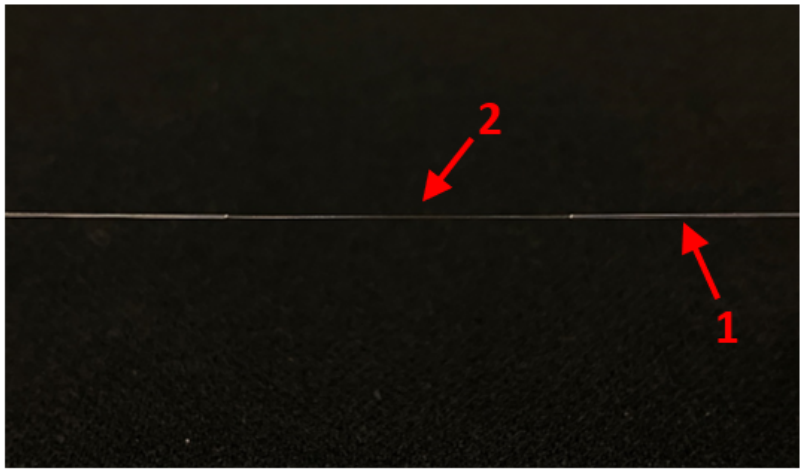

Figure A.23: – Closeup of fiber optic with 1" of core exposed in the middle; (1) fiber with coating; (2) fiber without coating.

4. Clean the microscope slide and place it on a KimWipe.

5. Pour a couple drops of oil in the middle of the slide and carefully place the stripped portion of the fiber in the middle of the slide (Fig. A.24).

6. Pour a few drops of index matching oil on the stripped portion of the fiber on the slide (Fig. A.24).

7. Take two clean cover slips and place them on both the sides of the fiber pointing towards each other (The two cover slips act as spacers for the third cover slip on top).

8. If the fiber is thicker than the thickness of the cover slip, more than one cover slip can be placed as a spacer on either side of the fiber.

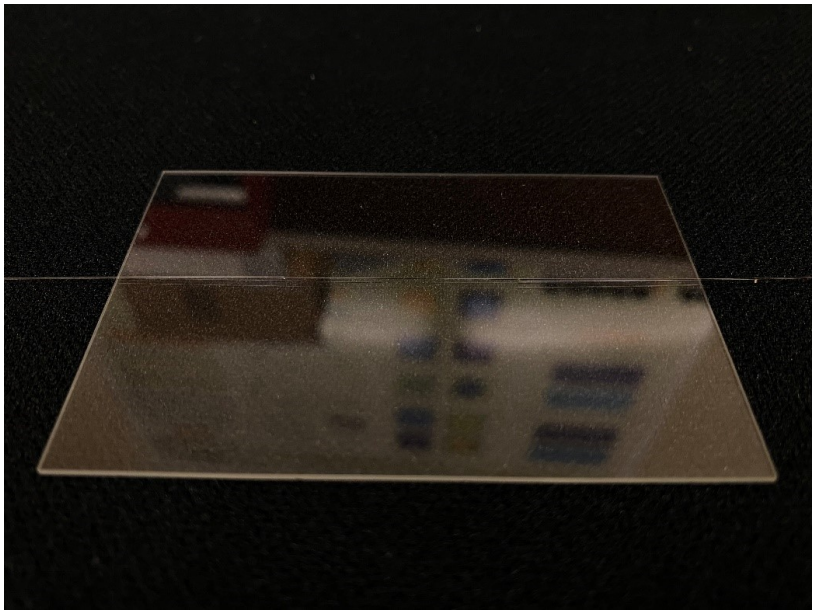

Figure A.24: Fiber on clean microscope slide.

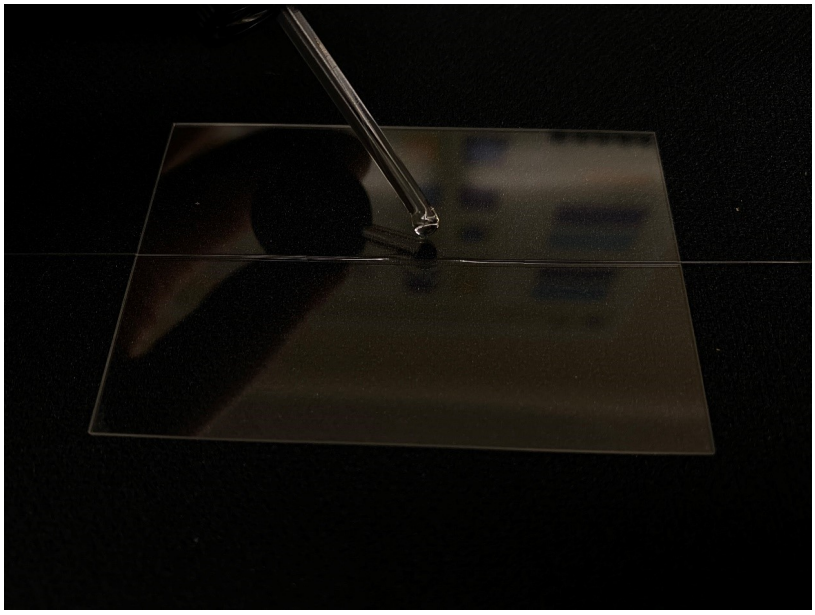

Figure A.25: Fiber with drop of refractive index matching oil being added.

9. Place one more cover slip on top of the two spacer cover slips covering the fiber sample.

10. Align the fiber rotation chucks perfectly with the stage and with each other.

11. Place the microscope slide with fiber on the stage plate.

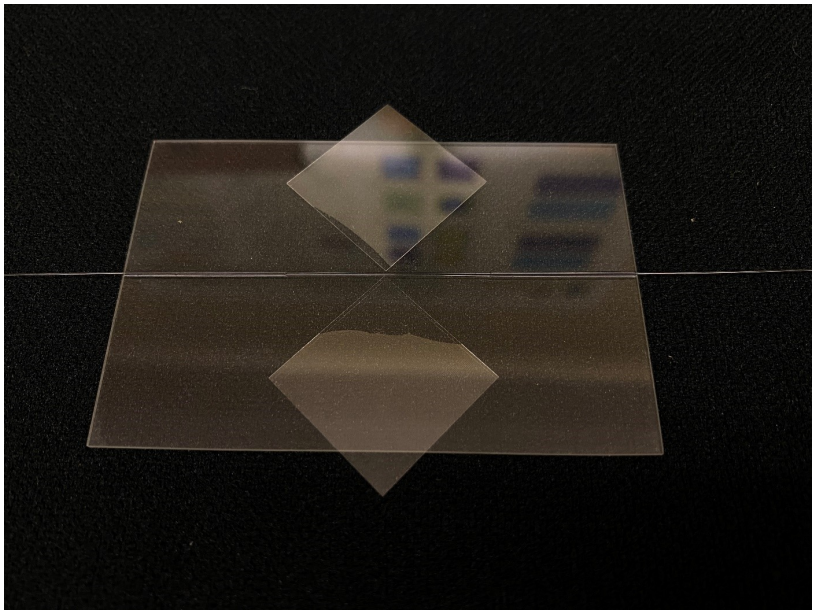

Figure A.26: Cover slips being used as spacers.

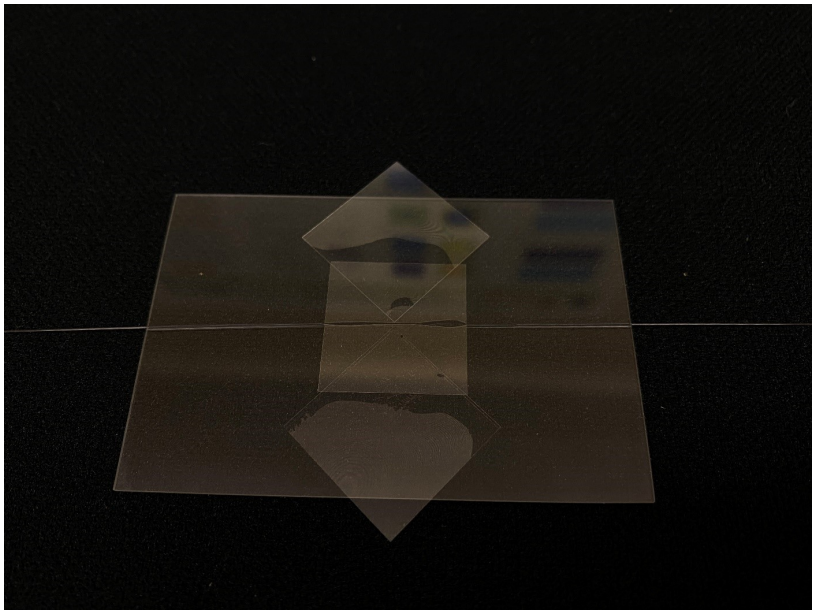

Figure A.27: Fiber on the slide and with a few drops of index matching oil, two cover slips as spacers, and a third cover slip on top of the two spacers, covering the fiber sample.

12. Carefully insert the fiber into the fiber rotation chucks on both sides.

13. The fiber should be straight and tight (but not overly tight) and make sure the two rotation chucks are aligned perfectly. Also make sure the elevation of the stage is in alignment with the height of the chucks.

14. Rotate the turret to bring the objective in the light path and get the fiber sample in focus (Fig. A.28)

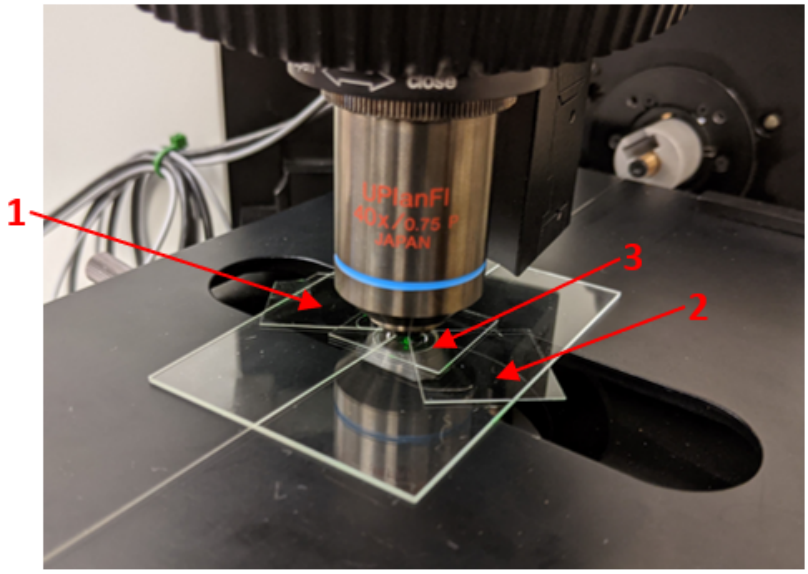

Figure A.28: (1) & (2) Cover slips placed on either side of the fiber to act as spacers. (3) Third cover slip placed on the two spacer slips covering the fiber. The fiber portion under observation is immersed in index matching oil.

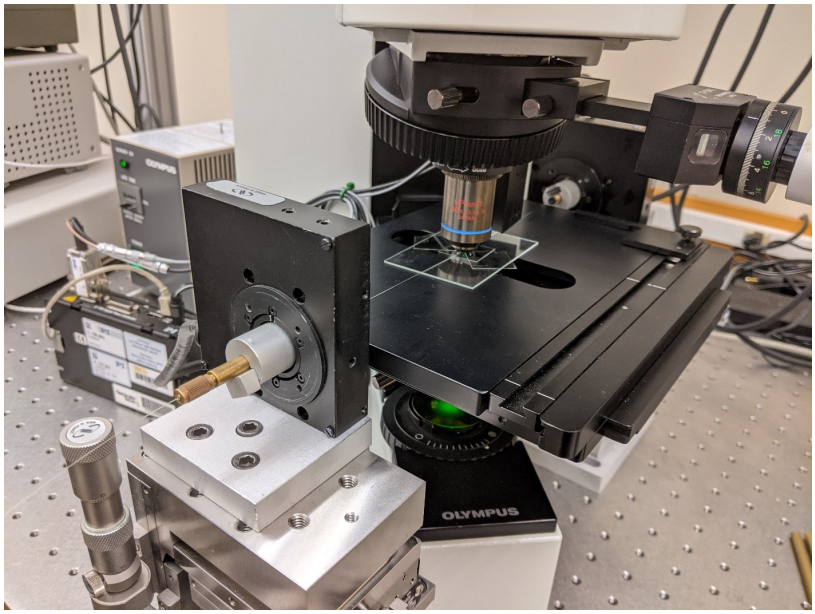

Figure A.29: Final configuration for taking QPI images of a fiber.

A.3.5 TDPM Experimentation

1. Open “TDPM_QPI.vi” from “Test VIs” folder on the Desktop.

2. On the front panel, press the “folder icon” to browse and select a destination folder to save the images.

3. Enter the desired defocus distance in the “defocus” entry in microns.

    - Alternatively, calculate the defocus distance using the formula dz = (0.461 um / RI_oil) where dz is the defocus distance and RI_oil is the refractive index of the oil. Enter the calculated dz value in the “defocus” entry.

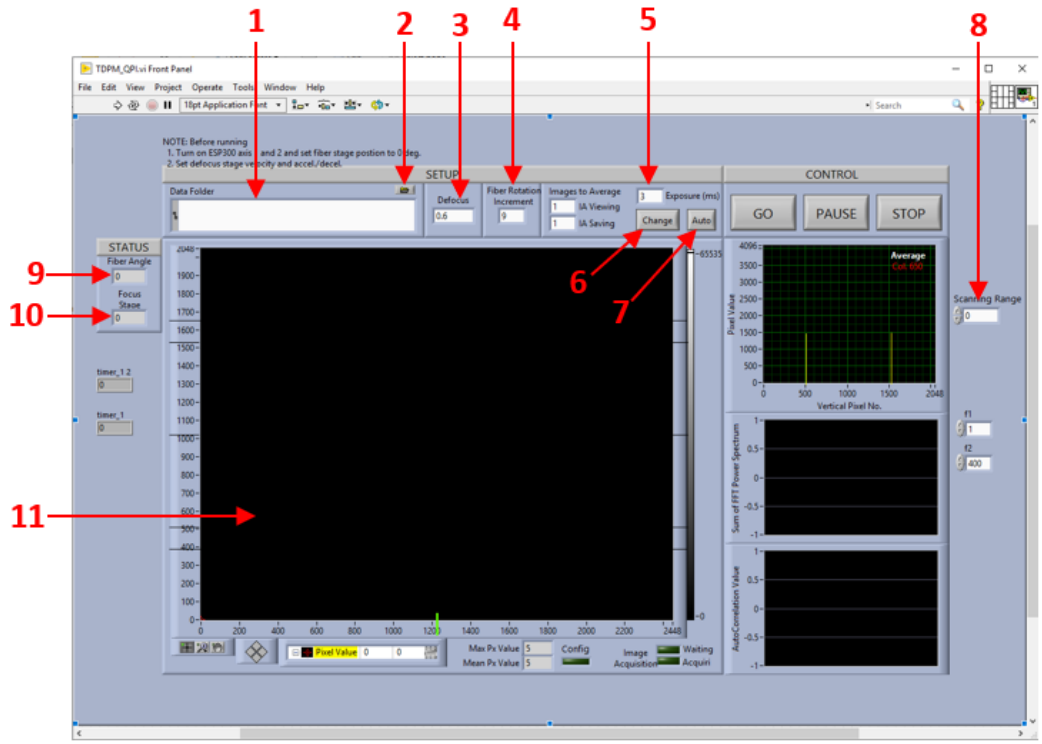

Figure A.30: (1) Destination folder address entry; (2) Press this folder icon to browse the destination folder location; (3) Defocus distance entry (microns); (4) Fiber rotation increment step size entry (deg); (5) Exposure time entry (ms); (6) Press change to apply the exposure value in the entry; (7) press Auto for setting the exposure automatically; (8) Scanning Range entry (microns); (9) Current rotation angle of the fiber; (10) relative Focus stage position (piezo scanner position) (microns); (11) Pixel graph showing the image from the camera..

4. On the right part of the panel, enter the “Scanning Range” in microns as desired.
    - This is the total distance the scanner will cover from start to finish.
    - For same number of images as with the 418 system, enter 100 (microns) as scanning range, and the same defocus distance as with the 418 system.
    - The maximum range of the 417 objective scanner is 400 (microns).
    - The number of images captured = floor(scanning range/defocus distance).
5. Bring the fiber core into focus and align it with the lines on the edge of the image view on the front panel.
6. Exposure settings can be changed manually or automatically from the front panel.
    - For manual change, enter the exposure (ms) value and press “change”.
    - For automatic change, press “Auto Exposure” button.
    - If the value in the entry did not updated after pressing “Auto Exposure” even though the exposure has changed, then press “change” once and again press the “Auto Exposure” button. Now the exposure value in the entry will be updated. (This value doesn’t really affect the experiment)
    - For good contrast and image quality, the “Mean Px Value” should be between 3500 to 4000.
7. Enter the fiber rotation increment angle (degrees) in the “Fiber Rotation Increment” entry. If this value is 12, then after the stack of images is captured, the fiber will be rotated by 12 degrees before the next stack is captured.
8. Make sure the fiber is in focus and clearly visible, the motion controller is ready, and the rotation stages are aligned. After everything is set, press the “GO” Button.
9. The piezo scanner will be configured (the “Config” light will come on) and then the image capture process will begin automatically.

10. The user can observe the motion of the piezo scanner via the “Focus Stage” entry.
    - The scanner will move from positive values to negative values.
    - Positive values correspond to the planes below the in-focus plane.
    - Negative values correspond to the planes above the in-focus plane.
11. After the stack of images for the angle is captured, the rotation stages will rotate the fiber by the specified increment angle. The rotated position of the stages is displayed in the “Fiber Angle” entry.
12. The program is paused automatically so that the user can re-align the fiber, if necessary.
13. Press the “GO” Button to continue the image capture process for the next stack of images.
14. Repeat steps 12 to 14 until the images have been captured for the “180 degree” angle displayed in the “Fiber Angle” entry.
15. Once the images have been captured for all the angles up to 180 degrees, then press the “STOP” button to stop the program.
16. The program can be paused or stopped during the process as required.
17. Copy the image folder to your desired location.

A.3.6 **MFPI-PC Experimentation**

1. MFPI-PC Experiments do not require rotation of the sample and hence motion controller and rotation stages are not used.
2. After setting the microscope for Koehler Illumination and preparing the 2D sample (phase masks or a slide), open “MFPIPC_QPI.vi” from the “Test Vis” folder on the Desktop.

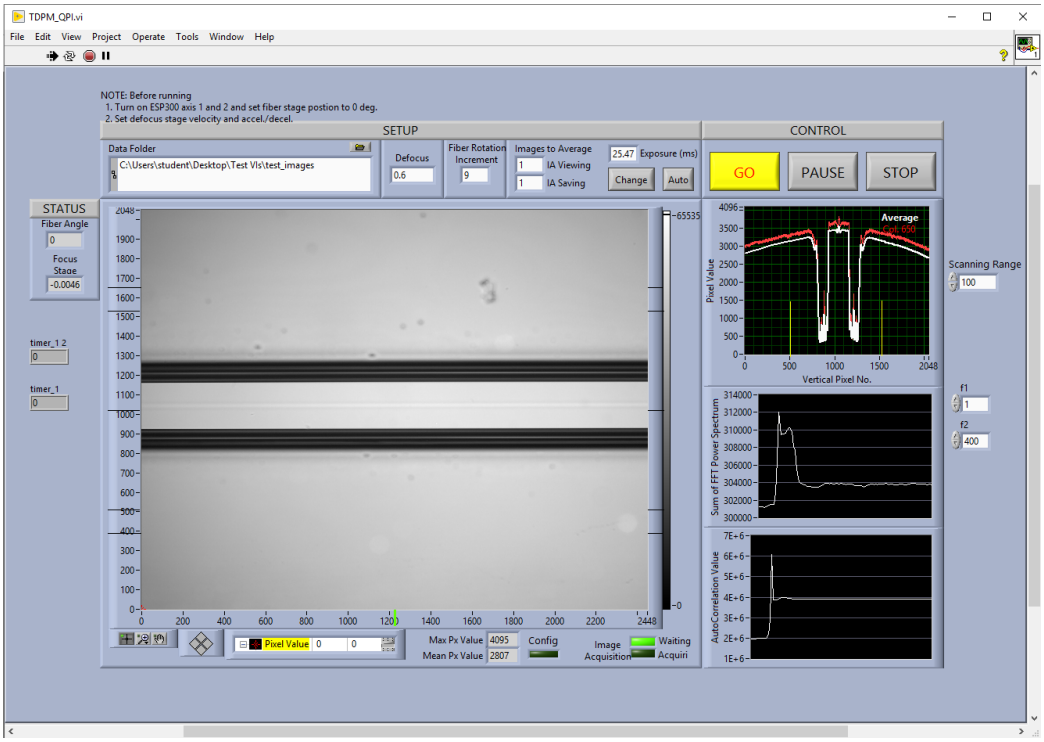

Figure A.31: Bringing the fiber core (running left to right) sample into focus.

3. Select the destination folder by pressing the “folder icon” and browsing to the desired folder location.

4. The slide/phase mask/thin sample is simply placed on the stage and brought into focus.

5. The Defocus distance value used for MFPI-PC is 0.6um and a total of 62 images are captured (31 above and below the in-focus plane).

    - The defocus distance and number of images need not be changed.
    - However, if some other value is desired, then defocus distance can be changed accordingly (The defocus distance calculation given in TDPM section is applicable only for TDPM).
    - Correspondingly, few changes need to be made in the MFPIPC_QPI block diagram (make a copy before making these changes) (Fig. A.32): -

(a) Press CTRL+E in the LabVIEW program or go to “Window” and select “Show Block Diagram”.

(b) Replace “-0.6” with the new defocus distance as a negative value (e.g. Enter “-0.5” if new defocus distance is 0.5um) (Fig. A.32).

(c) Replace the total loop count for defocusing loop (62 by default) with the new total number of images, as desired (Fig. A.32).

(d) Replace the “18” with new value calculated by floor(defocus distance*(total no. of images/2)) (Fig. A.33). For example, if the new defocus distance is 0.4um and the new total no. of images is 74, then the new value is floor(0.4*37) = 14.

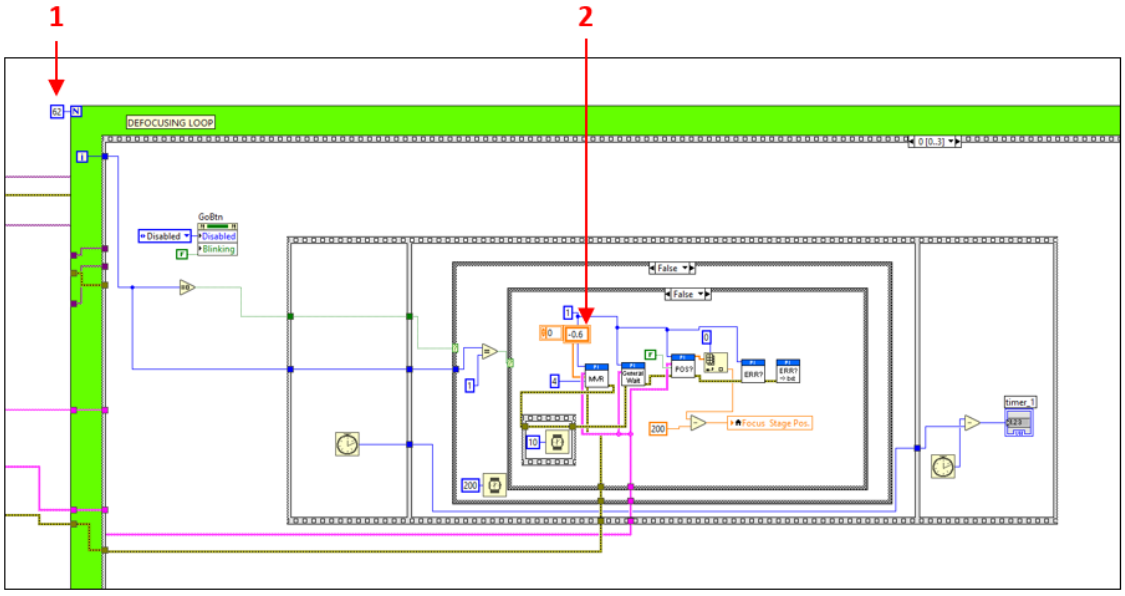

Figure A.32: (1) Total loop count (total number of images captured); (2) value corresponding to the defocus distance (this value should be the negative of the defocus distance). This part of the code is found in the “frame 0” (top red circle) and when the inner condition is “False” (bottom red oval). The arrows in the highlighted ovals allow the user to access the codes for different frames/cases.

6. After the microscope, the illumination, and the sample are set, press the “GO” button to start image acquisition.

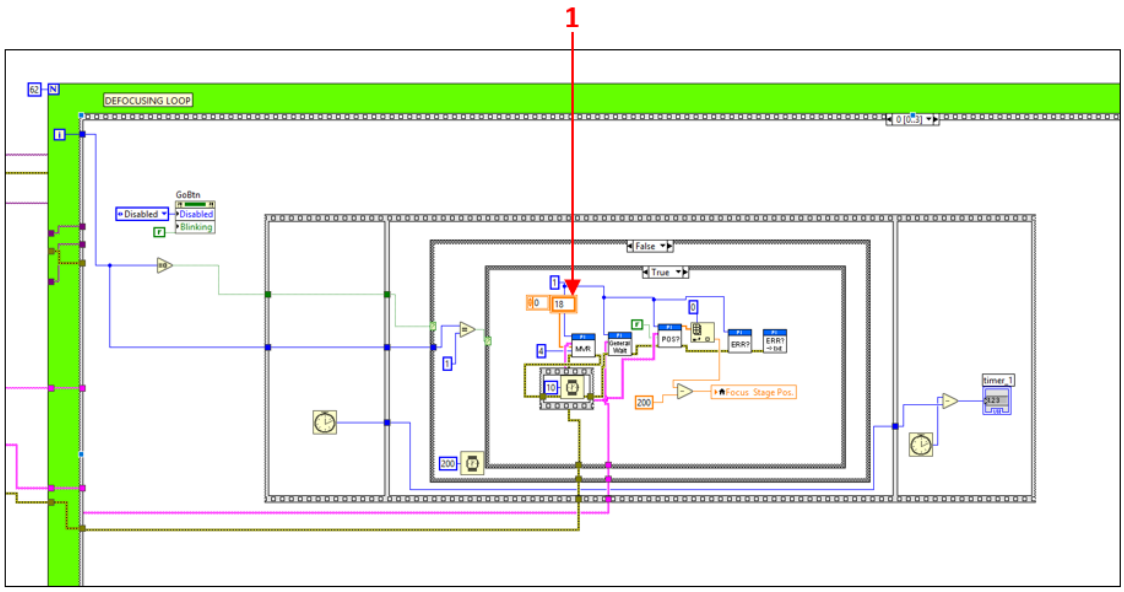

Figure A.33: (1) The value to be changed for step (d). This is the value corresponding to the lowest plane below the in-focus plane. This part of the code is found on the "frame 0" (top red oval) and when the inner case is "True" (bottom red oval).

7. The piezo scanner will move from positive to negative values and the program will automatically stop after the process is complete. Only one stack of images is captured for 2D QPI.

8. Copy the destination folder containing the images to desired drive/location, if required.

A.3.7 **Remove the fiber from the fiber rotation chucks**

These steps should be followed for removing the fiber sample from the system and cleaning the system after use.

1. Loosen the fiber rotation chucks in the fiber rotation apparatus to free the sample.

2. Carefully remove the fiber from fiber rotation apparatus by pulling it towards the microscope and the stage plate through the fiber rotation chucks.

3. Be careful with pulling out the fiber from the chucks to avoid disturbing the cover

slips or the fiber beneath the cover slips.

A.3.8 **Remove the old sample from the custom stage plate.**

1. Remove the cover slip from the microscope slide and place it on a KimWipe.

   TIP: There is an attractive force between the cover slip and the microscope slide due to the index matching oil. Carefully slide the cover slip along the slide until it can easily break free.

   TIP: When removing a fiber sample from the fiber chuck, do not pull the measured region of the fiber through the chuck. This avoids contaminating the inside of the chuck with oil.

2. Remove the fiber from the microscope slide using tweezers and place it on a separate KimWipe.

3. Remove the microscope slide from the stage plate using tweezers and place it on another KimWipe.

4. The used slides should be cleaned with IPA and placed back in their box. The box with microscope slides can be found in the drawers of the red shelf near the microscope in W418 lab.

5. The fiber can be saved for later use, if needed, otherwise, it should be discarded in a glass recycle bin.

6. A small box of used cover slips is present in the W418 lab. It should be used to discard the used cover slips. Eventually, it should go in the glass recycle bin.

A.3.9 **Equipment Shutdown**

1. Rotate the microscope objective turret to remove the objective lens from the light path.

2. Carefully remove the fiber from the fiber rotation chucks on both sides.

3. Lower the stage plate using coarse adjustment knobs.

4. Carefully pick up the slide containing fiber sample and cover slips and keep it aside on a KimWipe.

5. Switch off the Motion controller, if it is on.

6. Turn off the lamp and note down the time in the log book.

7. Unplug the camera from the computer.

8. As a safety precaution, unplug the digital piezo controller.

9. The shutdown is now complete.

APPENDIX B

INFORMATION ON PHASE MASKS

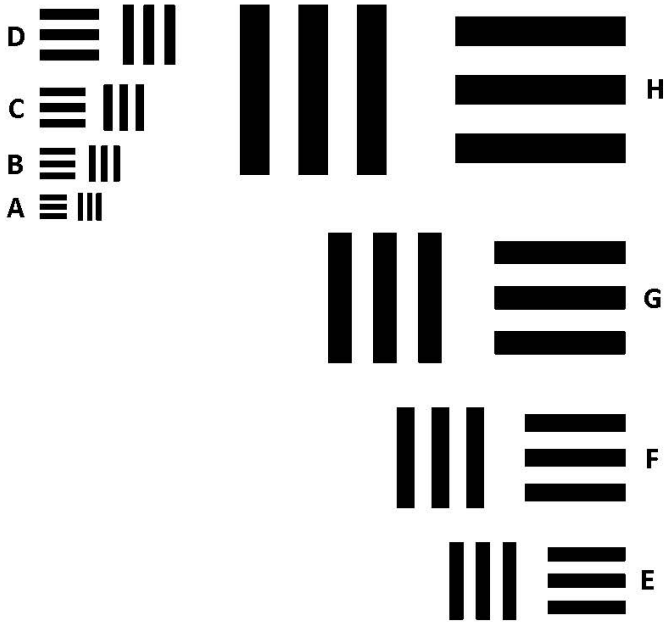

	Center-to-Center Spacing (µm)	Bar Width (µm)	Bar Length (µm)
A	1.0000	0.5000	2.8889
B	1.3000	0.6500	3.7556
C	1.6900	0.8450	4.8822
D	2.1970	1.0985	6.3469
E	2.8562	1.4281	8.2510
F	3.7128	1.8564	10.7262
G	4.8268	2.4134	13.9441
H	6.2748	3.1374	18.1273

Figure B.1: Dimensions of the resolution test chart patterns on the phase masks.

sample name	material	recipe	etch rate (Ang/sec)	Cr etch rate (Ang/sec)	selectivity	depth etched (Ang)	std. dev. (Ang)	etch time (sec)
paco_robles	Esco fused quartz	DKBOXH2	44	2.5	17.6	974	17	22
gaylord01	S1-UV grade fused silica Esco Optics Q112040	DKBOXH24	27	~0	infinity	748	18	27
gaylord02	S1-UV grade fused silica Esco Optics Q112040	DKBOXH24	28	~0	infinity	1790	30	64
vwr slide 1	Fisherbrand Plain Microscope Slide 12-550D, soda lime	DKBOXH24	2.3	0.41	5.6	270	19	116
samples ~25x25 or 30x30 mm mounted on 4" silicon wafer with cool grease								
PT ICP recipe	RF1 (W)	RF2 (W)	CF4 (sccm)	C4F8 (sccm)	H2 (sccm)	P (mTorr)	DC (V)	
DKBOXH2	100	800	20	15	15	5		
DKBOXH24	40	800	20	15	15	5	160	

Figure B.2: Summary of the EBL etch data of G01 and G02 phase masks.

REFERENCES

[1] J. W. Lichtman and J.-A. Conchello, "Fluorescence microscopy," *Nat. Methods*, vol. 2, no. 12, pp. 910–919, Dec. 1, 2005.

[2] Z. Xuepeng, Z. Xuguang, J. Feng, Z. Zheng Gang, M. Katakowski, and M. Chopp, "Dual-color fluorescence imaging in a nude mouse orthotopic glioma model," *J. Neurosci. Meth.*, vol. 181, no. 2, pp. 178–85, Jul. 30, 2009.

[3] G. Lukinaviius, G. Y. Mitronova, S. Schnorrenberg, A. N. Butkevich, H. Barthel, V. N. Belov, and S. W. Hell, "Fluorescent dyes and probes for super-resolution microscopy of microtubules and tracheoles in living cells and tissues," *Chem. Sci.*, vol. 9, no. 13, pp. 3324–3334, Feb. 26, 2018.

[4] M. V. Sednev, V. N. Belov, and S. W. Hell, "Fluorescent dyes with large Stokes shifts for super-resolution optical microscopy of biological objects: A review," *Methods Appl. Flouresc.*, vol. 3, no. 4, p. 042004 (28 pp.) Oct. 22, 2015.

[5] D. Hara, Y. Okamoto, S. Fujiyama, Y. Nishikawa, Y. Norimine, Y. Kazuta, T. Motoki, H. Amino, and S. Iwanaga, "An orange-fluorescent dye with long-lasting blinking for single molecule localization microscopy," *Proc. SPIE*, vol. 11256, p. 112560G (6 pp.) 2020.

[6] G. Patterson, M. Davidson, S. Manley, and J. Lippincott-Schwartz, "Superresolution imaging using single-molecule localization," *Ann. Rev. Phys. Chem.*, vol. 61, no. 1, pp. 345–367, Mar. 1, 2010.

[7] A. Egner and S. W. Hell, "Fluorescence microscopy with super-resolved optical sections," *Trends Cell Biol.*, vol. 15, no. 4, pp. 207–215, Apr. 2005.

[8] S. W. Hell, "Far-field optical nanoscopy," *Sci.*, vol. 316, no. 5828, p. 1153 (7 pp.) May 25, 2007.

[9] R. Dixit and R. Cyr, "Cell damage and reactive oxygen species production induced by fluorescence microscopy: Effect on mitosis and guidelines for non-invasive fluorescence microscopy," *Plant J*, vol. 36, no. 2, pp. 280–290, Sep. 15, 2003.

[10] J. W. Dobrucki, D. Feret, and A. Noatynska, "Scattering of exciting light by live cells in fluorescence confocal imaging: Phototoxic effects and relevance for FRAP studies," *Biophys. J.*, vol. 93, no. 5, pp. 1778–1786, Sep. 1, 2007.

[11] K. L. Tosheva, Y. Yue, P. M. Pereira, S. Culley, and R. Henriques, "Between life and death: Strategies to reduce phototoxicity in super-resolution microscopy," *J. Phys. D Appl. Phys.*, vol. 53, no. 16, p. 163001 (14 pp.) Apr. 2020.

[12] F. Zernike, "Phase contrast, a new method for the microscopic observation of transparent objects. Part I," *Physica Scripta*, vol. 9, pp. 686–698, Jul. 1942.

[13] F. Zernike, "Phase contrast, a new method for the microscopic observation of transparent objects Part II," *Physica Scripta*, vol. 9, no. 10, pp. 974–986, Dec. 1942.

[14] G. Nomarski and A. R. Weill, "Application à la métallographie des méthodes interférentielles à deux ondes polarisées," *Rev. Met. Paris*, vol. 52, no. 2, pp. 121–134, Feb. 1955.

[15] W. Lang, "Nomarski differential interference-contrast microscopy," *Zeiss Info. 70*, pp. 114–120, 1968.

[16] M. Pluta, "Nomarski's DIC microscopy: A review," *Proc. SPIE*, vol. 1846, pp. 10–25, May 3, 1994.

[17] R. Rottenfusser, E. Wilson, and M. Davidson, "Enhancing contrast in optical microscopy," *http://zeiss-campus.magnet.fsu.edu/articles/basics/contrast.html*,

[18] T. Cacace, V. Bianco, and P. Ferraro, "Quantitative phase imaging trends in biomedical applications," *Opt. Laser Eng.*, vol. 135, p. 106188 (9 pp.) Dec. 2020.

[19] B. Kemper, M. Gotte, B. Greve, and S. Ketelhut, "Prospects and challenges of quantitative phase imaging in tumor cell biology," *Proc. SPIE*, vol. 9718, p. 97180N (7 pp.) Mar. 9, 2016.

[20] C. Allier, L. Herve, O. Mandula, P. Blandin, Y. Usson, J. Savatier, S. Monneret, and S. Morales, "Quantitative phase imaging of adherent mammalian cells: A comparative study," *Biomed. Opt. Express*, vol. 10, no. 6, pp. 2768–2783, Jun. 1, 2019.

[21] S. Aknoun, J. Savatier, P. Bon, F. Galland, L. Abdeladim, B. Wattellier, and S. Monneret, "Living cell dry mass measurement using quantitative phase imaging with quadriwave lateral shearing interferometry: An accuracy and sensitivity discussion," *J. Biomed. Opt*, vol. 20, no. 12, p. 126009 (15pp.) Dec. 22, 2015.

[22] A. T. Y. Mok, K. C. M. Lee, K. K. Y. Wong, and K. K. Tsia, "Label-free cell-cycle analysis by high-throughput quantitative phase time-stretch imaging flow cytometry," *Proc. SPIE*, vol. 10505, 105050J (5 pp.) Feb. 2018.

[23] F. Hideki and A. Yoshihisa, "Three-dimensional quantitative phase imaging of blood coagulation structures by optical projection tomography in flow cytometry using digital holographic microscopy," *J. Biomed. Opt.*, vol. 24, no. 3, pp. 1–6, Oct. 9, 2018.

[24] I. Moon, F. Yi, Y. H. Lee, B. Javidi, D. Boss, and P. Marquet, "Automated quantitative analysis of 3D morphology and mean corpuscular hemoglobin in human red blood cells stored in different periods," *Opt. Express*, vol. 21, no. 25, pp. 30 947–30 957, Dec. 16, 2013.

[25] P. Wang, R. Bista, R. Bhargava, R. E. Brand, and Y. Liu, "Spatial-domain low-coherence quantitative phase microscopy for cancer diagnosis," *Proc. SPIE*, vol. 7889, p. 78891Q (3 pp.) 2011.

[26] Z. Wang, K. Tangella, A. Balla, and G. Popescu, "Tissue refractive index as marker of disease," *J. Biomed. Opt.*, vol. 16, no. 11, pp. 116017-1–116017-7, Nov. 2011.

[27] V. Ayyappan, A. Chang, C. Zhang, S. K. Paidi, R. Bordett, T. Liang, I. Barman, and R. Pandey, "Identification and staging of B-cell acute lymphoblastic leukemia using quantitative phase imaging and machine learning," *ACS Sens.*, vol. 5, no. 10, pp. 3281–3289, Oct. 2020.

[28] G. M. Noah, Y. Bao, and T. K. Gaylord, "Characterization of fiber Bragg gratings using a 3D quantitative phase imaging approach," in *OSA Frontiers in Opt.*, 2020, p. JW3A.63 (2 pp.)

[29] G. S. D. Gordon, J. Joseph, M. P. Alcolea, T. Sawyer, C. Williams, C. R. M. Fitzpatrick, P. H. Jones, M. di Pietro, and R. C. Fitzgerald, "Quantitative phase and polarization imaging through an optical fiber applied to detection of early esophageal tumorigenesis," *J. Biomed. Opt*, vol. 24, no. 12, p. 126004 (13 pp.) Dec. 16, 2019.

[30] V. K. Lam, T. Nguyen, V. Bui, B. M. Chung, L.-C. Chang, G. Nehmetallah, and C. B. Raub, "Quantitative scoring of epithelial and mesenchymal qualities of cancer cells using machine learning and quantitative phase imaging," *J. Biomed. Opt*, vol. 25, no. 2, p. 026002 (17 pp.) Feb. 18, 2020.

[31] H. Majeed, M. E. Kandel, K. Han, Z. Luo, V. Macias, K. Tangella, A. Balla, and G. Popescu, "Diagnosis of breast cancer biopsies using quantitative phase imaging," *Proc. SPIE*, vol. 9336, p. 93361R (6 pp.) Feb. 2015.

[32] Y. Tian, C. Runyu, X. Wen, P. Feng, and L. Xiaoping, "An optical study of drug resistance detection in endometrial cancer cells by dynamic and quantitative phase imaging," *J. Biophotonics*, vol. 12, no. 7, p. e201800443 (9 pp.) Jul. 2019.

[33] L. Kastl, M. Isbach, D. Dirksen, J. Schnekenburger, and B. Kemper, "Quantitative phase imaging for cell culture quality control," *Cytometry A*, vol. 91, no. 5, pp. 470–481, May 2017.

[34] Z. El-Schich, A. L. Mölder, and A. G. Wingren, "Quantitative phase imaging for label-free analysis of cancer cells—focus on digital holographic microscopy," *Appl. Sci.*, vol. 8, no. 7, p. 1027 (16 pp.) Jun. 23, 2018.

[35] L. Kastl, B. Kemper, and J. Schnekenburger, "Quantitative phase imaging for enhanced assessment of optomechanical cancer cell properties," *Proc. SPIE*, vol. 10503, p. 105032R (6 pp.) Feb. 23, 2018.

[36] Y. Li, J. Di, W. Wu, P. Shang, and J. Zhao, "Quantitative investigation on morphology and intracellular transport dynamics of migrating cells," *Appl. Opt.*, vol. 58, no. 34, G162–G168, Dec. 1, 2019.

[37] B. Rappaz, P. Marquet, E. Cuche, Y. Emery, C. Depeursinge, and P. J. Magistretti, "Measurement of the integral refractive index and dynamic cell morphometry of living cells with digital holographic microscopy," *Opt. Express*, vol. 13, no. 23, pp. 9361–9373, Nov. 14, 2005.

[38] J. Jung, L. E. Matemba, K. Lee, P. E. Kazyoba, J. Yoon, J. J. Massaga, K. Kim, D.-J. Kim, and Y. Park, "Optical characterization of red blood cells from individuals with sickle cell trait and disease in Tanzania using quantitative phase imaging," *Sci. Rep.*, vol. 6, no. 1, p. 31698 (9 pp.) Aug. 22, 2016.

[39] L. Chengshuai, C. Shichao, M. Klemba, and Z. Yizheng, "Integrated quantitative phase and birefringence microscopy for imaging malaria-infected red blood cells," *J. Biomed. Opt*, vol. 21, no. 9, p. 090501 (4 pp.) Sep. 6, 2016.

[40] S. Y. Lee and Y. K. Park, "3-D quantitative measurements of individual human red blood cells from diabetic patients employing 3-D quantitative phase imaging," in *ACPC*, ser. Optics InfoBase Conference Papers, OSA - The Optical Society.

[41] M. Schurmann, J. Scholze, P. Muller, J. Guck, and C. J. Chan, "Cell nuclei have lower refractive index and mass density than cytoplasm," *J. Biophotonics*, pp. 1068–1076, Mar. 24, 2016.

[42] J. Y. Park, H. Desta, M. C. Maloney, A. Sharikova, and A. Khmaladze, "Digital holographic phase imaging of particles embedded in microscopic structures in three dimensions," *Proc. SPIE*, vol. 9870, p. 98700B (9 pp.) Apr. 2016.

[43] A. Ghosh, J. Noble, A. Sebastian, S. Das, and Z. Liu, "Digital holography for non-invasive quantitative imaging of two-dimensional materials," *J. Appl. Phys.*, vol. 127, no. 8, p. 084901 (10 pp.) Feb. 24, 2020.

[44] R. Zhou, C. Edwards, G. Popescu, and L. Goddard, "Semiconductor defect metrology using laser-based quantitative phase imaging," *Proc. SPIE*, vol. 9336, p. 93361I (6 pp.) Feb. 2015.

[45] W. Qu, Y. Wen, Z. Wang, F. Yang, L. Huang, and C. Zuo, "Quantitative phase measurement for wafer-level optics," *Proc. SPIE*, vol. 9524, p. 95242J (13 pp.) Jul. 17, 2015.

[46] M. R. McCartney, N. Agarwal, S. Chung, D. A. Cullen, M.-G. Han, K. He, L. Li, H. Wang, L. Zhou, and D. J. Smith, "Quantitative phase imaging of nanoscale electrostatic and magnetic fields using off-axis electron holography," *Ultramicroscopy*, vol. 110, no. 5, pp. 375–382, Apr. 1, 2010.

[47] M. H. Jenkins, "New quantitative phase imaging modalities on standard microscope platforms," Ph.D. dissertation, School of Electrical and Computer Engineering, Georgia Institute of Technology, 2016.

[48] M. H. Jenkins, J. M. Long, and T. K. Gaylord, "Multifilter phase imaging with partially coherent light," *Appl. Opt.*, vol. 53, no. 16, pp. D29–D39, Jun. 1, 2014.

[49] M. H. Jenkins and T. K. Gaylord, "Quantitative phase microscopy via optimized inversion of the phase optical transfer function," *Appl. Opt.*, vol. 54, no. 28, pp. 8566–8579, Oct. 1, 2015.

[50] M. H. Jenkins and T. K. Gaylord, "Three-dimensional quantitative phase imaging via tomographic deconvolution phase microscopy," *Appl. Opt.*, vol. 54, no. 31, pp. 9213–9227, Nov. 1, 2015.

[51] G. M. Noah, Y. Bao, and T. K. Gaylord, "Cross-sectional refractive-index variations in fiber Bragg gratings measured by quantitative phase imaging," *Opt. Lett.*, vol. 45, no. 1, pp. 53–56, Jan. 1, 2020.

[52] *Phi Optics Inc.* Champaign, IL, USA: https://phioptics.com/.

[53] *Tomocube, Inc.* Daejeon, Republic of Korea: http://www.tomocube.com/.

[54] *Lyncee tec*. Lausanne, Switzerland: www.lynceetec.com.

[55] *Nanolive*. Lausanne, Switzerland: www.nanolive.ch.

[56] *Phase Holographic Imaging*. Lund, Sweden: www.phiab.se.

[57] *Ovizio Imaging Systems*. www.ovizio.com.

[58] G. Popescu, *Quantitative Phase Imaging of cells and tissues*. New York: McGraw-Hill Biophotonics, 2011, ISBN: 978-0-07-166342-7.

[59] Y. Bao, "Theory, development, and application of quantitative phase imaging modalities on standard microscope platforms," Ph.D. dissertation, School of Electrical and Computer Engineering, Georgia Institute of Technology, 2019.

[60] N. Lue, W. Choi, G. Popescu, T. Ikeda, R. R. Dasari, K. Badizadegan, and M. S. Feld, "Quantitative phase imaging of live cells using fast Fourier phase microscopy," *Appl. Opt.*, vol. 46, no. 10, pp. 1836–1842, Apr. 1, 2007.

[61] I. Yamaguchi and T. Zhang, "Phase-shifting digital holography," *Opt. Lett.*, vol. 22, no. 16, pp. 1268–1270, Aug. 15, 1997.

[62] U. Schnars and W. Jüptner, "Direct recording of holograms by a CCD target and numerical reconstruction," *Appl. Opt.*, vol. 33, no. 2, pp. 179–181, Jan. 10, 1994.

[63] G. Popescu, T. Ikeda, R. R. Dasari, and M. S. Feld, "Diffraction phase microscopy for quantifying cell structure and dynamics," *Opt. Lett.*, vol. 31, no. 6, pp. 775–777, Mar. 15, 2006.

[64] M. Junwei, Y. Baoli, V. Trendafilova, S. Ketelhut, L. Kastl, B. Greve, and B. Kemper, "Quantitative phase imaging of cells in a flow cytometry arrangement utilizing michelson interferometer-based off-axis digital holographic microscopy," *J. Biophotonics*, vol. 12, no. 9, p. e201900085 (10 pp.) 2019.

[65] Z. Wang, L. Millet, M. Mir, H. Ding, S. Unarunotai, J. Rogers, M. U. Gillette, and G. Popescu, "Spatial light interference microscopy (SLIM)," *Opt. Express*, vol. 19, no. 2, pp. 1016–1026, Jan. 17, 2011.

[66] Y. Sung, W. Choi, C. Fang-Yen, K. Badizadegan, R. R. Dasari, and M. S. Feld, "Optical diffraction tomography for high resolution live cell imaging," *Opt. Express*, vol. 17, no. 1, pp. 266–277, Jan. 5, 2009.

[67] T. Ikeda, G. Popescu, R. R. Dasari, and M. S. Feld, "Hilbert phase microscopy for investigating fast dynamics in transparent systems," *Opt. Lett.*, vol. 30, no. 10, pp. 1165–1167, May 15, 2005.

[68] W. C. Warger II and C. A. DiMarzio, "Computational signal-to-noise ratio analysis for optical quadrature microscopy," *Opt. Express*, vol. 17, no. 4, pp. 2400–2422, Feb. 16, 2009.

[69] W. S. Rockward, A. L. Thomas, B. Zhao, and C. A. DiMarzio, "Quantitative phase measurements using optical quadrature microscopy," *Appl. Opt.*, vol. 47, no. 10, pp. 1684–1696, Apr. 1, 2008.

[70] I. Frenklach, P. Girshovitz, and N. T. Shaked, "Off-axis interferometric phase microscopy with tripled imaging area," *Opt. Lett.*, vol. 39, no. 6, pp. 1525–1528, Mar. 15, 2014.

[71] M. R. Arnison, K. G. Larkin, C. J. R. Sheppard, N. I. Smith, and C. J. Cogswell, "Linear phase imaging using differential interference contrast microscopy," *J. Microsc.*, vol. 214, no. 1, pp. 7–12, Apr. 1, 2004.

[72] F. Brandi and F. Wessel, "Widefield quantitative phase imaging by second-harmonic dispersion interferometry," *Opt. Lett.*, vol. 45, no. 15, pp. 4304–4307, Aug. 1, 2020.

[73] P. Bon, G. Maucort, B. Wattellier, and S. Monneret, "Quadriwave lateral shearing interferometry for quantitative phase microscopy of living cells," *Opt. Express*, vol. 17, no. 15, pp. 13 080–13 094, Jul. 20, 2009.

[74] *Phasics*. Soisy Sur Seine, France: www.phasicscorp.com.

[75] R. W. Gerchberg and W. O. Saxton, "Practical algorithm for determination of phase from image and diffraction plane pictures," *Optik*, vol. 35, no. 2, pp. 237–246, 1972.

[76] J. Marrison, L. Raty, P. Marriott, and P. O'Toole, "Ptychography - a label free, high-contrast imaging technique for live cells using quantitative phase information," *Sci. Rep.*, vol. 3, pp. 1–7, Aug. 6, 2013.

[77] X. Ou, R. Horstmeyer, C. Yang, and G. Zheng, "Quantitative phase imaging via Fourier ptychographic microscopy," *Opt. Lett.*, vol. 38, no. 22, pp. 4845–4848, Nov. 15, 2013.

[78] M. R. Teague, "Deterministic phase retrieval: A Green's function solution," *J. Opt. Soc. Am.*, vol. 73, no. 11, pp. 1434–1441, Nov. 11, 1983.

[79] J. P. Guigay, "Fourier-transform analysis of Fresnel diffraction patterns and in-line holograms," *Optik*, vol. 49, no. 1, pp. 121–125, 1977.

[80] J. P. Guigay, M. Langer, R. Boistel, and P. Cloetens, "Mixed transfer function and transport of intensity approach for phase retrieval in the Fresnel region," *Opt. Lett.*, vol. 32, no. 12, pp. 1617–1619, Jun. 15, 2007.

[81] Y. J. Bao and T. K. Gaylord, "Quantitative phase imaging method based on an analytical nonparaxial partially coherent phase optical transfer function," *J. Opt. Soc. Am. A*, vol. 33, no. 11, pp. 2125–2136, Nov. 1, 2016.

[82] Y. J. Bao, G. C. Dong, and T. K. Gaylord, "Weighted-least squares multi-filter phase imaging with partially coherent light: Characteristics of annular illumination," *Appl. Opt.*, vol. 58, no. 1, pp. 137–146, Jan. 2019.

[83] D. Deng, J. Peng, W. Qu, Y. Wu, X. Liu, W. He, and X. Peng, "Simple and flexible phase compensation for digital holographic microscopy with electrically tunable lens," *Appl. Opt.*, vol. 56, no. 21, pp. 6007–6014, Jul. 20, 2017.

[84] J. A. Rodrigo and T. Alieva, "Rapid quantitative phase imaging for partially coherent light microscopy," *Opt. Express*, vol. 22, no. 11, pp. 13 472–13 483, Jun. 2, 2014.

[85] J. A. Rodrigo, J. M. Soto, and T. Alieva, "Fast label-free microscopy technique for 3D dynamic quantitative imaging of living cells," *Biomed. Opt. Express*, vol. 8, no. 12, pp. 5507–5517, Dec. 1, 2017.

[86] R. Schubert, A. Vollmer, S. Ketelhut, and B. Kemper, "Enhanced quantitative phase imaging in self-interference digital holographic microscopy using an electrically focus tunable lens," *Biomed. Opt. Express*, vol. 5, no. 12, pp. 4213–4222, Dec. 1, 2014.

[87] C. Trujillo, A. Doblas, G. Saavedra, M. Martínez-Corral, and J. García-Sucerquia, "Phase-shifting by means of an electronically tunable lens: Quantitative phase imaging of biological specimens with digital holographic microscopy," *Opt. Lett.*, vol. 41, no. 7, pp. 1416–1419, Apr. 1, 2016.

[88] C. Zuo, Q. Chen, W. Qu, and A. Asundi, "High-speed transport-of-intensity phase microscopy with an electrically tunable lens," *Opt. Express*, vol. 21, no. 20, pp. 24 060–24 075, Oct. 7, 2013.

[89] M. Chen, L. Tian, and L. Waller, "3D differential phase contrast microscopy," *Biomed. Opt. Express*, vol. 7, no. 10, pp. 3940–3950, Oct. 1, 2016.

[90] L. Tian and L. Waller, "Quantitative differential phase contrast imaging in an LED array microscope," *Opt. Express*, vol. 23, no. 9, pp. 11 394–11 403, May 1, 2015.

[91] D. Lee, S. Ryu, U. Kim, D. Jung, and C. Joo, "Color-coded LED microscopy for multi-contrast and quantitative phase-gradient imaging," *Biomed. Opt. Express*, vol. 6, no. 12, pp. 4912–4922, Dec. 1, 2015.

[92] K. Arkadiusz, K. Wojciech, and K. Małgorzata, "Active limited-angle tomographic phase microscope," *J. Biomed. Opt*, vol. 20, no. 11, p. 111216 (10 pp.) Sep. 11, 2015.

[93] L. Camacho, V. Micó, Z. Zalevsky, and J. García, "Quantitative phase microscopy using defocusing by means of a spatial light modulator," *Opt. Express*, vol. 18, no. 7, pp. 6755–6766, Mar. 29, 2010.

[94] N. Yoneda, A. Onishi, Y. Saita, K. Komuro, and T. Nomura, "Single-shot higher-order transport-of-intensity quantitative phase imaging based on computer-generated holography," *Opt. Express*, vol. 29, no. 4, pp. 4783–4801, Feb. 15, 2021.

[95] A. B. Parthasarathy, K. K. Chu, T. N. Ford, and J. Mertz, "Quantitative phase imaging using a partitioned detection aperture," *Opt. Lett.*, vol. 37, no. 19, pp. 4062–4064, Oct. 1, 2012.

[96] R. Barankov, J.-C. Baritaux, and J. Mertz, "High-resolution 3D phase imaging using a partitioned detection aperture: A wave-optic analysis," *J. Opt. Soc. Am. A*, vol. 32, no. 11, pp. 2123–2135, Nov. 2015.

[97] D. S. Mehta and V. Srivastava, "Quantitative phase imaging of human red blood cells using phase-shifting white light interference microscopy with colour fringe analysis," *Appl. Phys. Lett.*, vol. 101, no. 20, p. 203701 (5 pp.) Nov. 12, 2012.

[98] H. Iwai, C. Fang-Yen, G. Popescu, A. Wax, K. Badizadegan, R. R. Dasari, and M. S. Feld, "Quantitative phase imaging using actively stabilized phase-shifting low-coherence interferometry," *Opt. Lett.*, vol. 29, no. 20, pp. 2399–2401, Oct. 15, 2004.

[99] E. W. Rogala and H. H. Barrett, "Prototype results of a phase-shifting interferometer capable of measuring the complex index and profile of a test surface," *Appl. Opt.*, vol. 41, no. 25, pp. 5298–5312, Sep. 1, 2002.

[100] G. B. Airy, "I. on the diffraction of an annular aperture," *London Edinburgh Philos. Mag. J. Sci.*, vol. 18, no. 114, pp. 1–10, Jan. 1841.

[101] V. P. Nayyar and N. K. Verma, "Resolution of a microscope - improvement using a centrally obstructed condenser aperture and a semitransparent pi-phase annular aperture objective system," *Appl. Opt.*, vol. 15, no. 5, pp. 1341–1344, May 1976.

[102] T. Noda, S. Kawata, and S. Minami, "Three-dimensional phase contrast imaging by an annular illumination microscope," *Appl. Opt.*, vol. 29, no. 26, pp. 3810–3815, Sep. 10, 1990.

[103] A. Vainrub, O. Pustovyy, and V. Vodyanoy, "Resolution of 90 nm (lambda/5) in an optical transmission microscope with an annular condenser," *Opt. Lett.*, vol. 31, no. 19, pp. 2855–2857, Oct. 1, 2006.

[104] C. J. R. Sheppard, "Partially coherent microscope imaging system in phase space: Effect of defocus and phase reconstruction," *J. Opt. Soc. Am. A*, vol. 35, no. 11, pp. 1846–1854, Nov. 1, 2018.

[105] M. Hisaka, "Phase-contrast scanning optical microscopy for biological tissues," *Proc. SPIE*, vol. 9272, 92720B (6pp.) Nov. 5, 2014.

[106] M. Gu, T. Tannous, and J. R. Sheppard, "Effect of an annular pupil on confocal imaging through highly scattering media," *Opt. Lett.*, vol. 21, no. 5, pp. 312–314, Mar. 1, 1996.

[107] B. Sick, B. Hecht, and L. Novotny, "Orientational imaging of single molecules by annular illumination," *Phys. Rev. Lett.*, vol. 85, no. 21, pp. 4482–4485, Nov. 20, 2000.

[108] S. Lindek, C. Cremer, and E. H. K. Stelzer, "Confocal theta fluorescence microscopy with annular apertures," *Appl. Opt.*, vol. 35, no. 1, pp. 126–130, Jan. 1, 1996.

[109] C. J. R. Sheppard and A. Choudhury, "Annular pupils, radial polarization, and superresolution," *Appl. Opt.*, vol. 43, no. 22, pp. 4322–4327, Aug. 1, 2004.

[110] S. Yang and Q. Zhan, "Third-harmonic generation microscopy with tightly focused radial polarization," *J. Opt. A: Pure Appl. Opt.*, vol. 10, no. 12, Oct. 31, 2008.

[111] W. Gong, K. Si, N. Chen, and C. J. R. Sheppard, "Focal modulation microscopy with annular apertures: A numerical study," *J. Biophotonics*, vol. 3, no. 7, pp. 476–484, Jul. 1, 2010.

[112] G. Antonacci, "Dark-field brillouin microscopy," *Opt. Lett.*, vol. 42, no. 7, pp. 1432–1435, Apr. 1, 2017.

[113] G. Terakado and H. Kano, "Localized surface plasmon microscope for simultaneous imaging of refractive index and fluorescence distributions: Fluorescence enhancement by annular pupil illumination," in *Biomedical Optics and 3-D Imaging*, ser. OSA Technical Digest (CD), Optical Society of America, BSuD62 (3pp.)

[114] G. Terakado, J. Ning, K. Watanabe, and H. Kano, "High-resolution simultaneous microscopy of refractive index and fluorescent intensity distributions by using localized surface plasmons," *Appl. Opt.*, vol. 52, no. 14, pp. 3324–3328, May 10, 2013.

[115] J. Borglin, D. N. Wang, N. J. Durr, D. Hanstorp, A. Ben-Yakar, and M. B. Ericson, "Annular beam shaping in multiphoton microscopy to reduce out-of-focus background," *Int. J. Spectrosc.*, May 24, 2017.

[116] A. Doi, R. Oketani, Y. Nawa, and K. Fujita, "High-resolution imaging in two-photon excitation microscopy using in situ estimations of the point spread function," *Biomed. Opt. Exp.*, vol. 9, no. 1, pp. 202–213, Jan. 1, 2018.

[117] B. Wang, J. Shi, T. Zhang, X. Xu, Y. Cao, and X. Li, "Improved lateral resolution with an annular vortex depletion beam in sted microscopy," *Opt. Lett.*, vol. 42, no. 23, pp. 4885–4888, Dec. 1, 2017.

[118] Y. Zhou and X. Li, "Super-resolution by annular pupil inserted scattered light fluorescence microscopes," *Opt. Rev.*, vol. 24, no. 3, pp. 398–405, Apr. 22, 2017.

[119] J. Hu and Y. Shen, "Annular oblique epi-illumination design for ultra-large-scale and high-resolution fluorescence microscopy," *Proc. SPIE*, vol. 10815, 108150M (7 pp.) Nov. 5, 2018.

[120] X. Ma, Z. Zhang, M. Yao, J. Peng, and J. Zhong, "Spatially-incoherent annular illumination microscopy for bright-field optical sectioning," *Ultramicroscopy*, vol. 195, pp. 74–84, Dec. 1, 2018.

[121] X. Ma, B. W. Zhou, Z. J. Su, Z. B. Zhang, J. Z. Peng, and J. G. Zhong, "Label-free 3D imaging of weakly absorbing samples using spatially-incoherent annular illumination microscopy," *Ultramicroscopy*, vol. 200, pp. 97–104, May 1, 2019.

[122] C. Zuo, J. Sun, J. Li, J. Zhang, A. Asundi, and Q. Chen, "High-resolution transport-of-intensity quantitative phase microscopy with annular illumination," *Sci. Rep.*, vol. 7, no. 1, p. 7654 (22 pp.) Aug. 9, 2017.

[123] S. Huang, F. Xi, C. Liu, and Z. Jiang, "Phase retrieval on annular and annular sector pupils by using the eigenfunction method to solve the transport of intensity equation," *J. Opt. Soc. Am. A*, vol. 29, no. 4, pp. 513–520, Apr. 1, 2012.

[124] J. Li, Q. Chen, J. Sun, J. Zhang, X. Pan, and C. Zuo, "Optimal illumination pattern for transport-of-intensity quantitative phase microscopy," *Opt. Express*, vol. 26, no. 21, pp. 27 599–27 614, Oct. 15, 2018.

[125] J. M. Wittkopp, T. C. Khoo, S. Carney, K. Pisila, S. J. Bahreini, K. Tubbesing, S. Mahajan, A. Sharikova, J. C. Petruccelli, and A. Khmaladze, "Comparative phase imaging of live cells by digital holographic microscopy and transport of intensity equation methods," *Opt. Express*, vol. 28, no. 5, pp. 6123–6133, Mar. 2, 2020.

[126] Y. Fan, J. Sun, Q. Chen, J. Zhang, and C. Zuo, "Wide-field anti-aliased quantitative differential phase contrast microscopy," *Optics Express*, vol. 26, no. 19, pp. 25 129–25 146, Sep. 17, 2018.

[127] Y. Fan, J. Sun, Q. Chen, X. Pan, L. Tian, and C. Zuo, "Optimal illumination scheme for isotropic quantitative differential phase contrast microscopy," *Photonics Res.*, vol. 7, no. 8, pp. 890–904, Aug. 1, 2019.

[128] Y. Fan, J. Sun, Q. Chen, X. Pan, M. Trusiak, and C. Zuo, "Single-shot isotropic quantitative phase microscopy based on color-multiplexed differential phase contrast," *APL Photonics*, vol. 4, no. 12, 121301 (7pp.) Dec. 1, 2019.

[129] Y. Fan, J. Sun, Q. Chen, X. Pan, and C. Zuo, "Video-rate isotropic quantitative differential phase contrast microscopy based on color-multiplexed annular illumination," *Proc. SPIE*, vol. 11186, 111860F (7 pp.) Nov. 19, 2019.

[130] A. Pan, C. Shen, B. Yao, and C. Yang, "Single-shot Fourier ptychographic microscopy via annular monochrome LED array," in *OSA Frontiers in Opt.*, Optical Society of America, FTh3F.4 (2 pp.)

[131] J. Sun, C. Zuo, and Q. Chen, "Optimal annular illumination pattern for Fourier ptychographic microscopy based on spectrum aliasing minimization," *Proc. SPIE*, vol. 11549, 115490C (7 pp.) Oct. 10, 2020.

[132] J. Sun, C. Zuo, and Q. Chen, "Spectrum aliasing minimization for Fourier ptychographic microscopy based on annular illumination optimization," *Proc. SPIE*, vol. 11761, 11761W (7 pp.) Jan. 15, 2021.

[133] J. Sun, C. Zuo, J. Zhang, Y. Fan, and Q. Chen, "High-speed Fourier ptychographic microscopy based on programmable annular illuminations," *Sci. Rep.*, vol. 8, no. 1, p. 7669, May 16, 2018.

[134] J. S. Sun, C. Zuo, and Q. Chen, "Video-rate quantitative phase microscopy based on Fourier ptychography with annular illuminations," *Proc. SPIE*, vol. 10827, 108270M (5pp.) Jul. 24, 2018.

[135] W. You, W. Lu, and X. Liu, "Single-shot wavelength-selective quantitative phase microscopy by partial aperture imaging and polarization-phase-division multiplexing," *Opt. Express*, vol. 28, no. 23, pp. 34 825–34 834, Nov. 9, 2020.

[136] J. Li, Q. Chen, J. Zhang, Y. Zhang, L. Lu, and C. Zuo, "Efficient quantitative phase microscopy using programmable annular LED illumination," *Biomed. Opt. Express*, vol. 8, no. 10, pp. 4687–4705, Oct. 1, 2017.

[137] L. Jiaji, A. Matlock, L. Yunzhe, C. Qian, Z. Chao, and T. Lei, "High-speed in vitro intensity diffraction tomography," *Proc. SPIE*, vol. 11186, 111860Y (9 pp.) Nov. 19, 2019.

[138] J. Li, A. Matlock, Y. Li, Q. Chen, L. Tian, and C. Zuo, "Resolution-enhanced intensity diffraction tomography in high numerical aperture label-free microscopy," *Photonics Res.*, vol. 8, no. 12, pp. 1818–1826, Dec. 1, 2020.

[139] J. Li, S. Jiasong, Z. Jialin, C. Qian, and Z. Chao, "Three-dimensional tomographic microscopy technique with multi-frequency combination with partially coherent illuminations," *Proc. SPIE*, vol. 10887, 108870O (9 pp.) Mar. 4, 2019.

[140] J. Li, N. Zhou, Z. Bai, S. Zhou, Q. Chen, and C. Zuo, "Optimization analysis of partially coherent illumination for refractive index tomographic microscopy," *Opt. Laser Eng.*, vol. 143, Mar. 15, 2021.

[141] J. Li, A. Matlock, Y. Li, Q. Chen, L. Tian, and C. Zuo, "Computational microscopy for quantitative phase imaging and refractive index tomography using annular illumination," *Proc. SPIE*, vol. 11249, 112491F (8pp.) Feb. 14, 2020.

[142] J. Huang, Y. Bao, and T. K. Gaylord, "Three-dimensional phase optical transfer function in axially symmetric microscopic quantitative phase imaging," *J. Opt. Soc. Am. A*, vol. 37, no. 12, pp. 1857–1872, Dec. 1, 2020.

[143] K. Kamon, T. Miyamoto, Y. Myoi, H. Nagata, M. Tanaka, and K. Horie, "Photolithography system using annular illumination," *Jpn. J. Appl. Phys.*, vol. 30, no. 11B, pp. 3021–3029, Nov. 1991.

[144] K. Tounai, H. Tanabe, H. Nozue, and K. Kasama, "Resolution improvement with annular illumination," *Proc. SPIE*, vol. 1674, pp. 753–764, Jun. 1, 1992.

[145] W. N. Partlo, P. J. Tompkins, P. G. Dewa, and P. F. Michaloski, "Depth of focus and resolution enhancement of i-line and deep-uv lithography using annular illumination," *Proc. SPIE*, vol. 1927, pp. 137–157, Aug. 8, 1993.

[146] C. Anderson, A. Allezy, W. L. Chao, C. Cork, W. Cork, R. Delano, J. DePonte, M. Dickinson, G. Gaines, J. Gamsby, E. Gullikson, G. Jones, S. Meyers, R. Miyakawa, P. Naulleau, S. Rekawa, F. Salmassi, B. Vollmer, D. Zehm, and W. H. Zhu, "Overview and status of the 0.5-NA micro-field exposure tool at Berkeley lab," *Proc. SPIE*, vol. 10957, Mar. 26, 2019.

[147] B. Vohnsen and D. Rativa, "Ultrasmall spot size scanning laser ophthalmoscopy," *Biomed. Opt. Exp.*, vol. 2, no. 6, pp. 1597–1609, Jun. 1, 2011.

[148] Y. N. Sulai and A. Dubra, "Adaptive optics scanning ophthalmoscopy with annular pupils," *Biomed. Opt. Exp.*, vol. 3, no. 7, pp. 1647–1661, Jul. 1, 2012.

[149] M. Damodaran, K. V. Vienola, B. Braaf, K. A. Vermeer, and J. F. de Boer, "Digital micromirror device based ophthalmoscope with concentric circle scanning," *Biomed. Opt. Exp.*, vol. 8, no. 5, pp. 2766–2780, May 1, 2017.

[150] M. Enyama, K. Hamada, M. Fukuda, and H. Kazumi, "Method of improving image sharpness for annular-illumination scanning electron microscopes," *Jpn. J. Appl. Phys.*, vol. 55, no. 6, Jun. 2016.

[151] T. Miyoshi, S. Takahashi, Y. Takaya, and S. Shimada, "High sensitivity optical detection of oriented microdefects on silicon wafer surfaces using annular illumination," *CIRP Ann. Manuf. Technol.*, vol. 50, no. 1, pp. 389–392, Dec. 2001.

[152] Y. Horikawa, "Resolution of annular-pupil optical systems," *J. Opt. Soc. Am. A*, vol. 11, no. 7, pp. 1985–1992, Jul. 1, 1994.

[153] E. Rascevska, K. J. Francis, and S. Manohar, "Annular illumination photoacoustic probe for needle guidance in medical interventions," *Proc. SPIE*, vol. 11077, 110770L (4 pp.) Jun. 2019.

[154] M. V. Schulmerich, K. A. Dooley, M. D. Morris, T. M. Vanasse, and S. A. Goldstein, "Transcutaneous fiber optic Raman spectroscopy of bone using annular illumination and a circular array of collection fibers," *J. Biomed. Opt.*, vol. 11, no. 6, Dec. 13, 2006.

[155] K.-Y. Hsu, Y.-C. Tung, M.-H. Chung, and C.-K. Lee, "Design and fabrication of sub-wavelength annular apertures for femtosecond laser machining," *Proc. SPIE*, vol. 9351, 93510U (6pp.) Mar. 12, 2015.

[156] Y. Bao and T. K. Gaylord, "Quantitative phase imaging method based on an analytical nonparaxial partially coherent phase optical transfer function: Erratum," *J. Opt. Soc. Am. A*, vol. 34, no. 8, pp. 1329–1329, Aug. 1, 2017.

[157] C. Zuo, Q. Chen, and A. Asundi, "Transport of intensity equation: A new approach to phase and light field," *Proc. SPIE*, vol. 9271, p. 92710H (17 pp.) Nov. 11, 2014.

[158] D. Paganin, A. Barty, P. J. McMahon, and K. A. Nugent, "Quantitative phase-amplitude microscopy. III. the effects of noise," *J. Micros.*, vol. 214, no. 1, pp. 51–61, Jul. 30, 2004.

[159] C. Zuo, Q. Chen, Y. Yu, and A. Asundi, "Transport-of-intensity phase imaging using Savitzky-Golay differentiation filter-theory and applications," *Opt. Express*, vol. 21, no. 5, pp. 5346–5362, Mar. 11, 2013.

[160] L. Waller, L. Tian, and G. Barbastathis, "Transport of intensity phase-amplitude imaging with higher order intensity derivatives," *Opt. Express*, vol. 18, no. 12, pp. 12 552–12 561, Jun. 7, 2010.

[161] M. Soto and E. Acosta, "Improved phase imaging from intensity measurements in multiple planes," *Appl. Opt.*, vol. 46, no. 33, pp. 7978–7981, Nov. 20, 2007.

[162] N. Streibl, "Three-dimensional imaging by a microscope," *J. Opt. Soc. Am. A*, vol. 2, no. 2, pp. 121–127, Feb. 1, 1985.

[163] Y. Bao and T. K. Gaylord, "Iterative tomographic deconvolution phase microscopy," in *OSA Frontiers in Opt.*, ser. OSA Technical Digest (online), Optical Society of America, p. FM3C.3.

[164] M.-G. Fernando, R. D. Kenneth, and C. B. Alan, "Missing cone of frequencies and low-pass distortion in three-dimensional microscopic images," *Opt. Engr.*, vol. 27, no. 6, pp. 461–465, Jun. 1, 1988.

[165] J. Lim, K. Lee, K. H. Jin, S. Shin, S. Lee, Y. Park, and J. C. Ye, "Comparative study of iterative reconstruction algorithms for missing cone problems in optical diffraction tomography," *Opt. Exp.*, vol. 23, no. 13, pp. 16 933–16 948, Jun. 29, 2015.

[166] L. Waller, S. S. Kou, C. J. R. Sheppard, and G. Barbastathis, "Phase from chromatic aberrations," *Opt. Express*, vol. 18, no. 22, pp. 22 817–22 825, Oct. 25, 2010.